ANALYSIS OF MAGNETIC RESONANCE IMAGING IN
INHOMOGENOUS MAIN MAGNETIC FIELD

A THESIS SUBMITTED TO
THE GRADUATE SCHOOL OF NATURAL AND APPLIED SCIENCES
OF
MIDDLE EAST TECHNICAL UNIVERSITY

BY

VOLKAN EMRE ARPINAR

IN PARTIAL FULFILLMENT OF THE REQUIREMENTS
FOR
THE DEGREE OF DOCTOR OF PHILOSOPHY
IN
ELECTRICAL AND ELECTRONICS ENGINEERING

AUGUST 2009

Approval of the thesis:

ANALYSIS OF MAGNETIC RESONANCE IMAGING IN INHOMOGENOUS MAIN MAGNETIC FIELD

submitted by **VOLKAN EMRE ARPINAR** in partial fulfillment of the requirements for the degree of **Doctor of Philosophy in Electrical and Electronics Engineering Department, Middle East Technical University** by**,**

Prof. Dr. Canan Özgen   _____
Dean, Graduate School of **Natural and Applied Sciences**

Prof. Dr. İsmet Erkmen   _____
Head of Department, **Electrical and Electronics Eng.**

Prof. Dr. Murat Eyüboğlu   _____
Supervisor, **Electrical and Electronics Eng. Dept., METU**

Examining Committee Members

Prof. Dr. Nevzat Güneri Gençer   _____
Electrical and Electronics Engineering Dept., METU

Prof. Dr. Murat Eyüboğlu   _____
Electrical and Electronics Engineering Dept., METU

Prof. Dr. Kemal Leblebicioğlu   _____
Electrical and Electronics Engineering Dept., METU

Assist. Prof. Dr. Yeşim Serinağaoğlu Doğrusöz   _____
Electrical and Electronics Engineering Dept., METU

Prof. Dr. Adnan Köksal   _____
Electrical and Electronics Eng. Dept., Hacettepe Univ.

Date: _____28/08/2009_____

I hereby declare that all information in this document has been obtained and presented in accordance with academic rules and ethical conduct. I also declare that, as required by these rules and conduct, I have fully cited and referenced all material and results that are not original to this work.

Name, Last name: Volkan Emre Arpınar

Signature:

ABSTRACT

ANALYSIS OF MAGNETIC RESONANCE IMAGING IN INHOMOGENOUS MAIN MAGNETIC FIELD

Arpınar, Volkan Emre

Ph.D., Department of Electrical and Electronics Engineering

Supervisor: Prof. Dr. Murat Eyüboğlu

August 2009, 119 pages

In this study, analysis of Magnetic Resonance Imaging (MRI) in inhomogeneous main magnetic field is conducted. A numerical model based on Bloch equation is implemented for MRI, to understand effect of inhomogeneous magnetic field to Magnetic Resonance (MR) signal. Using the model, relations between inhomogeneity levels in main magnetic field with energy, decay time, bandwidth of the FID signal is investigated. Also relation between the magnetic field inhomogeneity and field of view is determined. To simulate measurement noise in the FID signal under inhomogeneous main magnetic field, noise model for MRI with homogeneous main field is altered. Following the numerical model development an image reconstruction algorithm for inhomogeneous main magnetic field is developed to remove undesirable effect of field inhomogeneity in image reconstruction. To evaluate capability of the reconstruction algorithm, the algorithm is tested for several input parameters which results in different

noise levels in the FID signal. Then reconstruction errors are analysed to gain information about feasibility of MRI in inhomogeneous main magnetic field.

ÖZ

HOMOJEN OLMAYAN ANA MANYETİK ALAN KULLANAN MANYETİK REZONANS GÖRÜNTÜLEMENİN ANALİZİ

Arpınar, Volkan Emre

Doktora, Elektrik ve Elektronik Mühendisliği Bölümü

Tez Yöneticisi: Prof. Dr. Murat Eyüboğlu

Ağustos 2009, 119 sayfa

Bu çalışmada homojen olmayan ana manyetik alan kullanan manyetik rezonans görüntülemenin (MRG) analizi yapılmıştır. Homojen olmayan ana manyetik alanın, manyetik rezonans (MR) sinyaline etkisini anlamak için Bloch denklemi tabanlı sayısal bir model oluşturulmuştur. Oluşturulan sayısal model kullanılarak, manyetik alandaki homojenlikten sapma miktarıyla, MR sinyalinin enerjisinin, sönüm süresinin ve bant genişliğinin nasıl değiştiği incelenmiştir. Ayrıca manyetik alandaki homojenlikten sapma miktarıyla görüntüleme alanının nasıl değiştiği incelenmiştir. Homojen olmayan manyetik alandaki gürültü sinyalinin benzetimini yapmak için, homojen durum için geçerli gürültü modeli geliştirilerek yeni bir gürültü modeli oluşturulmuştur. Sayısal modelin geliştirilmesinden sonra homojen olmayan ana manyetik alan için görüntüleme algoritması geliştirilmiştir. Bu görüntüleme algoritması manyetik alandaki homojenlikten sapmadan dolayı oluşan bozulmaları düzeltmek içindir. Görüntüleme algoritmasının performansını test etmek için farklı görüntüleme

parametreleri kullanılarak farklı seviyelerde gürültüye sahip MR sinyalleri oluşturulmuştur. Oluşturulacak sinyaller ve geliştirilen görüntü oluşturma algoritmasıyla görüntüler elde edilmiş ve elde edilen görüntülerdeki gürültü incelenerek homojen olmayan manyetik alan kullanan MRG sistemlerinin fizibilitesi hakkında bilgi elde edilmiştir.

Anahtar kelimeler: Manyetik rezonans görüntüleme, Homojen olmayan ana manyetik alan, Görüntü geriçatımı.

To my family

ACKNOWLEDGEMENTS

TABLE OF CONTENTS

LIST OF TABLES

LIST OF FIGURES

CHAPTER 1

INTRODUCTION

Magnetic Resonance Imaging (MRI) is a well-known tomographic imaging technique that produces images of internal physical and chemical characteristics of an object from externally measured Free Induction Decay (FID) signals. Physically, MRI is based on well-known Nuclear Magnetic Resonance (NMR) phenomenon observed by Felix Bloch and Edward Purcell independently in 1946 [1, 2].

1.1. Magnetic Resonance Imaging in Homogenous Main Magnetic Fields

In 1972, Paul Lauterbour developed an image formation method by the spatial information encoded to the MR signal [3]. A conventional imaging system is composed of a main magnet, a gradient system, and a radio frequency (RF) system.

The main magnet's function is to generate a strong main magnetic field ($\vec{B}_0$). In clinical MRI systems, magnitude of $\vec{B}_0$ is the range of 0.3 T to 3 T [4]. For some experimental systems, this value goes up to 20 T. The strength of $\vec{B}_0$ directly affects Signal to Noise Ratio (SNR) and spatial resolution of an imaging system. In these systems, homogeneity over the imaged volume is also important. So, efforts are made to achieve homogeneity of the main magnetic field. Therefore, in these systems inhomogeneity is as small as 10 ppm to 50 ppm [4]. After generation of the homogeneous main magnetic field, the gradient coil system is

used to perturb the main magnetic field in a controlled manner to encode spatial information to the FID signal. Therefore, tomographic image of an object is obtained from the spatially encoded FID signal by means of an image reconstruction algorithm.

The magnetic field gradient system normally consists of three orthogonal gradient coils. These coils are designed to generate time varying magnetic fields in a controlled way. This generates spatial non-uniformity in magnetic field so that spatial information is encoded to the FID signal. This makes signal localization and imaging possible. Strengths of the gradient fields are small compared to main magnetic field. Coils with amplifiers generate these gradient fields and the gradient strength is in the order of milli-Tesla per meter (mT/m) in MRI systems with homogeneous main magnetic field [5]. In order to receive signal from an object, to be imaged, a Radio Frequency (RF) signal, which is synchronized with the gradient fields, has to be applied to the object.

The RF system consists of transmitter coils, that are capable of generating time varying magnetic fields for excitation, and receiver coils, that are used to collect FID signal. In some systems, a single coil is used for both purposes. These transmitter and receiver coils are named as RF coils since the operation frequency in the range of RF signals. The desired futures of the RF coils are high detection sensitivity and generation of uniform magnetic fields. This achieves uniform excitation and signal reception from the object to be imaged.

1.2. Magnetic Resonance Phenomena in Inhomogeneous Magnetic Fields

Several magnetic resonance studies have been performed in inhomogeneous main magnetic fields. The primary usage of inhomogeneous main magnetic fields has been in NMR experiments. Following that, some imaging attempts were made.

1.2.1. Nuclear Magnetic Resonance Systems Using Inhomogeneous Magnetic Fields

The first NMR system with inhomogeneous main field is used in oil industry [6-8]. This system has a probe lowered to the hole of an oil-well. The probe uses a small permanent magnet to generate a main magnetic field. Therefore, the main magnetic field strength and homogeneity is deteriorating. This inhomogeneous magnetic fields strength is about 0.03 T with a field variation of 0.1 T/m. To receive signal from the samples, echo techniques are used to overcome the effects of field inhomogeneity [9-12]. These systems designed to record signal originating from a small region to have limited inhomogeneity in the field corresponding to the Region of Interest (ROI).

Inside-out NMR systems are similar to the previous oil-well systems [13-16]. In these systems, a NMR sensor, which is smaller than the object, is placed near the object. However, the single-sided sensors used in these systems have magnetic field as homogeneous as possible. These systems are used to the detection of moisture in soil [18,19], concrete [18, 20], building materials [20, 21] and food [22-24], explosives detection [25,26], quality and product control [27-30], medical diagnostics [15], and on-line monitoring [15, 16, 22].

3

In 1996, a mobile NMR surface scanner (NMR-MOUSE) has been developed for investigation of arbitrarily large objects, to be used mainly in material science [31, 32]. As the NMR MOUSE is developed, more information about NMR phenomenon in inhomogeneous magnetic fields is obtained. Initially, this system was mainly used to measure transverse relaxation time of the sample [31]. After that, other parameters like longitudinal relaxation time [33-34], diffusion coefficients [35 - 38], double-quantum coherences and their relaxation times [39, 40] and velocities [41] have been measured using this system.

The basic experimental setup of the surface scanner constructed by Eidmann *et al.* is composed of mainly two parts [31]. The first part is the RF pulse generation amplification and signal detection part with a NMR spectrometer. NMR spectrometer is connected to a PC. The setup size fits on a desktop. The PC is also utilized to generate pulse sequence, and acquire data. The second part is the probe. The probe weights about 2.5 kg and the user could position it arbitrarily. The probe is composed of a solenoid RF coil and a permanent magnet. This setup eliminates the usage of super conducting magnet, which is the most expensive part of the conventional MR systems. However, main magnetic and RF fields are inhomogeneous, Hahn echoes, CPMG type pulse sequences are used [42]. In this system, the strength of the pulse is not clear due to depth dependence of the excitation flip angle [31]. So the strength of the pulse is determined experimentally to make the signal response maximum. Sensitive depth range of the system is about 0 - 2 mm and the sensitive area is 3.5 mm x 3.5 mm for that depth [31].

1.2.2. Magnetic Resonance Imaging Attempts Using Inhomogeneous Magnetic Fields

These portable NMR systems are also used for imaging purposes. These systems have low and inhomogeneous main magnetic fields. The disadvantage of low and inhomogeneous main magnetic field is low sensitivity and low signal to noise ratio (SNR) [43]. However, the advantages are the longitudinal relaxation time decreases for many materials so the repetition time between scans is shortened, the relaxation time contrast improves, chemical shift and susceptibility artifacts are scaled down, and the instrumentation becomes smaller and less expensive [44].

In 1998, Bülmich *et al.* made *in-vitro* explorative studies on biomedical samples using the NMR-MOUSE. They obtained a cross-sectional image of transverse relaxation time of a pork tendon [32]. In order to obtain image of the pork leg the NMR mouse is positioned over the region of interest. One year later, anisotropy of a tendon investigated *in- vivo* by Haken and Bülmich [45].

In 2000, Prado *et al.* integrated a gradient coil to the previously designed NMR-MOUSE to encode spatial information to the recorded signal. By using this gradient, one-dimensional imaging is possible without moving the probe. The maximum field of view (FOV) of the system is about 15 mm [46]. Also, Baril *et al.* uses specially designed RF coil which has a RF field inhomogeneity in a controlled manner to obtain one-dimensional images of spin density. In this method, the gradient fields are not used [47, 48].

By using the NMR-MOUSE, two and three-dimensional images of materials have been investigated in recent years. This is achieved by using mechanical

movement and by using gradient fields [49-52]. In these images, gradient coils are used to encode the position in the FOV.

Another method by using inhomogeneous main magnetic field is Stray-field Imaging (STRAFI), first suggested by Samoilenko *et al.* [53]. This method has a restricted sensitive region and it exploits extremely large magnetic field gradient found outside the central region of a high field superconducting NMR magnet. This method preserves dynamic contrast, which makes magnetic resonance so powerful in the first place, while at the same time offers very high spatial resolution [54, 55]. Due to extremely large magnetic field gradient, even a short radio frequency pulse only excites nuclei in a narrow slice of the sample, orthogonal to the gradient direction. This provides spatial localization of the NMR measurement. By moving the sample gradually through the gradient and repeating the measurement, it is possible to build a profile of the sample in the gradient direction. By this mechanical motion, two or three-dimensional images can be obtained. Miller and Garroway also employ STRAFI technique with use of surface coils that generate RF field perpendicular to an inhomogeneous main magnetic field [56].

1.3. Numerical Models of Magnetic Resonance Phenomena

MRI numerical models are generally made for homogenous main magnetic fields and RF fields which are perpendicular to main magnetic field [57, 58]. In some models inhomogeneity cannot be fully maintained [59, 60]. Only a small deviation in the magnitude but not in the direction is covered in the model. In 1984, Bittoun and colleagues solved the Bloch equation for one-dimension by solving for every separate point [61]. Bloch equation models the behavior of magnetization vector, which is an ensemble of magnetizations of NMR active

atoms. After that, Summers *et al.* and Olsson *et al.* used the same technique to solve the problem in two-dimensions and then in three-dimensions [62, 63]. Since the computational cost is too high to solve the Bloch equation for every point, they parallelized the calculations [64, 65].

Some NMR models use Quantum density matrixes [66-68]. They are good at simulating NMR phenomena. This approach models every NMR active atom. However, computational cost is very high compared to Bloch equation since, it models every atom in the object rather than ensemble of magnetization. Also in heterogeneous biological materials, it is not practical to use this model [69].

1.4. Aim of the Thesis Study

Aim of this thesis is analysis of MR imaging in inhomogeneous main magnetic field. For that, a numerical model based on Bloch equation is implemented. This model gives deep understanding about the effects of inhomogeneous magnetic field to the FID signal. Using the model, relations between inhomogeneity levels in main magnetic field with energy, decay time, bandwidth of FID signal are investigated. Also relation between the magnetic field inhomogeneity and field of view is determined. To simulate the noise signal for the inhomogeneous main magnetic field case, noise model for MRI with homogeneous field is altered. Following the numerical model development, an image reconstruction algorithm in inhomogeneous main magnetic field is developed to remove undesirable effect of field inhomogeneity in image reconstruction. To evaluate capability of the reconstruction algorithm, the algorithm is tested for different input parameters which results in different noise levels in the FID signal. Then reconstruction errors are analysed to gain information about feasibility of MRI in inhomogeneous main magnetic field.

Using these analyses of MRI system in inhomogeneous main magnetic field, portable MRI systems with inhomogeneous magnetic fields are possible. To generate inhomogeneous magnetic field a permanent magnet can be used and the price of the system is lowered. Also, the reconstruction algorithm can be applied to any MRI system to correct the errors due to inhomogeneity in the main magnetic field.

CHAPTER 2

THEORY OF SIGNAL AND NOISE MODELING IN INHOMOGENEOUS MAGNETIC FIELDS AND THE PROPOSED FFT BASED RECONSTRUCTION ALGORITHM

In this chapter, theory of the signal model developed for MRI in inhomogeneous magnetic fields is given. Then the noise model developed for this case is given. Finally, the proposed reconstruction algorithm is explained.

2.1. Developed Numerical Model for Magnetic Resonance Phenomena in Inhomogeneous Magnetic Fields

In order to understand and analyze the FID signal, a numerical model is needed for magnetic resonance phenomena in inhomogeneous magnetic fields.

2.1.1. Magnetic Resonance Phenomena in Inhomogeneous Magnetic Fields - Basics and Assumptions

Biological samples are composed of atoms. A fundamental property with odd atomic number or atomic weight possesses an angular momentum called as a nuclear spin. Nuclear spin can be characterized by quantum mechanics however, in MRI of biological tissues an ensemble of the spins is analyzed. Since the imaging of hydrogen atoms in biological tissues is aimed, our interest is the ensemble of the spins. So that using quantum mechanics principles, when the biological object is placed in an external magnetic field, behavior of a spin system, which generates nuclear magnetism, can be found.

Nuclear magnetism of a spin system originates from the microscopic magnetic field associated with a nuclear spin. As an example: the hydrogen atom, which has a nucleus with electrical charge and rotates around its own axis, creates a magnetic field around it. This spin's magnetic field can be represented as a vector quantity. This quantity can be related with spin angular momentum ($\vec{J}$) using (2.1). γ is a physical constant known as gyromagnetic constant and it is nucleus specific. For a hydrogen atom it is equal to $2.675 \cdot 10^8$ Hz/T.

$$\vec{\mu} = \gamma \vec{J} \qquad (2.1)$$

Based on the theory of quantum mechanics, the magnitude of nuclear magnetic moment can take discrete values [3]. The hydrogen atoms can take two possible values. Although, the magnitude of nuclear magnetic momentum is certain under any conditions, but its direction is completely random in the absence of a strong external magnetic field. This is due to thermal random motion.

To achieve macroscopic magnetism from an object, it is necessary to align the direction of the spins. This can be done by applying a strong external magnetic field. Assume that the magnetic field spatial distribution of main magnetic field can be denoted as $\vec{B}_0(x, y, z)$. It can be decomposed as magnitude distribution ($\left|\vec{B}_0(x, y, z)\right|$) and unit vector distribution ($\vec{r}\,'(x, y, z)$) in the same direction with $\vec{B}_0(x, y, z)$. Hence, $\vec{B}_0(x, y, z)$ can represented as

$$\vec{B}_0(x, y, z) = B_0(x, y, z)\vec{r}\,'(x, y, z) \tag{2.2}$$

As indicated before, the magnetic momentum can take discrete set of orientations. When the external magnetic field applied in the direction of $\vec{r}\,'(x, y, z)$, the component of the magnetic momentum with direction $\vec{r}\,'(x, y, z)$ becomes certain but the other components are not known. For hydrogen atom there exists two possible orientations in $\vec{r}\,'(x, y, z)$ direction. This means that the orientation of magnetic momentum vector quantized along the direction of externally applied main magnetic field. Since there is no external magnetic field in transverse plane (normal plane to $\vec{r}\,'(x, y, z)$), transverse component of magnetic momentum remains arbitrary. In order to find a differential relation between magnetic momentum and external magnetic field, motion of magnetic momentum has to be described.

According to classical mechanic, the torque of magnetic momentum when placed in an external magnetic field is given in equation (2.3)

$$\frac{\partial \vec{J}(x, y, z, t)}{\partial t} = \vec{\mu}(x, y, z, t) \times \left(\left| B_0(x, y, z) \right| \vec{r}\,'(x, y, z) \right) \tag{2.3}$$

Using the equation (2.1) with (2.3), then

$$\frac{\partial \vec{\mu}(x, y, z, t)}{\partial t} = \gamma \vec{\mu}(x, y, z, t) \times \left(\left| B_0(x, y, z) \right| \vec{r}\,'(x, y, z) \right) \tag{2.4}$$

In order to solve the differential equation in (2.4), coordinate system has to be changed. A new local coordinate system is required to obtain decoupled differential equations. The local coordinate system can be defined by the orthogonal base vectors namely $\vec{\theta}\,', \vec{\varphi}\,'$, and $\vec{r}\,'$ for every position (x, y, z). To have a decoupled differential equation $\vec{r}\,'$ is selected in the same direction as $\vec{B}_0(x, y, z)$. Afterwards $\vec{\theta}\,'$ can be selected arbitrarily which lies in the normal plane to $\vec{r}\,'$. That is

$$\vec{r}\,'(x, y, z) \cdot \vec{\theta}\,'(x, y, z) = 0 . \tag{2.5}$$

Then base vector $\vec{\varphi}\,'$ is selected. In order to have a conventional right handed coordinate system select $\vec{\varphi}\,'$ as in (2.6)

$$\vec{\varphi}\,'(x, y, z) = \vec{r}\,'(x, y, z) \times \vec{\theta}\,'(x, y, z) \tag{2.6}$$

The equation in scalar form becomes

$$\begin{cases} \dfrac{\partial \mu_{\vec{\theta}'}(x, y, z, t)}{\partial t} = \gamma \left| \vec{B}_0(x, y, z) \right| \mu_{\vec{\varphi}'}(x, y, z, t) = \omega_0(x, y, z) \mu_{\vec{\varphi}'}(x, y, z, t) \\[4mm] \dfrac{\partial \mu_{\vec{\varphi}'}(x, y, z, t)}{\partial t} = \gamma \left| \vec{B}_0(x, y, z) \right| \mu_{\vec{\theta}'}(x, y, z, t) = \omega_0(x, y, z) \mu_{\vec{\theta}'}(x, y, z, t) \\[4mm] \dfrac{\partial \mu_{\vec{r}'}(x, y, z, t)}{\partial t} = 0 \end{cases} \tag{2.7}$$

In (2.7) $\mu_{\bar{\theta}'}$, $\mu_{\bar{\varphi}'}$, $\mu_{\bar{r}'}$, corresponds to projection of $\vec{\mu}$ to $\vec{r}'$, $\vec{\theta}'$, $\vec{\varphi}'$ axis. ω_0 is named as the Larmor frequency and it is equal to $\gamma |\vec{B}_0(x, y, z)|$. After taking the derivatives of the first two equations with respect to time and using the above relations, the result is

$$\frac{\partial^2 \mu_{\bar{\theta}'}(x, y, z, t)}{\partial t^2} = \gamma |\vec{B}_0(x, y, z)| \frac{\partial \mu_{\bar{\varphi}'}(x, y, z, t)}{\partial t} = \omega_0^2(x, y, z) \mu_{\bar{\theta}'}(x, y, z, t)$$

$$\frac{\partial^2 \mu_{\bar{\varphi}'}(x, y, z, t)}{\partial t^2} = \gamma |\vec{B}_0(x, y, z)| \frac{\partial \mu_{\bar{\theta}'}(x, y, z, t)}{\partial t} = \omega_0^2(x, y, z) \mu_{\bar{\varphi}'}(x, y, z, t)$$

(2.8)

Setting the initial conditions to $\mu_{\bar{r}'}(x, y, z, 0)$, $\mu_{\bar{\varphi}'}(x, y, z, 0)$, and $\mu_{\bar{\theta}'}(x, y, z, 0)$ then the solution becomes:

$$\begin{cases} \dfrac{\partial \mu_{\bar{\theta}'}(x, y, z, t)}{\partial t} = \mu_{\bar{\theta}'}(x, y, z, 0)\cos(\omega_0(x, y, z)t) + \mu_{y'}(x, y, z, 0)\sin(\omega_0(x, y, z)t) \\ \dfrac{\partial \mu_{\bar{\varphi}'}(x, y, z, t)}{\partial t} = -\mu_{\bar{\theta}'}(x, y, z, 0)\sin(\omega_0(x, y, z)t) + \mu_{\bar{\varphi}'}(x, y, z, 0)\cos(\omega_0(x, y, z)t) \\ \mu_{\bar{r}'}(x, y, z, t) = \mu_{\bar{r}'}(x, y, z, 0) \end{cases}$$

(2.9)

In order to represent our magnetic moment in a different way the transverse part of the magnetic moment, which is defined by $\mu_{\bar{\theta}'}(x, y, z, t)$ and $\mu_{\bar{\varphi}'}(x, y, z, t)$, can be combined as a complex function. That is

$$\mu_{\bar{\theta}'\bar{\varphi}'}(x, y, z, t) = \mu_{\bar{\theta}'}(x, y, z, t) + j\mu_{\bar{\varphi}'}(x, y, z, t)$$

(2.10)

Then (2.9) becomes

$$\begin{cases} \mu_{\vec{\theta}'\vec{\varphi}'}(x,y,z,t) = \mu_{\vec{\theta}'\vec{\varphi}'}(x,y,z,0)e^{-j\gamma|B_0(x,y,z)|t} \\ \mu_{\vec{r}'}(x,y,z,t) = \mu_{\vec{r}'}(x,y,z,0) \end{cases} \qquad (2.11)$$

To describe the collective behavior of a spin system, a macroscopic magnetization vector $\vec{M}$ can be introduced for inhomogeneous main magnetic field. Due to change in the main magnetic field with position, we have to divide the object into volume elements (voxels) and assume that main magnetic field change is negligible in that voxel. Say that $\vec{M}(\vec{\theta}_i, \vec{\varphi}_i, \vec{r}_i, t)$ is the vector sum of all the magnetic moment in the voxel defined by $\vec{\theta}_i$, $\vec{\varphi}_i$, and $\vec{r}_i$. Then,

$$\vec{M}(x_i, y_i, z_i, t) = \sum_{n=1}^{N(x_i, y_i, z_i)} \vec{\mu}_{n,t} \qquad (2.12)$$

where N_{x_i, y_i, z_i} is the total number of spins in the voxel. By using previous analysis, we can find collective behavior of the spins when placed in static magnetic field. As discussed before $\vec{\mu}_{n,t}$ takes two possible orientations with respect to the $\vec{r}'(x,y,z)$ axis at a given time for hydrogen atom. Spins in different orientations have different energy interaction with the static magnetic field. According to the quantum theory for every voxel,

14

$$E = -\vec{\mu} \cdot \vec{B}_0 = -\mu_{\vec{r}'} \cdot \left| \vec{B}_0 \right| \tag{2.13}$$

Then for pointing up spins,

$$E_\uparrow = -\frac{1}{2} \gamma \hbar \left| \vec{B}_0 \right| \tag{2.14}$$

where $\hbar$ is Planck's constant divided by 2π, and pointing down spins

$$E_\downarrow = \frac{1}{2} \gamma \hbar \left| \vec{B}_0 \right| \tag{2.15}$$

As seen above, spin up state is the lower-energy state, while the spin-down state is the higher-energy state since $\left| \vec{B}_0 \right|$ is magnitude. The energy difference between the two energy states is $\gamma \hbar \left| \vec{B}_0 \right|$. This nonzero difference in energy level between the two spin states is known as the Zeeman Splitting Phenomenon. The spin population difference in the two spin states is related to their energy difference. According to the Boltzmann relationship

$$\frac{N_\uparrow}{N_\downarrow} = \exp\left(\frac{\Delta E}{K T_s} \right) \tag{2.16}$$

Where $N_\uparrow$ is number of pointing up spins, $N_\downarrow$ is number of pointing down spins, T_s is absolute temperature of the spin system and K is Boltzmann constant.

Assuming magnitude of main magnetic field in the order of Tesla range then $\Delta E << KT_s$. Therefore, the exponential term can be written as first order approximation. This result can be substituted to (2.16). Then the difference between $N_\uparrow$ and $N_\downarrow$ is

$$N_\uparrow - N_\downarrow = N_s \frac{\gamma \hbar \left| \vec{B}_0 \right|}{2KT_s} \qquad (2.17)$$

This equation indicates that there is a fraction of spins in the lower-energy state. This occurs because a spin is more likely to take the lover energy state. This population difference generates the $\vec{M}$ vector, which is equal to

$$\vec{M}(x_i, y_i, z_i, t) = M_{\vec{r}'}(x_i, y_i, z_i, t)\vec{r}\,'(x_i, y_i, z_i) + M_{\vec{\theta}'}(x_i, y_i, z_i, t)\vec{\theta}\,'(x_i, y_i, z_i)$$
$$+ M_{\vec{\varphi}'}(x_i, y_i, z_i, t)\vec{\varphi}\,'(x_i, y_i, z_i) \qquad (2.18)$$

and it can be rewritten as

$$\vec{M}(x_i, y_i, z_i, t) = \left(\sum_{n=1}^{N(x_i, y_i, z_i)} \mu_{\vec{\theta}', n, t} \right) \vec{\theta}'(x_i, y_i, z_i) + \left(\sum_{n=1}^{N(x_i, y_i, z_i)} \mu_{\vec{\varphi}', n, t} \right) \vec{\varphi}'(x_i, y_i, z_i)$$

$$\left(\sum_{n=1}^{N(x_i, y_i, z_i)} \mu_{\vec{r}', n, t} \right) \vec{r}'(x_i, y_i, z_i) \tag{2.19}$$

The first two terms are zero because in transverse plane component phase is random so the vector sum is zero for sufficient number of spin in that voxel. $\mu_{z', n, t}$ can take two possible values as discussed above. These values can be

$$\mu_{z', n, t} = \begin{cases} +\dfrac{1}{2} \gamma\hbar \\[2mm] -\dfrac{1}{2} \gamma\hbar \end{cases} \tag{2.20}$$

Substituting (2.20) to (2.19)

$$\vec{M}(x_i, y_i, z_i, t) = \left(\sum_{n=1}^{N_\uparrow (x_i, y_i, z_i)} \frac{1}{2} \gamma\hbar \right) \vec{r}'(x_i, y_i, z_i) + \left(\sum_{n=1}^{N_\downarrow (x_i, y_i, z_i)} \frac{1}{2} \gamma\hbar \right) \vec{r}'(x_i, y_i, z_i) \tag{2.21}$$

Since $\gamma\hbar$ is constant

$$\vec{M}(x_i, y_i, z_i, t) = \frac{1}{2} \left(N_\uparrow (x_i, y_i, z_i) - N_\downarrow (x_i, y_i, z_i) \right) \gamma\hbar\, \vec{r}'(x_i, y_i, z_i) \tag{2.22}$$

Therefore, the bulk magnetization vector points exactly along the positive direction of the $\vec{r}\,'(x_i, y_i, z_i)$ axis at equilibrium. Difference between the number of spins that pointing up and down is found in (2.17) then the magnitude of magnetization vector is equal to:

$$\left|\vec{M}(x_i, y_i, z_i, t)\right| = \frac{\gamma^2 \hbar^2 B_0(x_i, y_i, z_i)}{4KT_s} N_s\left(x_i, y_i, z_i\right) \tag{2.23}$$

This is true for ½ spin system which corresponds to hydrogen atom. So far the magnetic momentum is investigated when there is only position dependent main magnetic field. In order to excite the object to be examined, external time varying magnetic field has to be applied. This corresponds to the RF pulse.

2.1.2 RF Pulse Modeling and Excitation Used in Inhomogeneous Magnetic Fields

RF pulse generates magnetic field and it can be named as $\vec{B}_1$ field. This is called "RF pulse" since its frequency is in radio frequency range and it is applied for a short time. It is normally ON for a few microseconds to milliseconds. The strength of $\vec{B}_1$ field has to be small compared to main magnetic field strength. It has a form of

$$\begin{aligned}
B_1(x_i, y_i, z_i, t) = 2B_1^e(t)\cos(\omega_{rf}t + \varphi)\big[& B_{1,x}(x_i, y_i, z_i)\vec{x}(x_i, y_i, z_i) \\
& + B_{1,y}(x_i, y_i, z_i)\vec{y}(x_i, y_i, z_i) + B_{1,z}(x_i, y_i, z_i)\vec{z}(x_i, y_i, z_i)\big]
\end{aligned} \tag{2.24}$$

18

$\vec{r}\,'(x, y, z)$ component, which defines one of the axis of local coordinates, is chosen in the direction of the static magnetic field $\vec{B}_0$. The other two components can be chosen arbitrarily such that it is orthogonal to $\vec{r}\,'(x_i, y_i, z_i)$ and each other. In order to represent $\vec{B}_1(x_i, y_i, z_i)$ in an easier way select $\vec{\theta}\,'(x_i, y_i, z_i)$ as in the direction of $\vec{B}_1(x_i, y_i, z_i)$ field projected into the normal plane to $\vec{r}\,'(x_i, y_i, z_i)$. This can be seen in Figure 2.1.
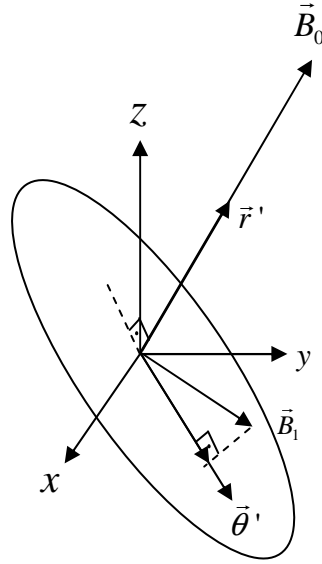
Figure 2.1. Original and local coordinate systems.

In local coordinate system by selecting $\vec{\theta}\,'(x_i, y_i, z_i)$ as above, $\vec{B}_1(x_i, y_i, z_i)$ can be written as

$$B_1(x_i, y_i, z_i, t) = 2B_1^e(t)\cos(\omega_{rf}t + \phi)\Big[B_{1,\vec{\theta}'}(x_i, y_i, z_i)\vec{\theta}\,'(x_i, y_i, z_i)$$
$$+ B_{1,\vec{r}'}(x_i, y_i, z_i)\vec{r}\,'(x_i, y_i, z_i)\Big] \tag{2.25}$$

To solve the effect of the RF magnetic field to the bulk magnetization one more coordinate system transformation has to be defined. This is called rotating frame of reference.

2.1.3. Rotating Frame of Reference Selection to Model Magnetic Resonance Imaging in Inhomogeneous Magnetic Fields

A rotating frame is a coordinate system whose transverse plane is rotating clockwise at an angular frequency ω. This transverse plane is spanned in the local coordinate directional vectors $\vec{\theta}\,'$ and $\vec{\varphi}\,'$. The directional vectors for rotating frame of reference can be named as $\vec{\theta}\,''$, $\vec{\varphi}\,''$, and $\vec{r}\,''$. And the relation between the rotating frame vectors to local frame vectors can be defined as

$$
\begin{cases}
\vec{\theta}\,''(x_i, y_i, z_i, t) = \cos(\omega(x_i, y_i, z_i)t)\vec{\theta}\,'(x_i, y_i, z_i) - \sin(\omega(x_i, y_i, z_i)t)\vec{\varphi}\,'(x_i, y_i, z_i) \\
\vec{\varphi}\,''(x_i, y_i, z_i, t) = \sin(\omega(x_i, y_i, z_i)t)\vec{\theta}\,'(x_i, y_i, z_i) - \cos(\omega(x_i, y_i, z_i)t)\vec{\varphi}\,'(x_i, y_i, z_i) \\
\vec{r}\,''(x_i, y_i, z_i, t) = \vec{r}\,'(x_i, y_i, z_i)
\end{cases}
\quad (2.26)
$$

Also the time derivatives of the unit directional vectors are

$$
\begin{cases}
\dfrac{\partial \vec{\theta}\,''(x_i, y_i, z_i, t)}{\partial t} = \vec{\omega}(x_i, y_i, z_i) \times \vec{\theta}\,''(x_i, y_i, z_i, t) \\[2mm]
\dfrac{\partial \vec{\varphi}\,''(x_i, y_i, z_i, t)}{\partial t} = \vec{\omega}(x_i, y_i, z_i) \times \vec{\varphi}\,''(x_i, y_i, z_i, t) \\[2mm]
\dfrac{\partial \vec{r}\,''(x_i, y_i, z_i, t)}{\partial t} = \vec{\omega}(x_i, y_i, z_i) \times \vec{r}\,''(x_i, y_i, z_i, t)
\end{cases}
\quad (2.27)
$$

where $\vec{\omega}$ is defined by

$$\vec{\omega}(x_i, y_i, z_i) = -\omega(x_i, y_i, z_i)\vec{r}\,''(x_i, y_i, z_i, t) \tag{2.28}$$

and as discussed before

$$\vec{M}(x_i, y_i, z_i, t) = M_{\vec{\theta}'}(x_i, y_i, z_i, t)\vec{\theta}\,'(x_i, y_i, z_i) + M_{\vec{\varphi}'}(x_i, y_i, z_i, t)\vec{\varphi}\,'(x_i, y_i, z_i)$$
$$+ M_{\vec{r}'}(x_i, y_i, z_i, t)\vec{r}\,'(x_i, y_i, z_i) \tag{2.29}$$

and $\vec{M}_{rot}$ can be defined as

$$\vec{M}_{rot}(x_i, y_i, z_i, t) = M_{\vec{\theta}''}(x_i, y_i, z_i, t)\vec{\theta}\,''(x_i, y_i, z_i, t) + M_{\vec{\varphi}''}(x_i, y_i, z_i, t)\vec{\varphi}\,''(x_i, y_i, z_i, t)$$
$$+ M_{\vec{r}''}(x_i, y_i, z_i, t)\vec{r}\,''(x_i, y_i, z_i, t) \tag{2.30}$$

So the relation between $\vec{M}_{rot}$ and $\vec{M}$ in a matrix form is

$$\begin{bmatrix} M_{\vec{\theta}''}(x_i, y_i, z_i, t) \\ M_{\vec{\varphi}''}(x_i, y_i, z_i, t) \\ M_{\vec{r}''}(x_i, y_i, z_i, t) \end{bmatrix} = \begin{bmatrix} \cos(\omega(x_i, y_i, z_i)t) & -\sin(\omega(x_i, y_i, z_i)t) & 0 \\ \sin(\omega(x_i, y_i, z_i)t) & \cos(\omega(x_i, y_i, z_i)t) & 0 \\ 0 & 0 & 1 \end{bmatrix} \begin{bmatrix} M_{\vec{\theta}'}(x_i, y_i, z_i, t) \\ M_{\vec{\varphi}'}(x_i, y_i, z_i, t) \\ M_{\vec{r}'}(x_i, y_i, z_i, t) \end{bmatrix} \tag{2.31}$$

Derivatives of $\vec{M}_{rot}$ and $\vec{M}$ can be related as

$$\frac{d\vec{M}(x_i, y_i, z_i, t)}{dt} = \frac{dM_{\vec{\theta}'}(x_i, y_i, z_i, t)}{dt} \vec{\theta}'(x_i, y_i, z_i)$$
$$+ \frac{dM_{\vec{\varphi}'}(x_i, y_i, z_i, t)}{dt} \vec{\varphi}'(x_i, y_i, z_i) + \frac{dM_{\vec{r}'}(x_i, y_i, z_i, t)}{dt} \vec{r}'(x_i, y_i, z_i) \qquad (2.32)$$

$$\frac{\partial \vec{M}_{rot}(x_i, y_i, z_i, t)}{\partial t} = \frac{\partial M_{\vec{\theta}''}(x_i, y_i, z_i, t)}{\partial t} \vec{\theta}''(x_i, y_i, z_i, t)$$
$$+ \frac{\partial M_{\vec{\varphi}''}(x_i, y_i, z_i, t)}{\partial t} \vec{\varphi}''(x_i, y_i, z_i, t) + \frac{\partial M_{\vec{r}''}(x_i, y_i, z_i, t)}{\partial t} \vec{r}''(x_i, y_i, z_i, t) \qquad (2.33)$$

Then,

$$\frac{d\vec{M}(x_i, y_i, z_i, t)}{dt} = \frac{\partial \vec{M}_{rot}(x_i, y_i, z_i, t)}{\partial t} + \vec{\omega}(x_i, y_i, z_i) \times \vec{M}_{rot}(x_i, y_i, z_i, t) \qquad (2.34)$$

As seen from (2.34), the rate of change in $\vec{M}$, as observed in local coordinate system and the rate of change of $\vec{M}$ as observed in the rotating coordinate system are not equal.

2.1.4. Derived Bloch Equation to Model Magnetic Resonance Phenomena in Inhomogeneous Magnetic Fields

The time-dependent behavior of $\vec{M}$ in the presence of an applied magnetic field is described quantitatively by the Bloch equation. The Bloch equation takes the

general form [1]. For inhomogeneous main and RF magnetic fields with described coordinate system

$$
\begin{aligned}
\frac{d\vec{M}(x_i, y_i, z_i, t)}{dt} = {} & \gamma \vec{M}(x_i, y_i, z_i, t) \times \vec{B}(x_i, y_i, z_i, t) \\
& - \frac{M_{\bar{\theta}'}(x_i, y_i, z_i, t)\vec{\theta}'(x_i, y_i, z_i) + M_{\bar{\varphi}'}(x_i, y_i, z_i)\vec{\varphi}'(x_i, y_i, z_i, t)}{T_2(x_i, y_i, z_i)} \\
& - \frac{\left(M_{\bar{r}'}(x_i, y_i, z_i, t) - M_{\bar{r}'}^0(x_i, y_i, z_i)\right)\vec{r}'(x_i, y_i, z_i, t)}{T_1(x_i, y_i, z_i)}
\end{aligned}
\tag{2.35}
$$

where $M_{\bar{r}'}^0(x_i, y_i, z_i)$ is the thermal equilibrium value for $\vec{M}(x_i, y_i, z_i, t)$ in the presence of $\vec{B}_0(x_i, y_i, z_i)$ only, which is calculated in (2.23). $T_1(x_i, y_i, z_i)$ and $T_2(x_i, y_i, z_i)$ are time constants characterizing the relaxation process of a spin system after it has been disturbed from its thermal equilibrium state. While calculating the effect of RF pulse, the second and the third terms are generally omitted since RF pulse duration is much shorter than $T_1(x_i, y_i, z_i)$ and $T_2(x_i, y_i, z_i)$ [3]. Under these assumptions

$$
\frac{d\vec{M}(x_i, y_i, z_i, t)}{dt} \simeq \gamma \vec{M}(x_i, y_i, z_i, t) \times \vec{B}(x_i, y_i, z_i, t)
\tag{2.36}
$$

By using (2.34), above equation can be written in the rotating frame of reference as

$$\frac{\partial \vec{M}_{rot}(x_i, y_i, z_i, t)}{\partial t} = \gamma \vec{M}_{rot}(x_i, y_i, z_i, t) \times \left(\vec{B}_{rot}(x_i, y_i, z_i, t) + \frac{\vec{\omega}(x_i, y_i, z_i)}{\gamma} \right) \quad (2.37)$$

and effective magnetic field is

$$\vec{B}_{eff} = \left(\vec{B}_{rot}(x_i, y_i, z_i, t) + \frac{\vec{\omega}(x_i, y_i, z_i)}{\gamma} \right) \quad (2.38)$$

Moreover, Bloch equation can be rewritten as

$$
\begin{aligned}
\frac{\partial \vec{M}_{rot}(x_i, y_i, z_i, t)}{\partial t} &= \gamma \vec{M}_{rot}(x_i, y_i, z_i, t) \times \vec{B}_{eff}(x_i, y_i, z_i, t) \\
&\quad - \frac{M_{\vec{\theta}''}(x_i, y_i, z_i, t) \vec{\theta}''(x_i, y_i, z_i) + M_{\vec{\varphi}''}(x_i, y_i, z_i) \vec{\varphi}''(x_i, y_i, z_i, t)}{T_2(x_i, y_i, z_i)} \\
&\quad - \frac{\left(M_{\vec{r}''}(x_i, y_i, z_i, t) - M_{\vec{r}''}^0(x_i, y_i, z_i) \right) \vec{r}''(x_i, y_i, z_i, t)}{T_1(x_i, y_i, z_i)}
\end{aligned}
\quad (2.39)
$$

Using the above equations, the effect of an RF pulse on a spin system can be analyzed and time dependent behavior of $\vec{M}$ can be found. In order to do that RF pulse transverse component is expressed according to the rotating frame of reference in the local coordinate system, which becomes

$$\vec{B}_{1,rot}(x_i, y_i, z_i, t) = \vec{B}_1^e(t)\vec{B}_{1,\bar{\theta}^{\shortmid\shortmid}}(x_i, y_i, z_i)\vec{\theta}\,"(x_i, y_i, z_i) \tag{2.40}$$

Then effective field $\vec{B}_{eff}(x_i, y_i, z_i, t)$ that the nuclear spin system sees in rotating frame of reference is

$$\vec{B}_{eff}(x_i, y_i, z_i, t) = \left(\vec{B}_0(t) - \frac{\omega_{rf}}{\gamma}\right)\vec{r}\,"(x_i, y_i, z_i) + \vec{B}_1^e(t)\vec{\theta}\,"(x_i, y_i, z_i) \tag{2.41}$$

If the RF frequency is equal to resonance frequency then effective magnetic field becomes $\vec{B}_{1,rot}$. Substituting the above result to the Bloch equation with the assumption of short RF application time (τ_p) compared to T_1 and T_2 then

$$\frac{\partial \vec{M}_{rot}(x_i, y_i, z_i, t)}{\partial t} \simeq \gamma \vec{M}_{rot}(x_i, y_i, z_i, t) \times \vec{B}_1^e(t)\vec{\theta}\,"(x_i, y_i, z_i) \tag{2.42}$$

and in scalar form, we have

$$\begin{cases} \dfrac{\partial M_{\bar{\theta}^{\shortmid\shortmid}}(x_i, y_i, z_i, t)}{\partial t} = 0 \\[2mm] \dfrac{\partial M_{\bar{\varphi}^{\shortmid\shortmid}}(x_i, y_i, z_i, t)}{\partial t} = \gamma B_1^e(x_i, y_i, z_i, t)M_{\bar{r}^{\shortmid\shortmid}}(x_i, y_i, z_i, t) \\[2mm] \dfrac{\partial M_{\bar{r}^{\shortmid\shortmid}}(x_i, y_i, z_i, t)}{\partial t} = -\gamma B_1^e(x_i, y_i, z_i, t)M_{\bar{\varphi}^{\shortmid\shortmid}}(x_i, y_i, z_i, t) \end{cases} \tag{2.43}$$

By using the initial conditions of thermal equilibrium which is

$$
\begin{cases}
M_{\theta''}(x_i, y_i, z_i, 0) = 0 \\
M_{\bar{\varphi}''}(x_i, y_i, z_i, 0) = 0 \\
M_{\bar{r}''}(x_i, y_i, z_i, 0) = M^0_{\bar{r}''}(x_i, y_i, z_i)
\end{cases}
\tag{2.44}
$$

then

$$
\begin{cases}
M_{\bar{\theta}''}(x_i, y_i, z_i, t) = 0 \\[2mm]
M_{\bar{\varphi}''}(x_i, y_i, z_i, t) = M^0_{\bar{r}''}(x_i, y_i, z_i)\sin\left(\int_0^t \gamma B_1^e(x_i, y_i, z_i, \tau)d\tau\right) \quad , for\ 0 \le t \le \tau_p \\[4mm]
M_{\bar{r}''}(x_i, y_i, z_i, t) = M^0_{\bar{r}''}(x_i, y_i, z_i)\cos\left(\int_0^t \gamma B_1^e(x_i, y_i, z_i, \tau)d\tau\right)
\end{cases}
\tag{2.45}
$$

As seen from the above equation, the effect of excitation, as observed in the rotating frame, is a precession of the bulk magnetization about the $\vec{\theta}\,''$ axis. Also (2.45) indicates that the final value of magnetization vector, after the RF pulse, depends on the integral of envelope function not the shape of it. This is called flip angle (α) and equals to

$$
\alpha(x_i, y_i, z_i) = \int_0^{\tau_p} \gamma B_1^e(x_i, y_i, z_i, \tau)d\tau
\tag{2.46}
$$

26

This effect of RF pulse can be described as rotation operator, which is defined by the rotation matrix around $\vec{\theta}''$ axis with a variable α as

$$R_{\vec{\theta}''}(\alpha) = \begin{bmatrix} 1 & 0 & 0 \\ 0 & \cos\alpha & \sin\alpha \\ 0 & -\sin\alpha & \cos\alpha \end{bmatrix} \qquad (2.47)$$

For general case, that is $\vec{B}_1$ field which has a $\vec{r}''$ component then $\vec{M}$ can be found by solving (2.42) for that situation again. The rotation of $\vec{M}$ due to RF pulse component along the direction of $\vec{\varphi}''$ is zero, because by selecting $\vec{\theta}''$ with the same direction of $\vec{B}_1$ there is no RF magnetic field in that direction.

$$\begin{bmatrix} M_{\vec{\theta}''}(x_i,y_i,z_i,\tau_p) \\ M_{\vec{\varphi}''}(x_i,y_i,z_i,\tau_p) \\ M_{\vec{r}''}(x_i,y_i,z_i,\tau_p) \end{bmatrix} = R_{\vec{r}''}\left(\theta(x_i,y_i,z_i)-\frac{\pi}{2}\right) R_{\vec{\theta}''}(\alpha(x_i,y_i,z_i))$$

$$R_{\vec{r}''}\left(\frac{\pi}{2}-\theta(x_i,y_i,z_i)\right) \begin{bmatrix} M_{\vec{\theta}''}(x_i,y_i,z_i,0) \\ M_{\vec{\varphi}''}(x_i,y_i,z_i,0) \\ M_{z''}(x_i,y_i,z_i,0) \end{bmatrix} \qquad (2.48)$$

2.1.5. Free Precession and Relaxation Process in Inhomogeneous Magnetic Fields

After a magnetized spin system has been perturbed from its thermal equilibrium by an RF pulse described as above, the system returns to its original equilibrium state in a sufficient time. This process is characterized by a precession of $\vec{M}$ about the $\vec{B}_0$ field with the relaxation processes in longitudinal and transverse

27

components. This relation can be written in rotating frame of reference at the resonance frequency as in scalar form as

$$
\begin{aligned}
\frac{dM_{\vec{r}''}(x_i, y_i, z_i, t)}{dt} &= -\frac{M_{\vec{r}''}(x_i, y_i, z_i, t) - M_{\vec{r}'}^0}{T_1(x_i, y_i, z_i)} \\
\frac{dM_{\vec{\theta}''\vec{\varphi}''}(x_i, y_i, z_i, t)}{dt} &= -\frac{M_{\vec{\theta}''\vec{\varphi}''}(x_i, y_i, z_i, t)}{T_2(x_i, y_i, z_i)}
\end{aligned}
\tag{2.49}
$$

Solving (2.49), time variation of transverse and longitudinal magnetization components can be found. As a note, T_1 is about 0.3 to 2 second and T_2 is about 0.03 to 0.15 seconds in biological tissues.

$$
\begin{aligned}
M_{\vec{r}''}(x_i, y_i, z_i, t) &= M_{\vec{r}'}^0(x_i, y_i, z_i)\left(1 - e^{t/T_1(x_i, y_i, z_i)}\right) + M_{\vec{r}''}(x_i, y_i, z_i, \tau_p)e^{t/T_1(x_i, y_i, z_i)} \\
M_{\vec{\theta}''\vec{\varphi}''}(x_i, y_i, z_i, t) &= M_{\vec{\theta}''\vec{\varphi}''}(x_i, y_i, z_i, \tau_p)e^{t/T_2(x_i, y_i, z_i)}
\end{aligned}
\tag{2.50}
$$

2.1.6. Signal Detection Principles Used in Inhomogeneous Magnetic Fields

FID signal is received by a receiver coil placed near the object to be imaged and signal is received from this coil for a specific time range. Signal detection in MR is based on the Faraday law of electromagnetic induction and the reciprocity principle. The Faraday law of induction states that time varying magnetic flux through the receiver coil induces a voltage that is equal to the rate of change in magnetic flux through the coil. The detection sensitivity of a receiver coil is determined through the principle of reciprocity.

Assume that $\vec{B}_2(x, y, z)$ is the magnetic field at location (x, y, z) produced by a unit direct current flowing in the receiver coil. Then the magnetic flux through the coil by $\vec{M}(x, y, z, t)$ is equal to

$$\Phi(t) = \iiint_{obj} \vec{B}_2(x, y, z) \cdot \vec{M}(x, y, z, t) dxdydz \qquad (2.51)$$

By using Faraday law,

$$V(t) = -\frac{\partial \Phi(t)}{\partial t} = -\frac{\partial}{\partial t} \iiint_{obj} \vec{B}_2(x, y, z) \cdot \vec{M}(x, y, z, t) dxdydz \qquad (2.52)$$

This equation is represented in scalar form as (2.53)

$$V(t) = -\frac{\partial}{\partial t} \iiint_{obj} \left(B_{2,x}(x, y, z) M_x(x, y, z, t) + B_{2,y}(x, y, z) M_y(x, y, z, t) \right.$$
$$\left. + B_{2,z}(x, y, z) M_z(x, y, z, t) \right) dxdydz \qquad (2.53)$$

Since $\vec{B}_2(x, y, z)$ and integral do not depend on time then the derivative term can propagate to $\vec{M}(x, y, z, t)$ term.

$$V(t) = -\iiint_{obj} \left(B_{2,x}(x,y,z)\frac{\partial M_x(x,y,z,t)}{\partial t} + B_{2,y}(x,y,z)\frac{\partial M_y(x,y,z,t)}{\partial t} \right. $$

$$\left. + B_{2,z}(x,y,z)\frac{\partial M_z(x,y,z,t)}{\partial t} \right) dxdydz \qquad (2.54)$$

Changing the coordinate system to local coordinates and discretizing the equation in space assuming that $\vec{B}_2(x,y,z)$ is constant in each voxel (2.54) becomes,

$$V(t) = -\sum_i \left(B_{2,\bar{\theta}'}(x_i,y_i,z_i)\frac{\partial M_{\bar{\theta}'}(x_i,y_i,z_i,t)}{\partial t} + B_{2,\varphi'}(x,y,z)\frac{\partial M_{\varphi'}(x_i,y_i,z_i,t)}{\partial t} \right. $$

$$\left. + B_{2,\bar{r}'}(x_i,y_i,z_i)\frac{\partial M_{\bar{r}'}(x_i,y_i,z_i,t)}{\partial t} \right) \Delta v \qquad (2.55)$$

In the above equation Δv is volume of the voxel. As discussed before T_1 values are in the order of seconds. So that as compared to the free precession of $M_{\bar{\theta}'}$ and $M_{\bar{\varphi}'}$ being much faster than longitudinal relaxation ($\omega_0(x,y,z) \gg T_1(x,y,z)$), the derivative of $M_{\bar{r}'}$ can be ignored.

In order to simplify the equation, define $B_{2,\bar{\phi}'}$ and $B_{2,\bar{\varphi}'}$ in polar coordinates where $\left| B_{2,\bar{\theta}'\bar{\varphi}'} \right|$ corresponds to magnitude and $\phi_{2,\bar{\theta}'\bar{\varphi}}$ to phase. Also $\vec{M}$ can be written in the polar form where $\left| \vec{M}_{\bar{\theta}'\bar{\varphi}'}(x_i,y_i,z_i,0) \right|$ corresponds to magnitude and $\varphi_M(x_i,y_i,z_i)$ corresponds to phase, then

$$M_{\bar{\theta}'}(x_i, y_i, z_i, t) = \left| \vec{M}_{\bar{\theta}'\bar{\varphi}'}(x_i, y_i, z_i, 0) \right| e^{-t/T_2(x_i, y_i, z_i)} \cos\left(-\omega(x_i, y_i, z_i)t + \varphi_M(x_i, y_i, z_i)\right)$$

$$(2.56)$$

$$M_{\bar{\varphi}'}(x_i, y_i, z_i, t) = \left| \vec{M}_{\bar{\theta}'\bar{\varphi}'}(x_i, y_i, z_i, 0) \right| e^{-t/T_2(x_i, y_i, z_i)} \sin\left(-\omega(x_i, y_i, z_i)t + \varphi_M(x_i, y_i, z_i)\right)$$

and the derivatives are equal to

$$\frac{\partial M_{\bar{\theta}'}(x_i, y_i, z_i, t)}{\partial t} = \omega(x_i, y_i, z_i) \left| M_{\bar{\theta}'\bar{\varphi}'}(x_i, y_i, z_i, 0) \right| e^{-t/T_2(x_i, y_i, z_i)} \sin\left(-\omega(x_i, y_i, z_i)t + \varphi_M(x_i, y_i, z_i)\right)$$

$$- \frac{1}{T_2(x_i, y_i, z_i)} \left| M_{\bar{\theta}'\bar{\varphi}'}(x_i, y_i, z_i, 0) \right| e^{-t/T_2(x_i, y_i, z_i)} \cos\left(-\omega(x_i, y_i, z_i)t + \varphi_M(x_i, y_i, z_i)\right)$$

$$(2.57)$$

$$\frac{\partial M_{\bar{\varphi}'}(x_i, y_i, z_i, t)}{\partial t} = \omega(x_i, y_i, z_i) \left| M_{\bar{\theta}'\bar{\varphi}'}(x_i, y_i, z_i, 0) \right| e^{-t/T_2(x_i, y_i, z_i)} \cos\left(-\omega(x_i, y_i, z_i)t + \varphi_M(x_i, y_i, z_i)\right)$$

$$- \frac{1}{T_2(x_i, y_i, z_i)} \left| M_{\bar{\theta}'\bar{\varphi}'}(x_i, y_i, z_i, 0) \right| e^{-t/T_2(x_i, y_i, z_i)} \sin\left(-\omega(x_i, y_i, z_i)t + \varphi_M(x_i, y_i, z_i)\right)$$

Assuming $\omega \gg 1/T_2$, second terms can be neglected in the above equation. Then induced voltage on the receiver coil becomes,

$$V(t) = -\sum_i \left(\omega(x_i, y_i, z_i) \left| B_{2,\bar{\theta}'\bar{\varphi}'}(x_i, y_i, z_i) \right| \left| M_{\bar{\theta}'\bar{\varphi}'}(x_i, y_i, z_i, 0) \right| e^{-t/T_2(x_i, y_i, z_i)} \right.$$

$$\left. \sin\left(-\omega(x_i, y_i, z_i)t + \varphi_M(x_i, y_i, z_i) - \varphi_{2,\bar{\theta}'\bar{\varphi}'}(x_i, y_i, z_i)\right) \right) \Delta v$$

$$(2.58)$$

This is a high frequency signal at the resonance frequency. So while discretizing the signal in time domain for the simulation, special care has to be taken according to the maximum frequency content in the signal.

2.2. Noise Model of Magnetic Resonance Imaging

In this part, first the noise model of magnetic resonance imaging in homogenous magnetic fields is investigated. Afterwards, this noise model is extended to cover the inhomogeneous case.

2.2.1. Noise Model of Magnetic Resonance Imagining in Homogeneous Magnetic Fields

In experiments with homogenous main magnetic fields with different field strengths, signal to noise ratio (SNR) is related to:

$$\psi \propto \frac{B_0^2}{\left(B_0^2 + \alpha B_0^{1/2} \right)^{1/2}} . \tag{2.59}$$

where, ψ is the SNR, B_0 is the main magnetic field strength and α is change in SNR due to RF coil [70, 71]. If B_0 is large compared to α then, the noise originating from the RF coil can be neglected. In order to find intrinsic SNR, first overall system SNR is measured; then effect of electronic losses and noise generated in electronic instrument stage is eliminated. Intrinsic SNR can be calculated using,

$$\psi_S = \frac{\psi_I \left[1 - \frac{Q_L}{Q_E} \right]^{1/2}}{10^{NF/20}} . \tag{2.60}$$

Here, ψ_S is measured SNR, ψ_I is the intrinsic SNR, *NF* is the noise figure of the electronics in decibels, Q_L and Q_E, are loaded and unloaded quality factors of the RF coil, respectively. Edelstein *et al* measured these values for different MRI systems under various main magnetic field strengths [71]. These values are given in table 2.1.

Table 2.1. Measured SNR values for different MRI systems under various main magnetic field strengths. Table is reproduced from [71].

B_0 (T)	ψ_S (ml^{-1}Hz$^{1/2}$)	*NF* (dB)	Q_E	Q_L	ψ_I (ml^{-1}Hz$^{1/2}$)
0.12	944	1.0	240	170	$1.96 \cdot 10^3$
0.5	4,660	2.0	327	89	$6.88 \cdot 10^3$
1.0	9,642	1.7	356	51	$1.27 \cdot 10^4$
1.5	16,730	1.4	431	64	$2.13 \cdot 10^4$

By using these measurements given in table 2.1, a relationship between ψ_I and B_0 strength can be found. The points B_0 strength versus ψ_I is given in Figure 2.2.
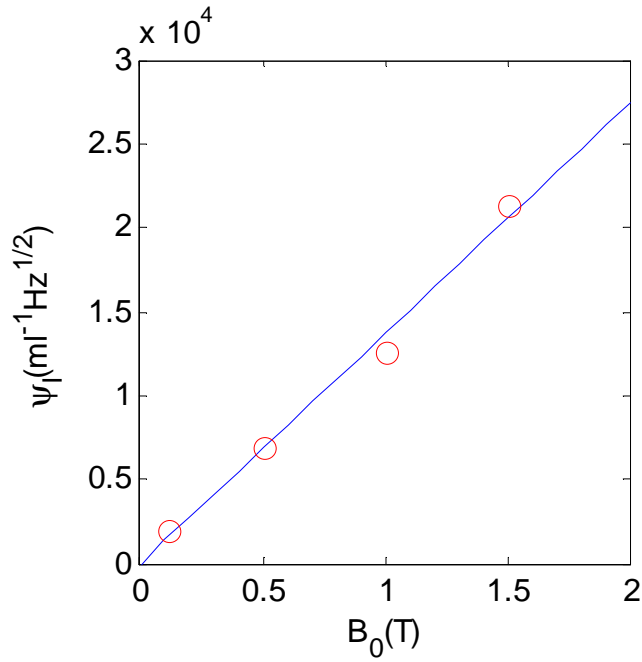
Figure 2.2. Main magnetic field strength versus intrinsic SNR. Red dots represent calculated intrinsic SNR values in Table 2.1 for different main magnetic field strength points. Blue line shows the fitted first order polynomial for these measurement points.

The obtained relation,

$$\psi_I = 1.37 \cdot 10^4 B_0 .$$

(2.61)

is linear as plotted in Figure 2.2. If pixel SNR is calculated for a fixed pulse sequence then,

$$pixel\ SNR = \psi_S \rho V \sqrt{N T_S} \left(1 - e^{-T_R/T_1}\right) e^{-T_E/T_2}$$

(2.62)

where, ρ is proton density relative to water, V is pixel volume, N is number of averages, T_S is sampling time, T_R is repetition time, T_E is echo time, T_1 is longitudinal relaxation time and T_2 is transversal relaxation time.

Pixel SNR can be determined for each pixel by using equations (2.60), (2.61) and (2.62) together with the magnetic field information, test object properties and pulse sequence. Signal strength for every pixel can also be determined by the given information. Using *pixel SNR* and signal strength, noise level can be determined for every pixel and then Gaussian noise with zero mean is added to the signal.

2.3. Proposed FFT Based Image Reconstruction Algorithm for Inhomogeneous Magnetic Fields

In MRI, k-space is filled with Free Induction Decay (FID) signal sampled according to the imaging pulse sequence. In conventional MRI systems, pulse sequences are designed such that the k-space is sampled uniformly [4]. However, in MRI systems with inhomogeneous main magnetic field and nonlinear gradient fields, it is not possible to obtain uniformly sampled k-space data. Therefore, uniform k-space sampling followed by Discrete Fourier Transform (DFT) leads to highly distorted images in inhomogeneous magnetic fields. Consequently, the measured FID signal needs to be corrected. A two-dimensional FOV and a spin echo pulse sequence is adopted in order to simplify the FID signal as

$$FID(m,n) = \sum_{l=1}^{L} B_l M_l e^{j(\omega_l - \omega_0)ndt} e^{j\theta_l(m,n)} . \qquad (2.63)$$

35

where, m is phase encoding number, n is sampling number, L is number of pixels in FOV, M_l is weighted proton density of pixel l, B_l is signal gain associated with pixel l, ω_l is l^{th} pixel resonance frequency due to main and gradient fields, ω_0 is demodulation frequency, dt is signal period and θ_l is phase due to gradient and inhomogeneity in main magnetic field.

This signal can be transformed using two-dimensional DFT. Then by interchanging the summations while taking B_l and M_l out of m and n summation, the result is

$$DFT\left\{FID(m,n)\right\} = \sum_{l=1}^{L} M_l\, B_l \underbrace{\sum_{m=0}^{M-1}\sum_{n=0}^{N-1} e^{j[(\omega_l-\omega_0)ndt+\theta_l(m,n)-un\frac{2\pi}{N}-vm\frac{2\pi}{M}]}}_{C} \qquad (2.64)$$

where, u and v are spatial frequency variables of DFT.

As seen from equation (2.64), C does not depend on M_l and the part labeled as C can be calculated for known magnetic fields, pulse sequence, u and v for every pixel l. If C is named as $a_{vN+u+1,l}$ then,

$$DFT\left\{FID(m,n)\right\}\Big|_{u,v} = \sum_{l=1}^{L} M_l a_{vN+u+1,l} \qquad (2.65)$$

$$a_{vN+u+1,l} = B_l \sum_{m=0}^{M-1}\sum_{n=0}^{N-1} e^{j[(\omega_l-\omega_0)ndt+\theta_l(m,n)-un\frac{2\pi}{N}-vm\frac{2\pi}{M}]} \qquad (2.66)$$

36

When summation in equation (2.66) is written in open form for every u and v pair, a set of linear equations is obtained between DFT of FID signal and weighted proton density values.

This can be written as in open form

$$
\begin{aligned}
FFT(0,0) &= M_1 a_{1,1} + M_2 a_{1,2} + \cdots + M_L a_{1,L} \\
FFT(0,1) &= M_1 a_{2,1} + M_2 a_{2,2} + \cdots + M_L a_{2,L} \\
&\vdots \\
FFT(0,N) &= M_1 a_{N,1} + M_2 a_{N,2} + \cdots + M_L a_{N,L} \\
FFT(1,0) &= M_1 a_{N+1,1} + M_2 a_{N+1,2} + \cdots + M_L a_{N+1,L} \\
&\vdots \\
FFT(M,N) &= M_1 a_{MN,1} + M_2 a_{MN,2} + \cdots + M_L a_{MN,L}
\end{aligned}
\tag{2.68}
$$

Then define A, b, x as follows

$$
b =
\begin{bmatrix}
FFT(0,0) \\
FFT(0,1) \\
\vdots \\
FFT(0,N) \\
FFT(1,0) \\
\vdots \\
FFT(M,N)
\end{bmatrix}
\tag{2.69}
$$

$$A = \begin{bmatrix} a_{1,1} & a_{1,2} & \cdots & a_{1,k} & a_{1,k+1} & \cdots & a_{1,L} \\ a_{2,1} & a_{2,2} & \ddots & a_{2,k} & a_{2,k+1} & \ddots & a_{2,L} \\ \cdots & \cdots & \ddots & \cdots & \cdots & \ddots & \cdots \\ a_{N,1} & a_{N,2} & \cdots & a_{N,k} & a_{N,k+1} & \cdots & a_{N,L} \\ a_{N+1,1} & a_{N+1,2} & \cdots & a_{N+1,k} & a_{N+1,k} & \cdots & a_{N+1,L} \\ \vdots & \vdots & \ddots & \vdots & \vdots & \ddots & \vdots \\ a_{NM,1} & a_{NM,2} & \cdots & a_{NM,k} & a_{NM,k+1} & \cdots & a_{NM,L} \end{bmatrix}$$

(2.70)

$$x = \begin{bmatrix} M_1 \\ M_2 \\ \vdots \\ M_k \\ M_{k+1} \\ \vdots \\ FFT(M,N) \end{bmatrix}$$

(2.71)

and the equation becomes in the form of linear equation

$$Ax = b$$

(2.72)

Solution for the set of linear equations can be found if this equation set is not ill conditioned. If it is ill conditioned then a partial solution can be also found.

CHAPTER 3

FREE INDUCTION DECAY SIGNAL CHARACTERISTICS IN INHOMOGENOUS MAGNETIC FIELDS

In this chapter, magnetic resonance (MR) signal deviation due to inhomogeneity in the main magnetic field is investigated. This analysis is done to understand the effect of inhomogeneity in magnetic field to the signal decay time, the signal energy, and the peak of the signal. In addition, the relation between inhomogeneity in main magnetic field and field of view is investigated.

Using these parameters, suitability of specific MRI hardware designed for inhomogeneous magnetic field can be analyzed. This means that using following analysis, the inhomogeneity tolerance of a specific hardware can be found. Or else, given the inhomogeneity distribution, the hardware design parameters can be selected accordingly.

3.1. Analysis Parameters Used to Characterize Free Induction Decay Signal in Inhomogeneous Magnetic Fields

Some of the parameters used to characterize the FID signal in inhomogeneous main magnetic field are important, like signal energy, peak value, decay time and field of view. These parameters' importance and calculation methods are explained in this part.

3.1.1. Decay Time of Free Induction Decay Signal

The decay time is an important parameter. If signal decays very fast compared to sampling rate of the MRI system then a meaningful signal with sufficient information to reconstruct image cannot be collected.

The FID signal decays with time whether the main magnetic field is homogenous or not. However, the behavior of these two cases are different from each other. For homogenous main magnetic field, the decay in the signal is due to relaxation processes. These relaxation processes are defined by longitudinal and transverse relaxation times and included in Bloch equation.

The longitudinal relaxation is due to proton interactions with lattice. This relaxation is described by a time constant T_1 which implies the rate of change in longitudinal magnetization. This is because perturbed magnetic moments will tend to reach to the minimum energy state. The minimum energy state is reached when the magnetic moment is parallel to the main magnetic field. T_1 values depend on the object or the main magnetic field strength. For biological tissues, the range of T_1 values is about hundreds to thousands of milliseconds for main magnetic field strength larger than 0.01T [3].

The transverse relaxation is due to spin-spin interactions. Spins themselves generate magnetic field. Therefore, total magnetic field on a spin, is combination of main magnetic field and field generated from neighboring spins. Since there is spin variation over the object, the total magnetic field across the sample differs from position to position. Because of this difference in the total magnetic field, spins precess at different frequencies and they lose their synchronization. As a result, the net magnetization and FID signal decreases over time. This relaxation

is described by a time constant T_2. For biological tissues, the range of T_2 values is about ten to hundreds of milliseconds [3]. These relaxation times of different tissues, measured in different main magnetic field strengths, are given in Table 3.1.

Table 3.1. Longitudinal (T_1) and transverse (T_2) relaxation times of different normal tissue types, which are measured in different main magnetic field strengths, are given. This table is reproduced from [72].

Tissue	T_1 (ms)			T_2 (ms)		
	0.06 T	0.1 T	1.5 T	0.06 T	0.1 T	1.5 T
Liver	138	215	340	36	37	30
Muscle	185	259	740	49	28	38
Kidney	214	419	685	56	39	56
Brain	285	399	1361	75	-	149

As seen from Table 3.1 T_2 values are independent from main magnetic field strength. Bottomley *et al.* reports that T_2 values are dependent mainly on tissue type [72]. As seen from the table, T_1 values increase as the main magnetic field increases. This shows there is a relationship between T_1 and main magnetic field strength. Bottomley *et al.* also reports that the dominant factors on T_1 values are tissue type and the main magnetic field strength [72]. If T_1 weighted images are aimed at MRI in an environment where main magnetic field variation is large, the behavior of T_1 has to be taken into consideration.

Continuing from the FID signal decay perspective, the effect of transverse relaxation is dominant because sensitivity of RF receiver coil of MRI system is in the direction of transverse plane and T_2 values are smaller then T_1 values (Table 3.1).

The external main magnetic field inhomogeneity have a significant influence on decay of free induction decay (FID) signal over time. This decay can be defined with a different time constant $T_2^{'}$. The combined time constant is referred to as T_2^{*} and it is equal to

$$\frac{1}{T_2^{*}} = \frac{1}{T_2} + \frac{1}{T_2^{'}} .$$

(3.1)

This decrease can be observed in conventional MRI systems since the main magnetic field assumed to be homogenous although it is practically not homogenous. Furthermore, this effect is more dominant as the inhomogeneity increases in main magnetic field. Thus, the relation between inhomogeneity level and signal decay has to be analyzed. The analysis can be done by determining FID signal analytically and numerically, and then processing it. However, this signal decay not only depends upon inhomogeneity level but also inhomogeneity distribution. To simplify the analysis, constant inhomogeneity distribution with variable inhomogeneity level is assumed.

This analysis is used to relate T_2^{*} to MR system hardware parameters like maximum sampling rate, spatial resolution, SNR and bandwidth of the system. A characteristic FID signal, which is the Electromotive Force (EMF) in the RF receiver, is shown in Figure 3.1. In MRI systems, the signal is demodulated

using quadrature amplitude demodulation technique. This demodulation technique produces two signals. These two signals are converted to digital using analog to digital converters. Afterwards, these two digital outputs are combined to form a single complex signal. If this process is applied to the signal given in Figure 3.1, then the demodulated complex signal is obtained as in Figure 3.2.
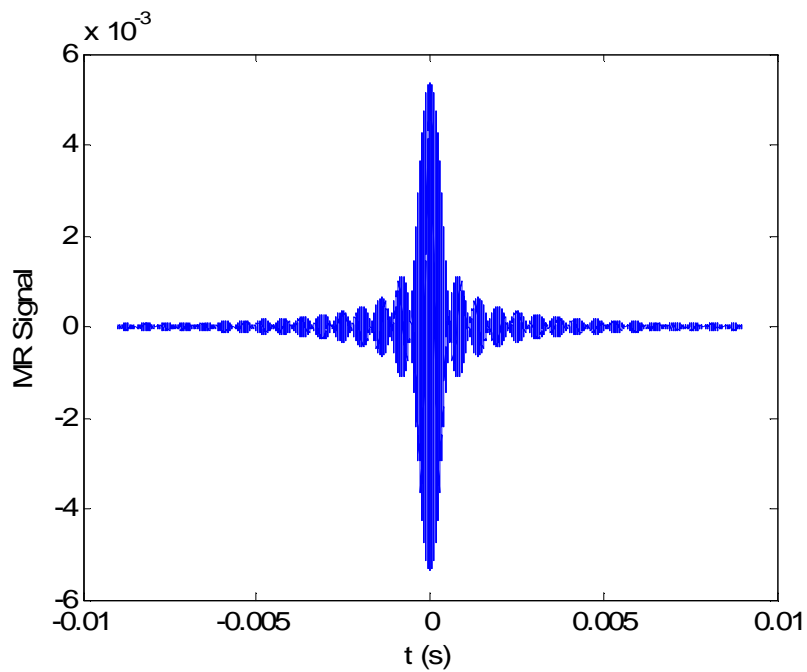
Figure 3.1. Time versus FID signal for an inhomogeneous main magnetic field with linear 100 parts per million (ppm) inhomogeneity is given. The test object selected as uniform with T_2 constant of 20 ms. Signal is obtained using spin echo pulse sequence.
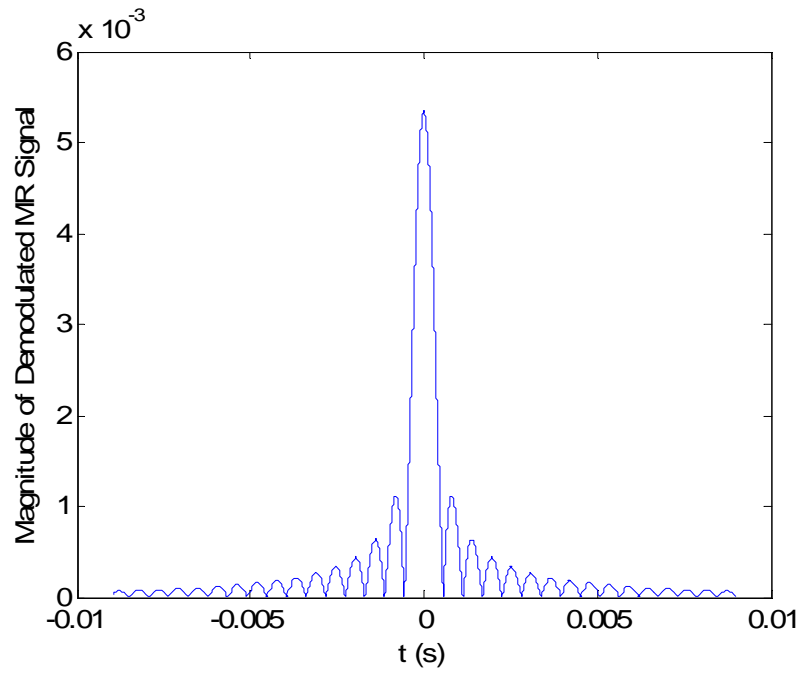
Figure 3.2. Time versus magnitude of demodulated FID signal.

The signal, which is given in Figure 3.2, decays with time, due to inhomogeneity in the main magnetic field and transverse relaxation. This relaxation can be estimated from the demodulated MR signal. The demodulated FID signal depends on object properties, MRI system properties and pulse sequence parameters. To make the analysis possible, the signal can be divided into two parts as,

1: the signal decrease due to T_2^* and

2: rest of the signal:

$$S(t) \approx \underbrace{f(t)}_{2} \underbrace{A e^{-t/T_2^*}}_{1} \tag{3.2}$$

44

To do that first the maximum value of the signal is obtained. Then, the time needed for the signal to decrease to half of its maximum value,

$$S(\frac{t_{fwhm}}{2}) \approx \frac{\max\{S(t)\}}{2} \tag{3.3}$$

is determined as illustrated in Figure 3.3.
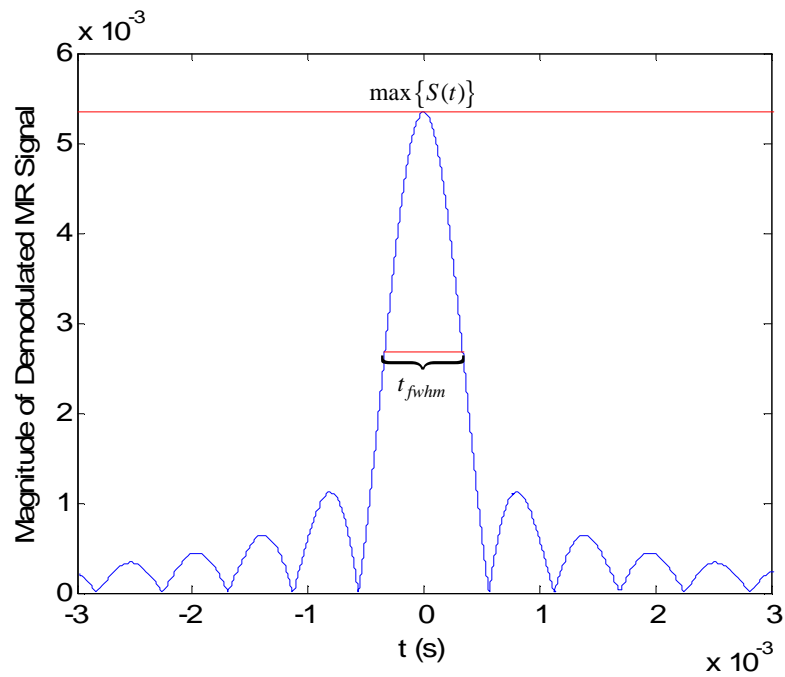
Figure 3.3. Zoomed version of Figure 3.2 with signal maximum and time elapsed when the signal is decreased to half of its maximum.

Assuming f(t) variation is low in (3.1), the signal decay is due to relaxation. Then,

$$S(\frac{t_{fwhm}}{2}) \approx \max\{S(t)\} e^{-\frac{t_{fwhm}}{2T_2^*}} \approx \frac{\max\{S(t)\}}{2} \qquad (3.4)$$

Dividing both sides with $\max\{S(t)\}$ and taking natural logarithm, (3.4) becomes

$$-\frac{t_{fwhm}}{2T_2^*} \approx \ln\left(\frac{1}{2}\right) \qquad (3.5)$$

Rearranging the equation (3.5) to find T_2^*

$$T_2^* \approx \frac{t_{fwhm}}{2\ln(2)} \qquad (3.6)$$

Using the above equation, T_2^* values can be estimated for different levels of inhomogeneity and distributions. These values give information about how fast the signal decays due to main magnetic field inhomogeneity.

As stated before, if signal decays very fast compared to sampling rate of the MRI system then a meaningful signal with sufficient information to reconstruct an image cannot be acquired. From this point of view, a relation between sampling properties (sampling frequency and resolution) of MRI system and the total transverse relaxation time can be found. Using Nyquist theorem and the relation between the sampling frequency and T_2^* , bandwidth of the receiver part can be found.

Assuming an MRI receiver hardware composed of an N_{bit} bit analog to digital converter (ADC) with sampling frequency of f_s and with a gain set to cover the analog voltage range of $[-\max\{S(t)\}, \max\{S(t)\}]$. Using this ADC the FID signal which decays with time constant T_2^* is sampled. If an image is to be reconstructed with N samples, then these samples have to be acquired before the FID signal decays below the resolution of ADC.

To determine the described relation, we should first obtain the ADC's resolution which is equal to

$$dS = \frac{[\max\{S(t)\} - (-\max\{S(t)\})]}{2^{N_{bit}}} \tag{3.7}$$

and the sampling period is equal to

$$dt = \frac{1}{f_s} \tag{3.8}$$

To acquire N samples using analog to digital converter, total time of *(N-1)dt* is required. Assuming (3.2) holds, after a time of *(N-1)dt* passes, the signal decreases to a value

$$S((N-1)dt) \approx \max\{S(t)\}e^{-T_2^*(N-1)dt} \tag{3.9}$$

because of the relaxation processes described by T_2^*. This value has to be larger than dS (right side of the inequality in (3.10)) to detect the signal using the ADC and this relation is given in (3.10).

$$\max\{S(t)\}e^{-(N-1)dt/T_2^*} > \frac{2\max\{S(t)\}}{2^{N_{bit}}} \qquad (3.10)$$

Simplifying the above relation, it is equal to

$$dt < \frac{\ln(2)(N_{bit}-1)T_2^*}{(N-1)}. \qquad (3.11)$$

If (3.11) is written for sampling frequency then

$$f_s > \frac{(N-1)}{\ln(2)(N_{bit}-1)T_2^*}. \qquad (3.12)$$

Using Nyquist theorem, bandwidth of the receiver part (BW_{rcv}) has to satisfy

$$BW_{rcv} > \frac{(N-1)}{2\ln(2)(N_{bit}-1)T_2^*}. \qquad (3.13)$$

3.1.2. Signal Peak of Free Induction Decay Signal

Signal peak is an important parameter for the FID signal, because it gives the information about the strength of the signal. It can be defined as

$$Signal\ peak = \max\{S(t)\}.\tag{3.14}$$

Moreover, it affects MRI hardware parameters like receiver signal gain. As explained in the previous subsection FID signal depends on object, MRI system and pulse sequence. Some pulse sequences like spin echo pulse sequence can recover some effects of field inhomogeneity in FID signal [4]. As such, these pulse sequences are preferred in MRI in inhomogeneous main magnetic fields [43]. If spin echo pulse sequence is used for the analysis, then the signal peak value is not dominantly related to main magnetic field inhomogeneity. However, there is a weak relation between signal peak and main magnetic field inhomogeneity. This is because magnetization vector magnitude is related to main magnetic field strength. This relation is explained in the previous chapter and it is equal to

$$\left|\vec{M}(x_i, y_i, z_i, t)\right| = \frac{\gamma^2 \hbar^2 \left|\vec{B}_0(x_i, y_i, z_i)\right|}{4KT_s} N_s(x_i, y_i, z_i).\tag{3.15}$$

These magnetization vectors generate FID signal, so if the magnetic field variation is large then signal peak can vary.

3.1.3. Energy of Free Induction Decay Signal

Signal energy is an important parameter and it has to be taken into account during the analysis. As the demodulated FID signal is complex, the energy of the signal can be defined as

$$Signal\ energy = \int\limits_{<T_{acq}>} |S(t)|^2\ dt .$$

(3.16)

Signal energy is closely related to the signal peak and relaxation time constant, which are explained in above subsections. Therefore, the same variables affect the signal energy.

3.1.4. Field of View and Image Resolution

Field of view (FOV) is defined as distance in one-dimension, area in two-dimensions or volume in three-dimensions, which will be imaged. For MRI in homogeneous magnetic field, FOV is a rectangular image. For inhomogeneous case, FOV is directly related to main magnetic field strength and gradient field strength. Again, the resolution of the reconstructed image has a close relationship with FOV. As FOV decreases resolution increases.

For this analysis, assume that RF excitation coil has an orthogonal component to main magnetic field in imaging volume and off-resonance excitation effects are negligible. Then the FOV depends to main magnetic field strength distribution,

RF center frequency (f_c), and RF field bandwidth (BW_{RF}). The relation is given in (3.17).

$$FOV = \left\{ (x, y, z) \middle| \left(f_c - \frac{BW_{RF}}{2} \right) < \gamma \left| \vec{B}_0(x, y, z) \right| < \left(f_c + \frac{BW_{RF}}{2} \right) \right\} \qquad (3.17)$$

FOV is related to BW_{RF}. But for the MRI system there is another bandwidth limit which is BW_{rcv}. This is the receiver bandwidth limit. Receiver bandwidth is related to the hardware of the receiver part and sampling frequency of the signal.

3.2. One-Dimensional Analysis of Free Induction Decay Signal in Inhomogeneous Main Magnetic Field

To make one-dimensional analysis of FID signal in inhomogeneous main magnetic field some of the parameters have to be set.

Assume that:

1. Main magnetic field direction is in *z*-axis, and main magnetic field strength varies linearly in *x* direction.

$$\vec{B}_0(x) = \left(B_{0mean} + B_{0slope} x \right) \vec{a}_z$$

2. Single RF coil is used for excitation and reception. The magnetic field is in the direction of *x* and uniform. Perfect 90º and 180º pulses are assumed.

$$\vec{B}_1(x) = \vec{B}_2(x) = B_1 \vec{a}_x$$

3. Test object is uniform. Object's proton density is equal to one relative to water, T_2 value is 20 ms and T_1 value is 1 s.

$$\rho_{relative}(x) = 1$$
$$T_1(x) = 1\ s$$
$$T_2(x) = 20\ ms$$

4. Spin echo pulse sequence with pulse repetition time of 6 s and echo time of 22 ms and acquisition time of 20 ms.

$$T_R = 6\ s$$
$$T_E = 22\ ms$$
$$T_{acq} = 20\ ms$$

3.2.1. Analytical Results for Free Induction Decay Signal in Inhomogeneous Main Magnetic Field

After the above assumptions, first the magnetization vector magnitude has to be determined. Using (2.23), assumptions 1 and 3, magnetization vector magnitude at thermal equilibrium is equal to

$$\left| \vec{M}^0(x) \right| = \frac{\gamma^2 \hbar^2 N_s}{4KT_s} \left(B_{0mean} + B_{0mean} x \right) \tag{3.18}$$

The magnetization vector direction is the same with main magnetic field direction in thermal equilibrium, so magnetization vector direction is in z.

The magnetization vector, which is in thermal equilibrium, is exited with an ideal 90º RF pulse. After that, $T_E/2$ time is waited and then 180º RF pulse is applied. So that using (2.31) and (2.48) resultant vector can be found. For this case in (2.31) the r' is equal to z, θ' is equal to x and φ' is equal to y. Then for our case the FID signal is equal to

$$V(t) = -\int_{-x_0}^{x_0} \left(B_{2,x}(x)\frac{\partial M_x(x,t)}{\partial t} + \underbrace{B_{2,y}(x)}_{0}\frac{\partial M_y(x,t)}{\partial t} + \underbrace{B_{2,z}(x)}_{0}\frac{\partial M_z(x,t)}{\partial t} \right) dx \qquad (3.19)$$

In the above equation $B_{2,x}(x)$ is equal to B_1. The derivative of magnetization vector can be obtained using (2.36), and it is equal to

$$\frac{d\vec{M}(x,t)}{dt} = \gamma\vec{M}(x,t)\times\vec{B}_0(x) . \qquad (3.20)$$

This is because no extra field is applied at that time. Using $\vec{B}_0(x)$ is in the direction of z, the (3.20) becomes

$$\frac{d\vec{M}(x,t)}{dt} = \underbrace{\left[\gamma B_{0,z}(x)M_y(x,t) \right]\hat{a}_x}_{x\ component} + \left[\gamma B_{0,z}(x)M_x(x,t) \right]\hat{a}_y \qquad (3.21)$$

and signal becomes

53

$$V(t) = -\int_{-x_0}^{x_0} \left(B_2 \left[\gamma B_0(x) M_y(x,t) \right] \right) dx \qquad (3.22)$$

Using (2.56) the magnetization vector is equal to

$$M_y(x,t) = \left| \vec{M}_{xy}(x,0) \right| e^{-t/T_2(x)} \cos\left(-B_0(x)t\right) \qquad (3.23)$$

Where $\left| \vec{M}_{xy}(x,0) \right|$ is equal to magnetization vector magnitude in thermal equilibrium which is given in (3.18). Then,

$$V(t) = -B_2 \frac{\gamma^3 \hbar^2 N_s}{4KT_s} e^{-t/T_2} \int_{-x_0}^{x_0} \left(\left[\left(B_{0mean} + B_{0slope}x \right)^2 \cos\left(-\left(B_{0mean} + B_{0slope}x \right)t \right) \right] \right) dx \qquad (3.24)$$

The integral is equal to

$$V(t) = -B_2 \frac{\hbar^2 N_s}{4KT_s B_{0slope} t^3} e^{-t/T_2}$$

$$
\begin{aligned}
\Big[&\sin(-\gamma B_{0slope} t x_0 + \gamma B_{0mean} t)\gamma^2 B_{0slope}^2 t^2 x_0^2 \\
&-2\sin(-\gamma B_{0slope} t x_0 + \gamma B_{0mean} t)\gamma^2 B_{0slope} t^2 x_0 B_{0mean} \\
&+\sin(-\gamma B_{0slope} t x_0 + \gamma B_{0mean} t)\gamma^2 B_{0mean}^2 t^2 \\
&-2\sin(-\gamma B_{0slope} t x_0 + \gamma B_{0mean} t) \\
&-2\cos(-\gamma B_{0slope} t x_0 + \gamma B_{0mean} t)\gamma\ B_{0slope} t\ x_0 \\
&+2\cos(-\gamma B_{0slope} t x_0 + \gamma B_{0mean} t)\gamma\ B_{0mean} t\ x_0 \\
&-\sin(-\gamma B_{0slope} t x_0 + \gamma B_{0mean} t)\gamma^2 B_{0slope}^2 t^2 x_0^2 \\
&-2\sin(-\gamma B_{0slope} t x_0 + \gamma B_{0mean} t)\gamma^2 B_{0slope}^2 t^2 x_0 B_{0mean} \\
&-\sin(\gamma B_{0slope} t x_0 + \gamma B_{0mean} t)\gamma^2 B_{0mean}^2 t^2 \\
&+2\sin(\gamma B_{0slope} t x_0 + \gamma B_{0mean} t) \\
&-2\cos(\gamma B_{0slope} t x_0 + \gamma B_{0mean} t)\gamma\ B_{0mean} t\ x_0 \\
&-2\cos(\gamma B_{0slope} t x_0 + \gamma B_{0mean} t)\gamma\ B_{0mean} t\ \Big]
\end{aligned}
$$

(3.25)

Using the above equation, the analytical result can be found for different levels of inhomogeneity. Inhomogeneity level in the main magnetic field is changed using B_{0slope}. The range is selected as [10^{-5}, 10^{-1}], and the steps of B_{0slope} is selected logarithmic. The mean of the main magnetic field strength is selected as 0.15 T. The half of object size (x_0) is equal to 7.5 cm. For these parameters, the demodulated FID signals' magnitude are given in Figure 3.4.
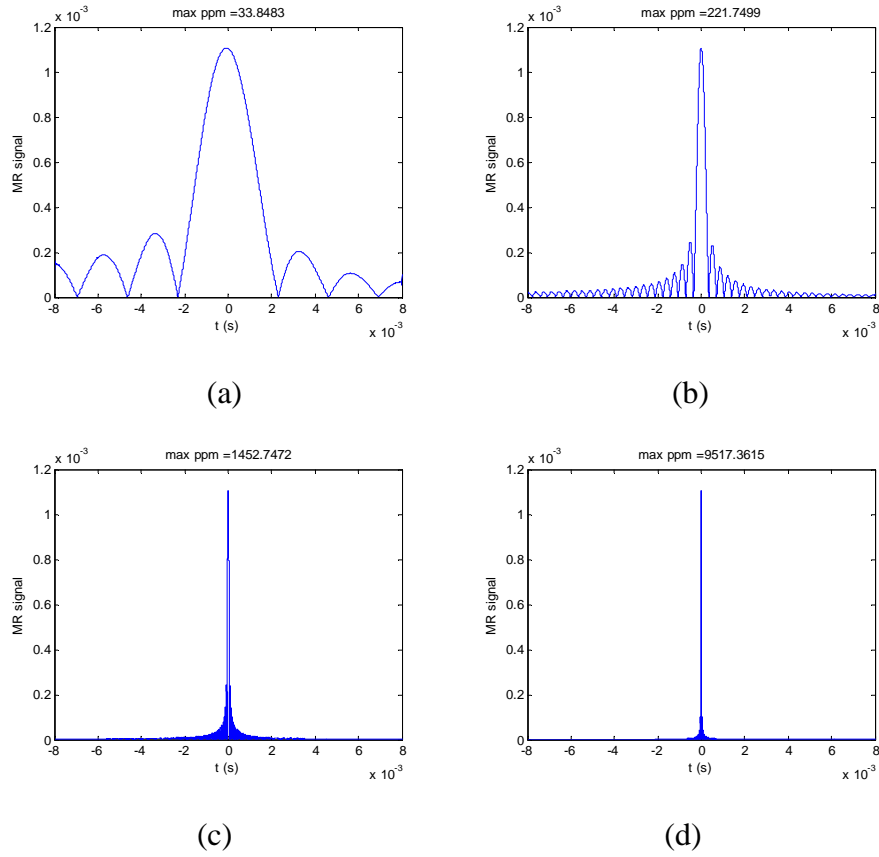
Figure 3.4. Demodulated FID signal for different levels of inhomogeneity for one-dimensional case is given. In these plots, t = 0 corresponds to echo time T_E. (a) $B_{0slope} = 6.55 \cdot 10^{-5}$, which corresponds to 33.8 ppm (b) $B_{0slope} = 4.29 \cdot 10^{-4}$, which corresponds to 222 ppm (c) $B_{0slope} = 2.81 \cdot 10^{-3}$, which corresponds to $1.45 \cdot 10^3$ ppm (d) $B_{0slope} = 18.3 \cdot 10^{-3}$, which corresponds to $9.52 \cdot 10^3$ ppm.

As seen from Figure 3.4 the demodulated FID signal is plotted for different inhomogeneity levels. From these plots as the inhomogeneity level increases, the signal decay increases, peak value does not change very much, and energy decreases. Using the procedure explained in previous sub-section, one can find the relation between inhomogeneity and relaxation time constant. The plots relating inhomogeneity level versus total relaxation time, peak and energy are given in Figure 3.5, 3.6 and 3.7.
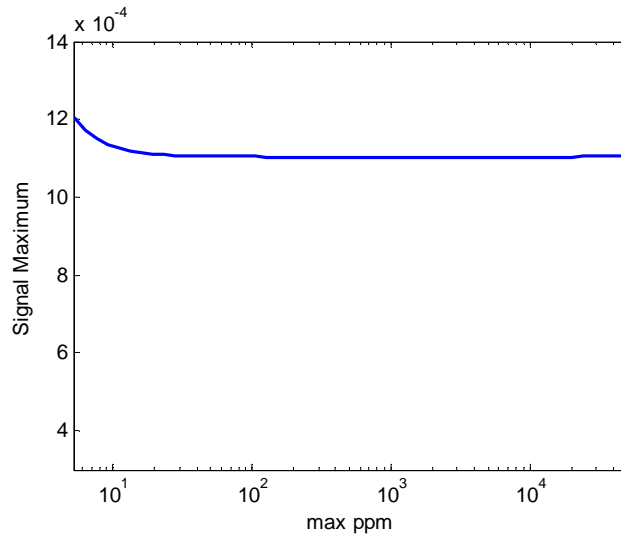
Figure 3.5. Inhomogeneity level versus demodulated FID signals' maximum values plot is given for one-dimensional case. Values are calculated from analytical FID signals.

As seen from the Figure 3.5, inhomogeneity level has an effect on the signal peak. There is a small decrease in the signal peak level when inhomogeneity level increases. This decrease is about 10%. There are three reasons for that. First, for demodulation a low pass filter is used which has the following effect on demodulated signal: as the inhomogeneity increases the bandwidth of the signal increases too and the filter attenuates some of the signal content. Second, as the magnetic field distribution changes, the magnetization vector magnitude and precession frequency changes too. Due to that, both the total signal and the signal peak changes. Third, the signal maximum occurs at the time of T_E, and integral result given in (3.25) has a 0/0 uncertainty at that time instant. To overcome this problem, time is selected as $T_E+dt/1000$ instead of T_E. Therefore, signal peak may vary.
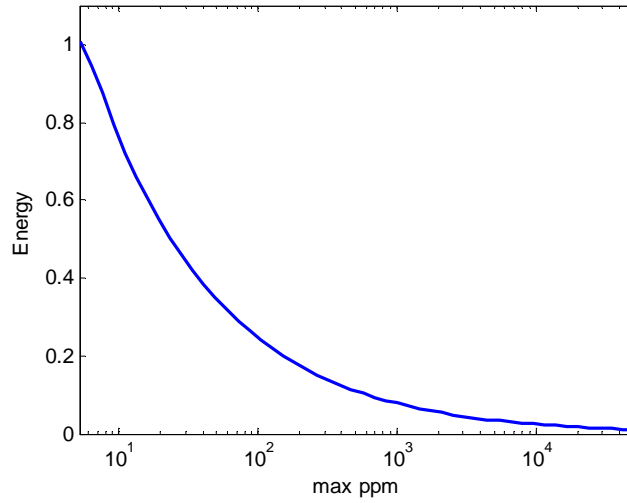
Figure 3.6. Inhomogeneity level versus demodulated FID signals' normalized energy plot is given for one-dimensional case. Values are calculated from analytical FID signal.

As seen from the Figure 3.6, inhomogeneity level severely affects the energy of the signal. This is expected because as the inhomogeneity level increases the precession frequency of the magnetization vectors along the object changes. This station results a loss of synchronization and loss of the energy of the signal.
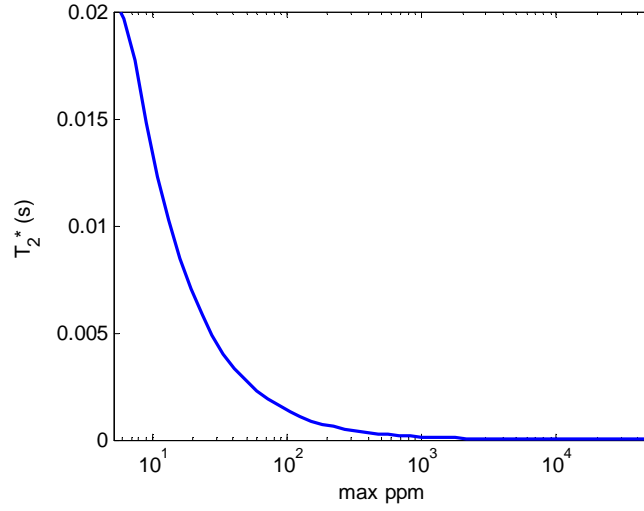
Figure 3.7. Inhomogeneity level versus demodulated FID signals' total transverse relaxation time constant plot is given for one-dimensional case. Values are calculated using analytical FID signal.

As seen from Figure 3.7, the total decay time of the FID signals affected severely for large inhomogeneity levels. The plot is similar to energy of FID signal change. As inhomogeneity increases, the effect of the transverse relaxation due to inhomogeneity in the main magnetic field increases. The reason of the signal decay is the loss of synchronization in magnetization vectors as the time passes. Furthermore, if the inhomogeneity levels are small then the dominant signal decay is due to transverse relaxation of the sample. These results are compatible with the (3.1), which describes the total relaxation. Also for our case $T_R \gg T_1$ then T_1 values does not have a dominant affect on the FID signal.

Using the above result given in Figure 3.7, transversal relaxation and sampling period of the ADC can be found. To do that, assume the MRI receiver part has a 12 bit ADC and reconstruction of an image with 31 pixels is aimed. Using (3.11), inhomogeneity level versus sampling period relation can be found. As

seen from (3.11) and from Figure 3.8, as inhomogeneity level increases, sampling period degreases. This is because, inhomogeneity affects the transverse relaxation, transverse relaxation affects the sampling period.
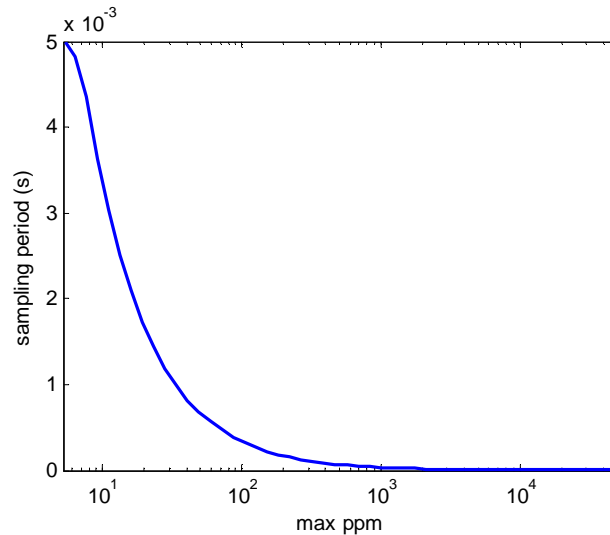
Figure 3.8. Inhomogeneity level versus maximum sampling period needed is given for one-dimensional case. Assumptions are MRI receiver part has a 12 bit analog to digital converter and 31 pixel image is reconstructed. Values are calculated using analytical FID signal.

From sampling period information, it is easy to calculate the sampling frequency as shown in Figure 3.9. As seen from the figure, for high inhomogeneity levels the sampling frequency is directly related. However, for low inhomogeneity levels, the effect of transverse relaxation due to inhomogeneity is less.

60

It is concluded that, if the sampling frequency of the system is larger than the values is plotted in Figure 3.9, then this system is capable of measuring the signal.
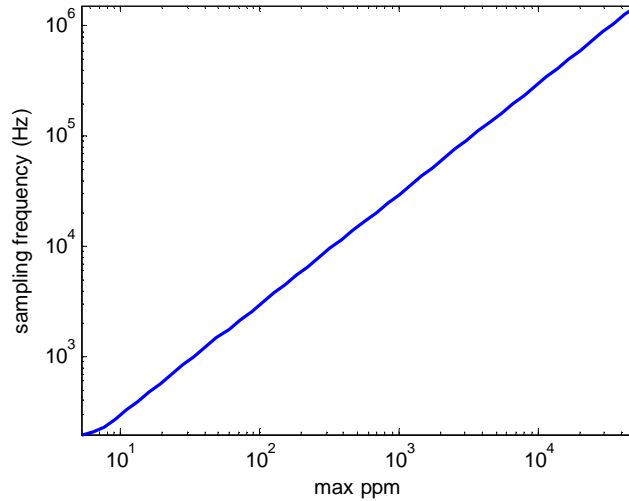
Figure 3.9. Inhomogeneity level versus minimum sampling frequency needed is given for one-dimensional case. Assumptions are MRI receiver part has a 12 bit analog to digital converter and 31 pixel image is reconstructed. Values are calculated using analytical FID signal.
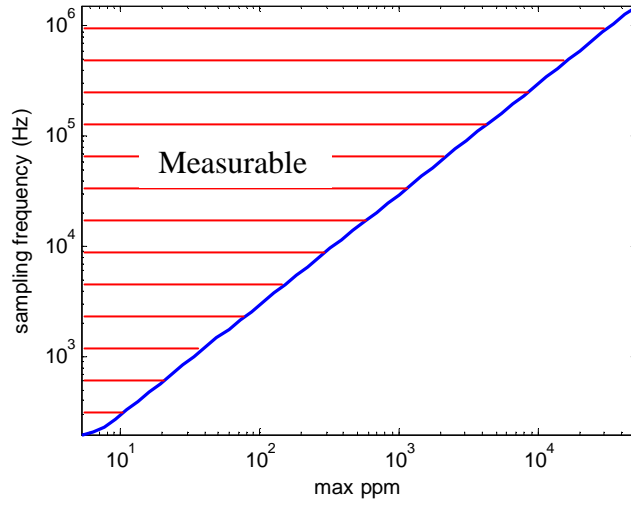
Figure 3.10. Inhomogeneity level versus sampling frequency needed to measure the signal for one-dimensional case. Assumptions are MRI receiver part has a 12 bit analog to digital converter and 31 pixel image is reconstructed. Values are calculated using analytical FID signal.
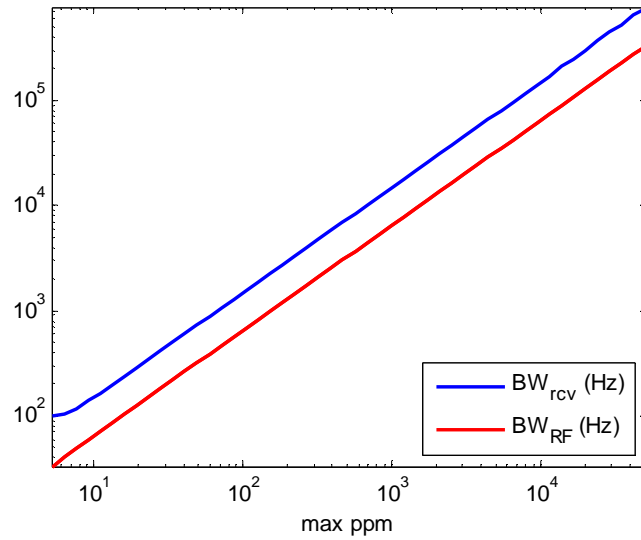
Figure 3.11. Inhomogeneity level versus Bandwidth of receiver and Bandwidth of RF is given for one-dimensional case. Assumptions are: MRI receiver part has a 12 bit analog to digital converter and 31 pixel image is reconstructed. Values are calculated using analytical FID signal.

This plot gives information about the inhomogeneity level and RF field bandwidth. Since the whole object is excited, it is directly related to FOV. Object size is equal to [-75 mm, 75 mm]. Also, N is equal to 31, so the resolution of the MR image is 5mm. Also, the RF bandwidth used to excite the sample is smaller than the bandwidth of receiver. This means that receiver part bandwidth does not affect the FOV.

The same analysis are done for linearly varying main magnetic field in the range of $[10^{-4}, 10^{-1}]$. The results are given in Figure 3.12. The results are the same with the logarithmic case.

(a)   (b)

(c)   (d)

(e)   (f)
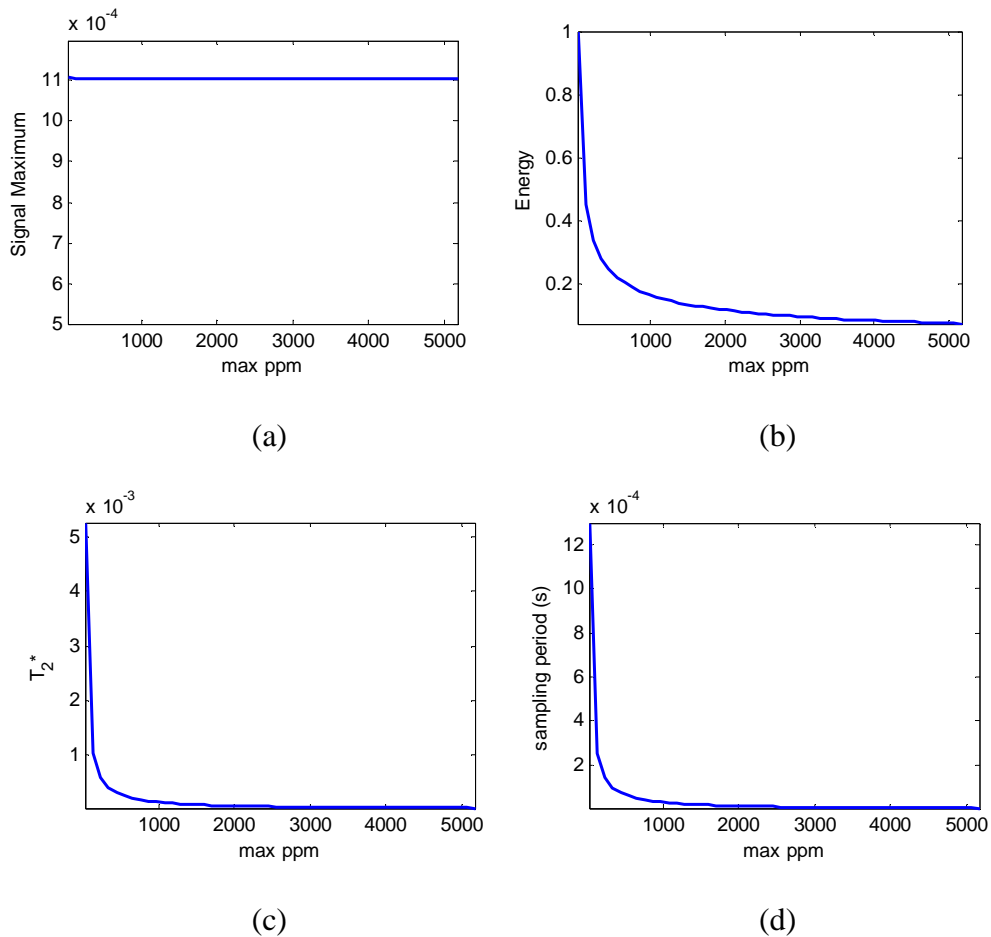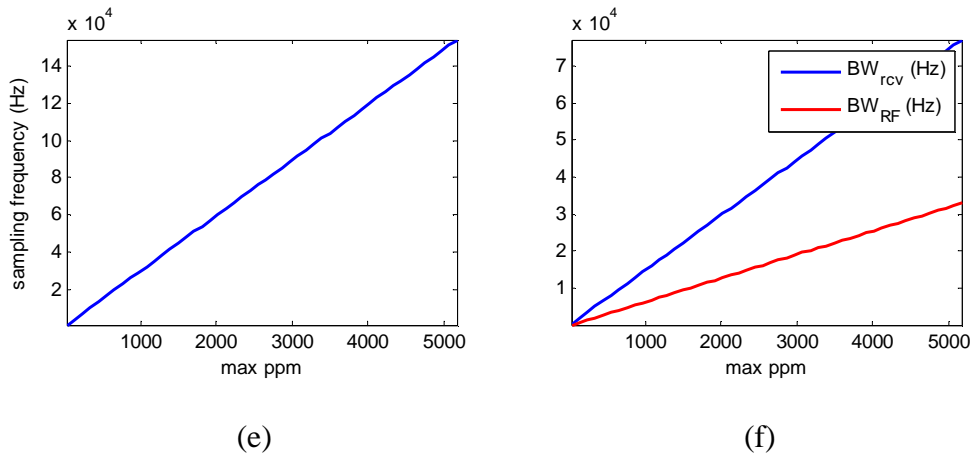
Figure 3.12. Inhomogeneity level versus (a) Signal maximum, (b) Energy, (c) total longitudinal time constant, (d) maximum sampling period, (e) minimum sampling frequency, (f) bandwidth of RF and receiver is given. Results are obtained from numerical results.

3.2.2. Numerical Results for Free Induction Decay Signal in Inhomogeneous Main Magnetic Field

In subsection 3.2.1 results are obtained using analytical analysis. To verify and test the developed numerical model explained in previous chapter same results are obtained. The same assumptions given in section 3.2 are used for numerical model. The results are similar to the analytical results given in 3.2.1. Results obtained analytically (Figure 3.12) and from the numerical model (Figure 3.13) has maximum difference in the peak value is 2.6%, for the relaxation time constant, maximum difference is 4.3%, And for the energy, it is 3.8%. These differences in the results are due to the discretization of the domain into voxels and assumption of uniform magnetic field within the voxel.
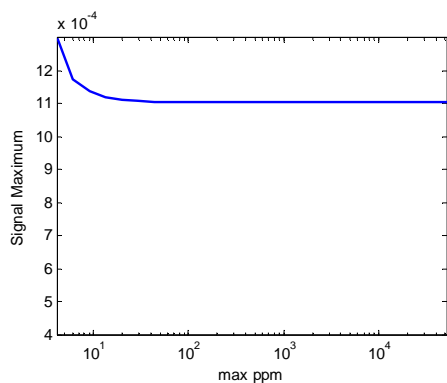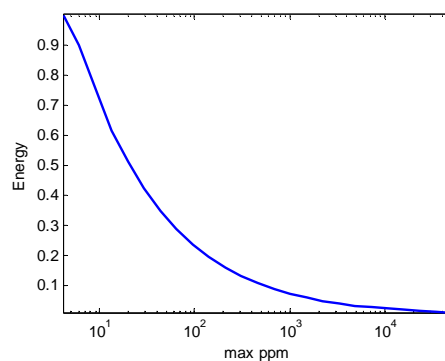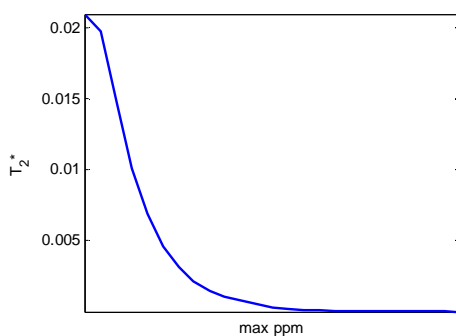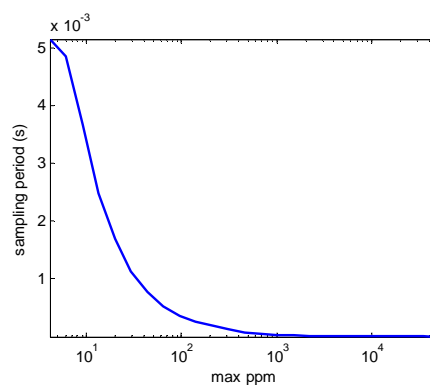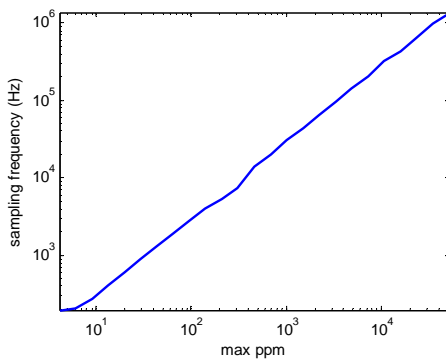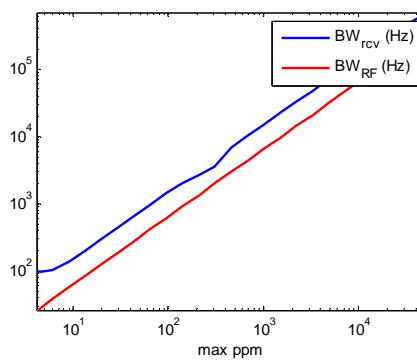
Figure 3.13. Inhomogeneity level versus (a) Signal maximum, (b) Energy, (c) total longitudinal time constant, (d) maximum sampling period, (e) minimum sampling frequency, (f) bandwidth of RF and receiver is given. Results are obtained from numerical FID signal.

3.3. Two-Dimensional Analysis of Free Induction Decay Signal in Inhomogeneous Main Magnetic Field

To make two-dimensional analysis of FID signal in inhomogeneous main magnetic field, values of some of the parameters have to be set *a priori*.

Assuming that:

1. Main magnetic field direction is in *z*-axis, and main magnetic field strength varies linearly in *x* and *y* direction.

$$\vec{B}_0(x, y) = \left(B_{0mean} + B_{0slopex}x + B_{0slopey}y \right)\vec{a}_z$$

2. Single RF coil is used for excitation and reception. The magnetic field is in the direction of *x* and uniform. Perfect 90° and 180° pulses are assumed.

$$\vec{B}_1(x, y) = \vec{B}_2(x, y) = B_1\vec{a}_x$$

3. Frequency gradient field is in the direction of *z*. It is linearly varying in *x* direction.

$$\vec{G}_{frq}(x, y) = G_{frq}x\vec{a}_z$$

4. Test object is uniform. Object's proton density is equal to one relative to water, T_2 value is 20 ms and T_1 value is 1 s.

$$\rho_{relative}(x, y) = 1$$
$$T_1(x, y) = 1 \, s$$
$$T_2(x, y) = 20 \, ms$$

5. Spin echo pulse sequence with pulse repetition time of 6 s and echo time of 22 ms and acquisition time of 20 ms.

$$T_R = 6 \ s$$
$$T_E = 22 \ ms$$
$$T_{acq} = 20 \ ms$$

Since the problem is two-dimensional, analytic formulation of the signal cannot be found. So that, only the numerical results are presented here.

3.3.1 Numerical Results for Free Induction Decay Signal in Inhomogeneous Main Magnetic Field

Similar to the one-dimensional case the FID signals are obtained based on the assumptions given in section 3.2 and the numerical model. The main difference from one-dimensional case is existence of the gradient during data acquisition. Using numerical model FID signal are obtained for different levels of inhomogeneity in main magnetic field for both direction. By analyzing this FID signals, peak values, energy and relaxation time constants are obtained. The results are tabulated and presented in three-dimensional plots.
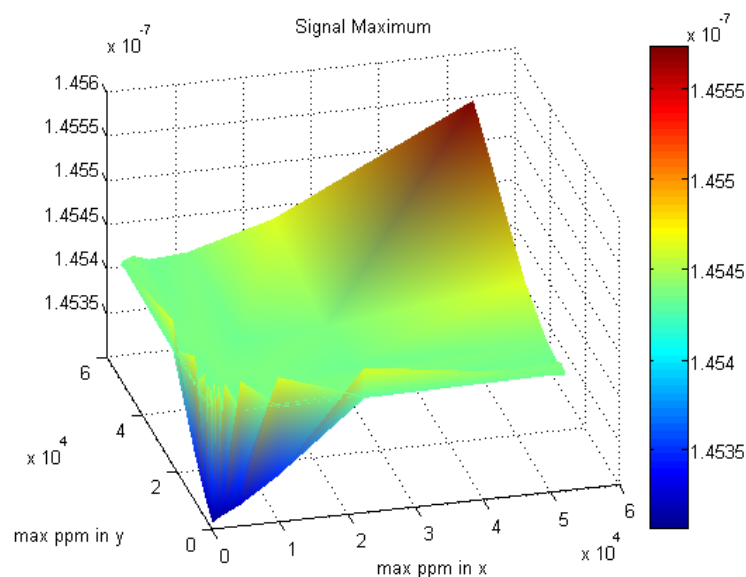
Figure 3.14. Inhomogeneity level versus demodulated FID signals' maximum value plot is given for two-dimensional case. Values are calculated from numerical FID signals.

As seen from Figure 3.14, as inhomogeneity level increases the signal peak degreases. The result is similar for one-dimensional case. However, signal peak variation is small (0.18%) compared to the one-dimensional case. This can be related to, constant magnetic field assumption for every pixel and the gradient field application during signal reception.

In Figure 3.15, inhomogeneity versus normalized energy plot is given. As inhomogeneity level in x direction or in y direction increases, signal energy decreases. Again, this is an expected result since the magnetization vectors are lost their synchronization due to inhomogeneity. Also in Figure 3.16, decay time constant is obtained. There is a jump in decay time constant graph. This jump occurs because at low inhomogeneity in main magnetic field, signal decays due to frequency encoding gradient. From these decay times, minimum sampling

frequency is obtained. The same jump occurs in frequency graph in Figure 3.17. After that the same plot. *i.e.* inhomogeneity level in *x* and *y* direction versus minimum sampling frequency graph is given in figure 3.18. But, for this case the ppm levels logarithm versus sampling frequency is plotted. Also, a plane added to show the tolerable inhomogeneity levels for 1MHz ADC. The results are tabulated in Table 3.2.
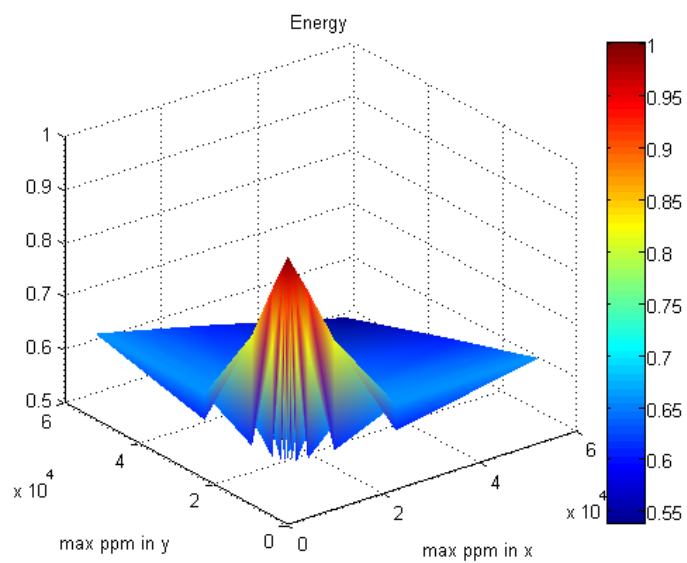
Figure 3.15. Inhomogeneity level versus demodulated FID signals' normalized energy plot is given for two-dimensional case. Values are calculated from analytical FID signal.
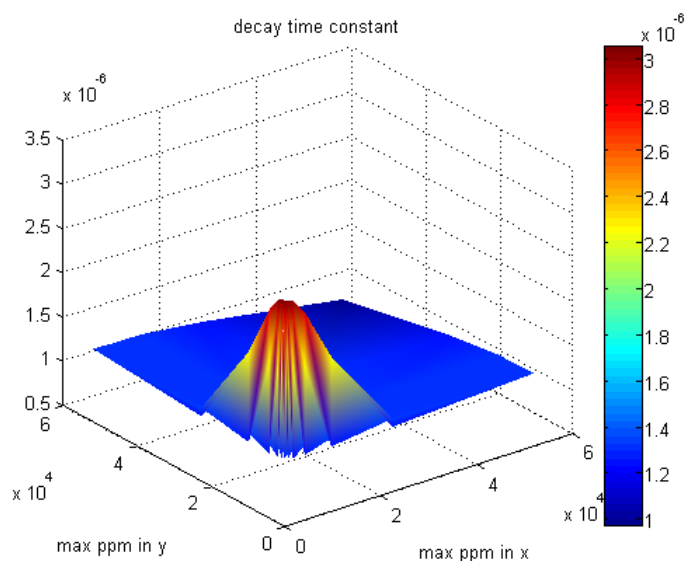
Figure 3.16. Inhomogeneity level versus demodulated FID signals' decay time constant plot is given for two-dimensional case. Values are calculated from analytical FID signal.
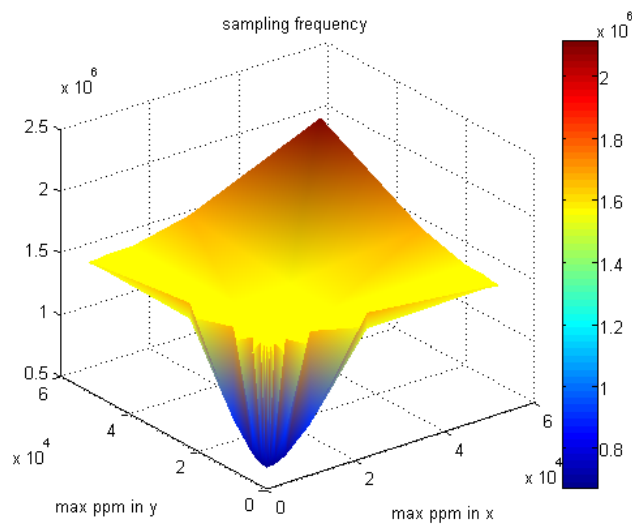
Figure 3.17. Inhomogeneity level versus minimum sampling frequency needed is given for two-dimensional case. Assumptions are MRI receiver part has a 12 bit analog to digital converter and 31x31 pixel image is reconstructed. Values are calculated using analytical FID signal.
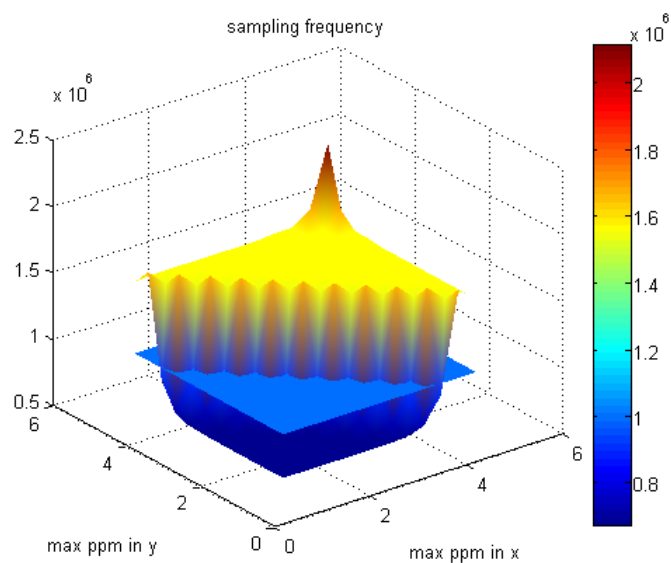
Figure 3.18. Inhomogeneity level in logarithmic scale versus sampling frequency needed to measure the signal for two-dimensional case. Assumptions are MRI receiver part has a 12 bit analog to digital converter and 31x31 pixel image is reconstructed. The plane shows the limit is at 1MHz. Values are calculated using analytical FID signal.

Table 3.2. Inhomogeneity level in *x* and *y* direction versus time constant and minimum sampling frequency needed is given.

|	ppm in *x* → ppm in *y* ↓	5.17	11.9	27.6	63.7	147	340	785	$1.81 \cdot 10^3$	$4.19 \cdot 10^3$	$9.68 \cdot 10^3$	$22.3 \cdot 10^3$	$51.6 \cdot 10^3$
T_2*	5.17	3,04E-6	3,05E-6	3,05E-6	3,05E-6	3,05E-6	3,05E-6	3,04E-6	3,02E-6	2,85E-6	2,25E-6	1,23E-6	1,33E-6
fs		6,74E+5	6,71E+5	6,71E+5	6,71E+5	6,71E+5	6,71E+5	6,74E+5	6,79E+5	7,19E+5	9,11E+5	1,66E+6	1,54E+6
T_2*	11.9	3,05E-6	3,05E-6	3,05E-6	3,05E-6	3,05E-6	3,04E-6	3,02E-6	2,85E-6	2,25E-6	1,23E-6	1,33E-6	1,32E-6
fs		6,71E+5	6,71E+5	6,71E+5	6,71E+5	6,71E+5	6,74E+5	6,79E+5	7,19E+5	9,11E+5	1,66E+6	1,54E+6	1,55E+6
T_2*	27.6	3,05E-6	3,05E-6	3,05E-6	3,05E-6	3,04E-6	3,02E-6	2,85E-6	2,25E-6	1,23E-6	1,33E-6	1,32E-6	1,32E-6
fs		6,71E+5	6,71E+5	6,71E+5	6,71E+5	6,74E+5	6,79E+5	7,19E+5	9,11E+5	1,66E+6	1,54E+6	1,55E+6	1,55E+6
T_2*	63.7	3,05E-6	3,05E-6	3,05E-6	3,04E-6	3,02E-6	2,85E-6	2,25E-6	1,23E-6	1,33E-6	1,32E-6	1,32E-6	1,32E-6
fs		6,71E+5	6,71E+5	6,71E+5	6,74E+5	6,79E+5	7,19E+5	9,11E+5	1,66E+6	1,54E+6	1,55E+6	1,55E+6	1,55E+6
T_2*	147	3,05E-6	3,05E-6	3,04E-6	3,02E-6	2,85E-6	2,25E-6	1,23E-6	1,33E-6	1,32E-6	1,32E-6	1,32E-6	1,32E-6
fs		6,71E+5	6,71E+5	6,74E+5	6,79E+5	7,19E+5	9,11E+5	1,66E+6	1,54E+6	1,55E+6	1,55E+6	1,55E+6	1,55E+6
T_2*	340	3,05E-6	3,04E-6	3,02E-6	2,85E-6	2,25E-6	1,23E-6	1,33E-6	1,32E-6	1,32E-6	1,32E-6	1,32E-6	1,32E-6
fs		6,71E+5	6,74E+5	6,79E+5	7,19E+5	9,11E+5	1,66E+6	1,54E+6	1,55E+6	1,55E+6	1,55E+6	1,55E+6	1,55E+6
T_2*	785	3,04E-6	3,02E-6	2,85E-6	2,25E-6	1,23E-6	1,33E-6	1,32E-6	1,32E-6	1,32E-6	1,32E-6	1,32E-6	1,32E-6
fs		6,74E+5	6,79E+5	7,19E+5	9,11E+5	1,66E+6	1,54E+6	1,55E+6	1,55E+6	1,55E+6	1,55E+6	1,55E+6	1,55E+6
T_2*	$1.81 \cdot 10^3$	3,02E-6	2,85E-6	2,25E-6	1,23E-6	1,33E-6	1,32E-6	1,32E-6	1,32E-6	1,32E-6	1,32E-6	1,32E-6	1,32E-6
fs		6,79E+5	7,19E+5	9,11E+5	1,66E+6	1,54E+6	1,55E+6	1,55E+6	1,55E+6	1,55E+6	1,55E+6	1,55E+6	1,55E+6
T_2*	$4.19 \cdot 10^3$	2,85E-6	2,25E-6	1,23E-6	1,33E-6	1,32E-6	1,32E-6	1,32E-6	1,32E-6	1,32E-6	1,32E-6	1,32E-6	1,31E-6
fs		7,19E+5	9,11E+5	1,66E+6	1,54E+6	1,55E+6	1,55E+6	1,55E+6	1,55E+6	1,55E+6	1,55E+6	1,55E+6	1,56E+6
T_2*	$9.68 \cdot 10^3$	2,25E-6	1,23E-6	1,33E-6	1,32E-6	1,32E-6	1,32E-6	1,32E-6	1,32E-6	1,32E-6	1,32E-6	1,31E-6	1,31E-6
fs		9,11E+5	1,66E+6	1,54E+6	1,55E+6	1,55E+6	1,55E+6	1,55E+6	1,55E+6	1,55E+6	1,55E+6	1,56E+6	1,56E+6
T_2*	$22.3 \cdot 10^3$	1,23E-6	1,33E-6	1,32E-6	1,32E-6	1,32E-6	1,32E-6	1,32E-6	1,32E-6	1,32E-6	1,31E-6	1,31E-6	1,23E-6
fs		1,66E+6	1,54E+6	1,55E+6	1,55E+6	1,55E+6	1,55E+6	1,55E+6	1,55E+6	1,55E+6	1,56E+6	1,56E+6	1,66E+6
T_2*	$51.6 \cdot 10^3$	1,33E-6	1,32E-6	1,32E-6	1,32E-6	1,32E-6	1,32E-6	1,32E-6	1,32E-6	1,31E-6	1,31E-6	1,23E-6	9,71E-7
fs		1,54E+6	1,55E+6	1,55E+6	1,55E+6	1,55E+6	1,55E+6	1,55E+6	1,55E+6	1,56E+6	1,56E+6	1,66E+6	2,11E+6

CHAPTER 4

RESULTS OF FFT BASED IMAGE RECONSTRUCTION ALGORITHM FOR INHOMOGENOUS MAGNETIC FIELDS

Theory behind the developed FFT based image reconstruction algorithm for inhomogeneous magnetic fields is given in Chapter 2. The developed reconstruction algorithm needs main magnetic field distribution, RF magnetic field distribution, Gradient field distribution, pulse sequence, RF coil parameters, MRI system parameters and FID signals. These inputs except the FID signals are known.

To obtain a realistic FID signal for inhomogeneous case, a simulator is developed. The implemented simulator is based on derived Bloch equation and noise model given in Chapter 2. For specific inputs, direct solution of the derived Bloch equation can be found, instead of solving it numerically. This improves computational efficiency. Block diagram of the MRI simulator for inhomogeneous magnetic field is given in Figure 4.1. Furthermore, image reconstruction modules are given in this figure.
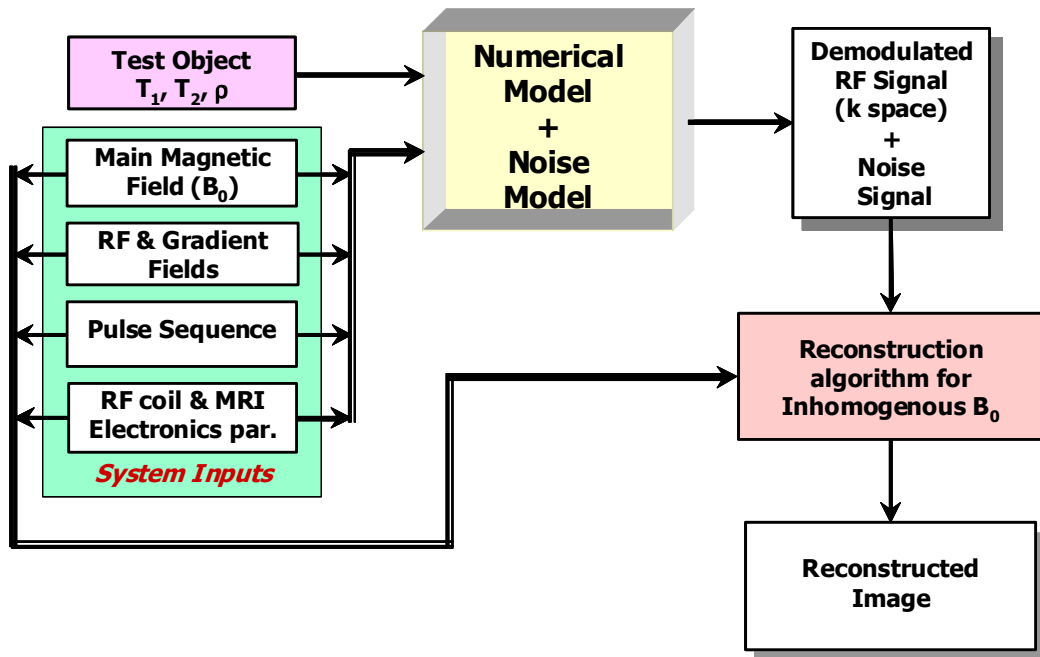
Figure 4.1. Block diagram of the MRI simulator for inhomogeneous magnetic field, which includes numerical model, noise model and image reconstruction modules.

For some inputs, analytical solution of the derived Bloch equation can be found. The cases where the equation has analytical solution is listed in Table 4.1. The numerical solution covers all possibilities but it is computationally intensive, and the additional numerical error introduced [73].

Table 4.1. Investigating usage of analytical solution.

	Analytical
Static magnetic field applied	✓
Circularly polarized RF signal at resonance frequency	✓
Random RF signal	✗
Slow varying gradient fields	✓
Fast varying gradient fields	✗
Time varying T_1, T_2, and ρ	✓

4.1. FFT Based Image Reconstruction Algorithm Results without Noise

To test the validity of the proposed FFT Based Image Reconstruction Algorithm, two-dimensional experiments at uniform magnetic fields are investigated. This analysis is performed since the results are expected to be the same as conventional MRI.

In order to do that assume uniform main magnetic field, which is equal to

$$\vec{B}_0(x, y, z) = 0.1\hat{a}_z \tag{4.1}$$

Then RF coil's magnetic field can be defined as:

$$\vec{B}_1(x, y, z) = 1 \cdot 10^{-4} \hat{a}_x \tag{4.2}$$

The gradient fields are selected as in conventional MRI systems. In these systems, gradient fields' directions are the same with the direction of main magnetic field and linearly varying with respect to position according to which gradient it is. As an example for x gradient,

$$\vec{G}_x(x, y, z) = 10^{-2} x\hat{a}_z \tag{4.3}$$

A spin echo pulse sequence as shown in Figure 4.2 is assigned, as a pulse sequence. In the pulse sequence, the RF signal magnitude is selected such that the spins are rotated 90 and 180 degrees. The strength of gradients are selected, such that FOV is same as the test object. The repetition time (T_R) and echo time (T_E) are selected as to get proton density images. T_R and T_E are equal to 5 s and 5 ms respectively.
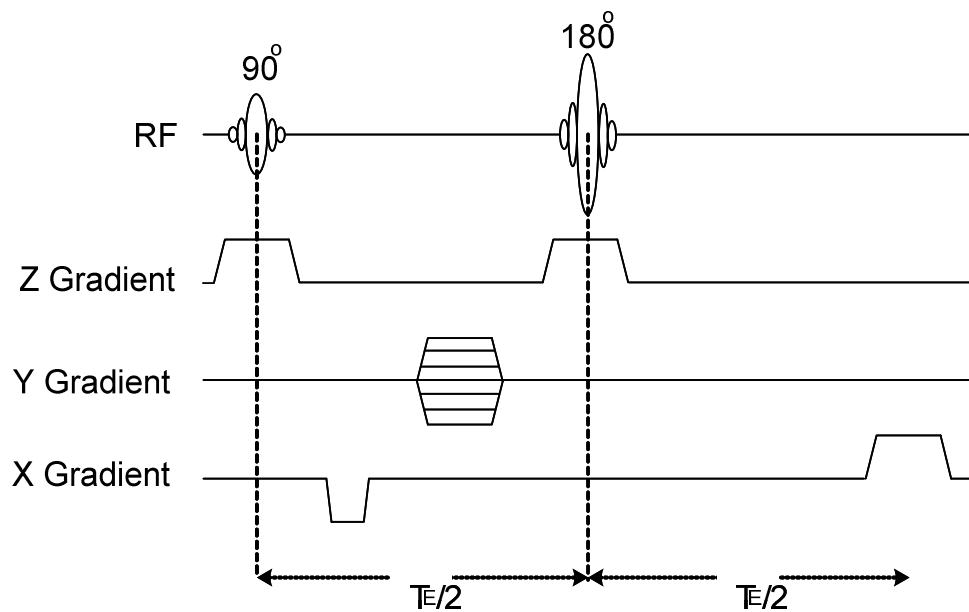

Figure 4.2. Spin echo pulse sequence.

As a test object, two-dimensional Shepp-Logan head phantom geometry with MR parameters is used. The proton density image of the test object relative to water is shown in Figure 4.3. The relaxation times for the test object (T_1, T_2) selected as uniform. T_1, T_2 selected as 1 s and 500 ms.
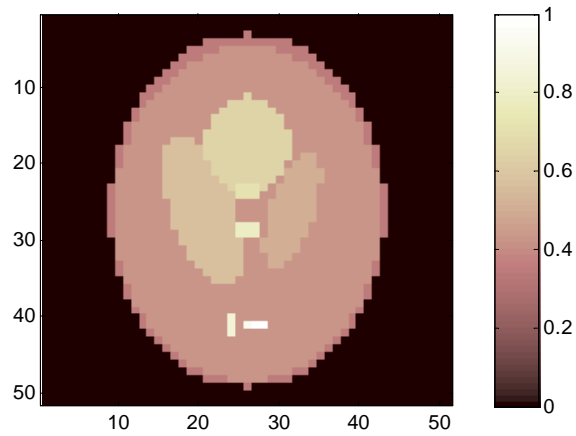
Figure 4.3. Proton density distribution of the test object.

The simulation studies are made using the above input parameters. Hence, the results of the numerical model without noise are obtained. Calculation of FID signals to fill the k-space takes about 120 minutes with a PC (Pentium 4 2.8GHz CPU & 2GB RAM). The output of the numerical model is given in Figure 4.4.


(a)

(b)
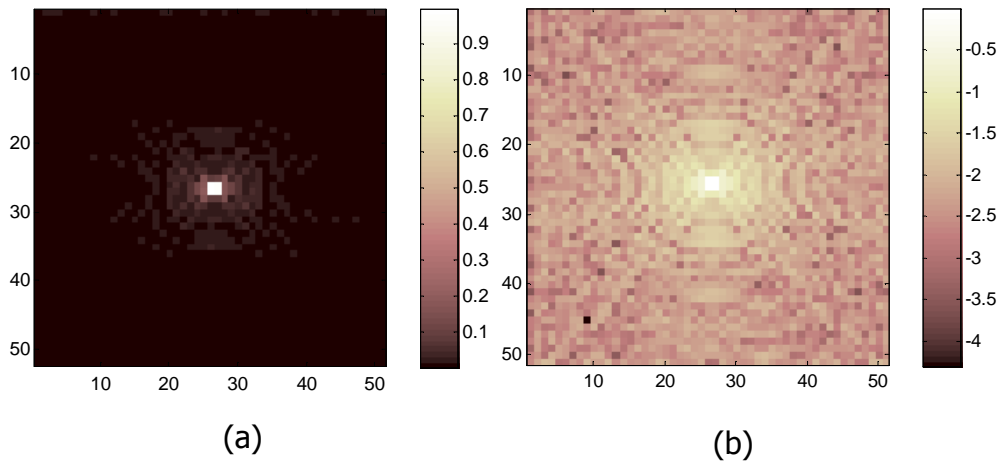
Figure 4.4. Simulation results (a) linear scale (b) logarithmic scale.

Since this is the simulation of well-known conventional MRI, the output signal corresponds to two-dimensional Fourier transform of the proton density image. So that, the image can be reconstructed by taking two-dimensional Inverse Fourier Transform. However, in the proposed reconstruction algorithm the results are multiplied by inverse of "*A*" matrix, which is defined in (2.70). The magnitude of *A* matrix is shown in Figure 4.4. As seen from Figure 4.5, matrix *A* is nearly an identity matrix. Elements other than the diagonal, are in the order of 10^{-12}. The matrix rank is full and eigen values of the magnitude of *A* matrix are equal to each other. Hence, its inverse is identity matrix.
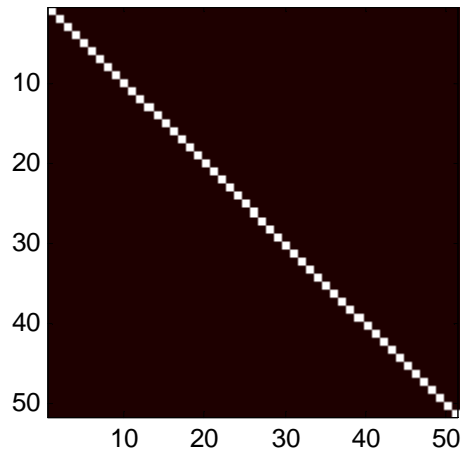
Figure 4.5. The magnitude of *A* matrix is given for homogenous magnetic main field with linear gradient and spin echo pulse sequence.

Figure 4.6 shows the reconstructed image. Relative error in the reconstructed image can be found using Equation (4.3) where proton density is nonzero. In the equation ρ is proton density of test object, ρ_R is reconstructed proton density l is pixel number, L_1 is number of pixel, where proton density is non zero.

78
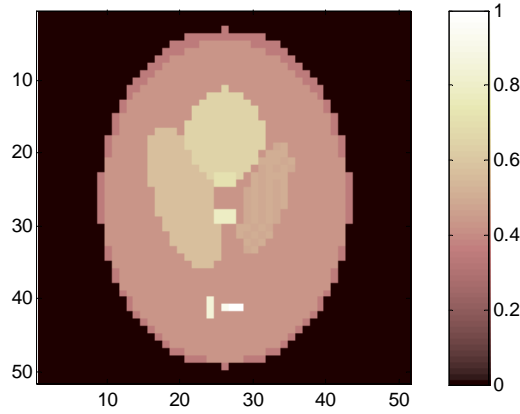
Figure 4.6. Reconstructed image is given for homogenous main magnetic field with linear gradient and spin echo pulse sequence.

$$\text{Relative Error \%} = \sqrt{\frac{1}{L_1} \sum_{l=1}^{L_1} \frac{(\rho_l - \rho_{R,l})^2}{\rho_l^2}} \times 100\% \quad \text{where } \rho > 0 \tag{4.3}$$

An error measure, where the test object's proton density is zero, has to be defined. As an error measure mean of values where the test object's proton density is zero. The formula is given in (4.4). In this equation L_2 is number of pixel, where proton density is zero.

$$\text{Background noise} = \frac{1}{L_2} \sum_{l=1}^{L_2} |\rho_{R,l}| \quad \text{where } \rho = 0 \tag{4.4}$$

As seen from Figure 4.6, the image is reconstructed almost perfectly. The errors are due to the numerical truncation error and numerical derivatives used while calculating the induced voltage. The relative error is $3.02 \cdot 10^{-3}\%$, and background

noise described in (4.4) is $4.21 \cdot 10^{-5}$. After that, some parameters are changed and results are obtained for these cases. The changed parameters and calculated errors are given in Table 4.2.

Table 4.2. Error values for different inputs for homogenous main magnetic field with linear gradient and spin echo pulse sequence

	Relative error %	Background Noise
Reference	$3.02 \cdot 10^{-3}$	$4.21 \cdot 10^{-5}$
Proton density distribution doubled	$3.02 \cdot 10^{-3}$	$4.20 \cdot 10^{-5}$
T_1 value of test object doubled	$3.82 \cdot 10^{-3}$	$4.33 \cdot 10^{-5}$
T_2 value of test object doubled	$3.77 \cdot 10^{-3}$	$1.13 \cdot 10^{-4}$
T_E value doubled	$3.03 \cdot 10^{-3}$	$8.41 \cdot 10^{-5}$
T_R value doubled	$2.81 \cdot 10^{-3}$	$3.71 \cdot 10^{-5}$

As seen from the table, the error values are small. This shows that the simulation works fine for uniform inputs and reconstruction algorithm give correct results. To understand the necessity of the proposed algorithm, the results for non-uniform magnetic field case, has to be analyzed. In order to investigate the non-uniform case, non-uniform main and magnetic field have to be used. For inhomogeneous main magnetic field, outside of a 0.15 T Oxford magnet is measured and used as the main magnetic field. By doing this, a more realistic simulation is made. The measured magnetic field with a maximum inhomogeneity of 1.95×10^5 ppm is shown in Figure 4.7. As seen in the figure, there is no x-component in the main magnetic field. The RF coil's magnetic field is assumed to be uniform and in x-direction. By this assumption, RF magnetic field is perpendicular to the main magnetic field. A spin echo pulse sequence is used as the pulse sequence.
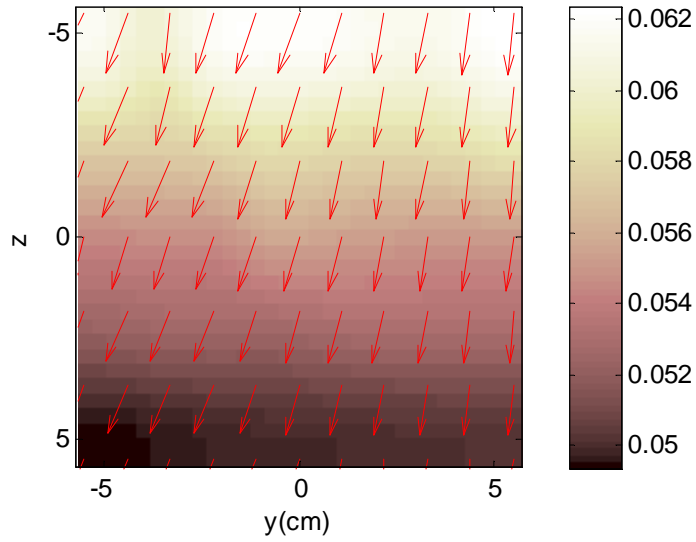
Figure 4.7. Strength and direction of the main magnetic field. Color map shows the strength of main magnetic field, the arrows show the direction of the main magnetic field. The x-component of the main magnetic field is zero.

The parameters used for the simulation are given in Table 4.3. The gradient fields are selected such that they are parallel to the main magnetic field & varying linearly with position accordingly with a constant of 10^{-3} T/m. The input proton density is the same as the previous.

Table 4.3. Simulation inputs for inhomogeneous main magnetic field case.

Parameter	Value
Longitudinal Relaxation for phantom (T_1)	2 s
Transverse Relaxation (T_2)	0.5 s
Echo time (T_E)	5 ms
Repetition time (T_R)	5 s
Data Acquisition Time (T_S)	0.5 ms
Number of averages (N)	4
Slice thickness	1 cm
Number of pixels	31x31

The simulation is performed for described inputs then the resultant signals are found.
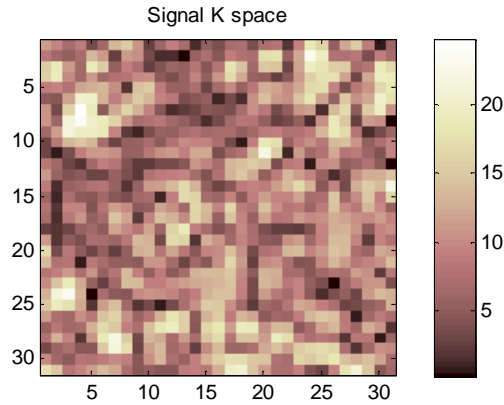

Figure 4.8. Absolute value of demodulated FID signals without noise is given.

Two-dimensional Fourier transform of the demodulated FID signal is shown in Figure 4.9. For the image in Figure 4.8 the relative error, is 95% and the mean of background noise is 0.15. Following the Fourier transformation, the *A* matrix is calculated. For this case, A matrix is not full rank so that for matrix inversion singular value decomposition (SVD) technique is used. To achieve better results, truncation can be applied in SVD method. The truncation level can be selected according to the relative error, since the original phantom is known. Error versus truncation level is shown in Figure 4.10. The truncation level selected as 843rd singular value. The value for this is about 0.9% of the largest singular value. Then, for this truncation level the image reconstructed using proposed FFT based reconstruction algorithm. The reconstructed image is shown in Figure 4.11. The reconstructed image has 8.3% relative error with 0.03 background noise mean.

Direct FFT reconstructed image
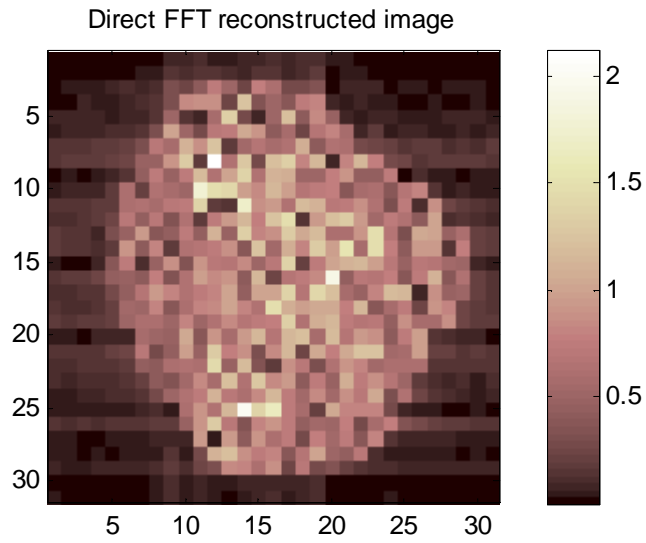
Figure 4.9. Direct Fourier transform of the demodulated output signal.

Relative Error

Background Error Mean

(a)

(b)
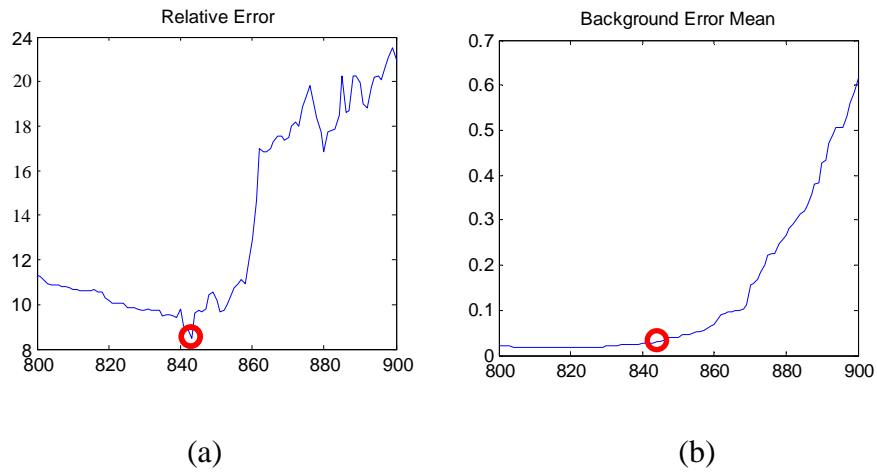
Figure 4.10. a) Relative error, b) Background noise mean versus SD truncation level for noiseless inhomogeneous case.
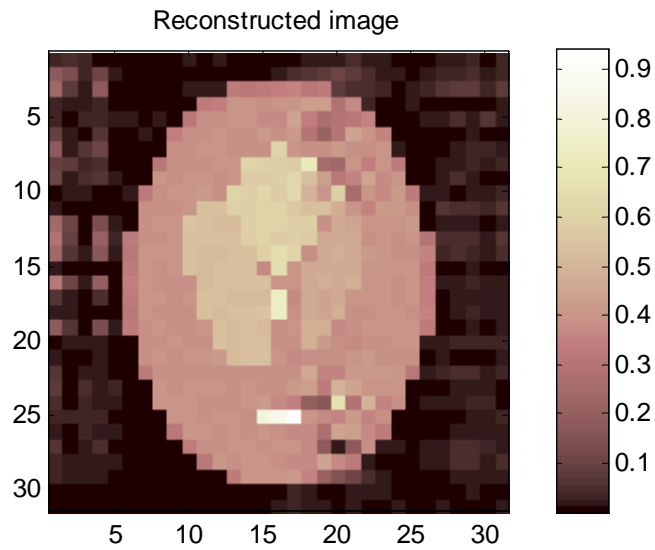
Figure 4.11. Reconstructed image using proposed FFT based reconstruction algorithm.

4.2. FFT Based Image Reconstruction Algorithm Results with Noisy Free Induction Decay Signal

Pixel SNR can be found for each pixel by the method explained in theory part. To find it the main and RF magnetic field information, test object properties and pulse sequence have to be known. Signal strength for every pixel can also be determined by the given information. Using *pixel SNR* and signal strength, noise level can be determined for every pixel and then Gaussian noise with zero mean is added to the signal. Rest of the FID signal calculation and image reconstruction is the same as the noiseless case. Again, Shepp-Logan head phantom geometry with MR properties given in figure 4.6 and table 4.4. is used as a test object. Properties of the other parameters are given in Table 4.4.

Table 4.4. Pulse sequence, test object and other parameters used as inputs simulation for inhomogeneous main magnetic field case.

Parameter	Value
T_E time	5 ms
T_R time	5 s
T_S time	0.07 ms
Number of averages (N)	2
T_1 relaxation	1 s
Number of pixels	31x31
Object size	11.5x11.5 cm
Slice Thickness (ST)	1 cm
Noise Figure (NF)	1.5 dB
Q_L quality	170
Q_E quality	240

FID signal decays primarily with T_2, and this decay becomes more rapid under inhomogeneous magnetic fields. In order to evaluate the effect of T_2 in MR imaging using inhomogeneous magnetic fields and realistic FID signals for various T_2 values (i.e. 300, 100, 50, 20 and 10 ms) are generated using the developed model. Based on these FID signals, MRI images are reconstructed by using the developed FFT based reconstruction algorithm for MRI in inhomogeneous fields. Reconstructed images are given in figure 4.12.
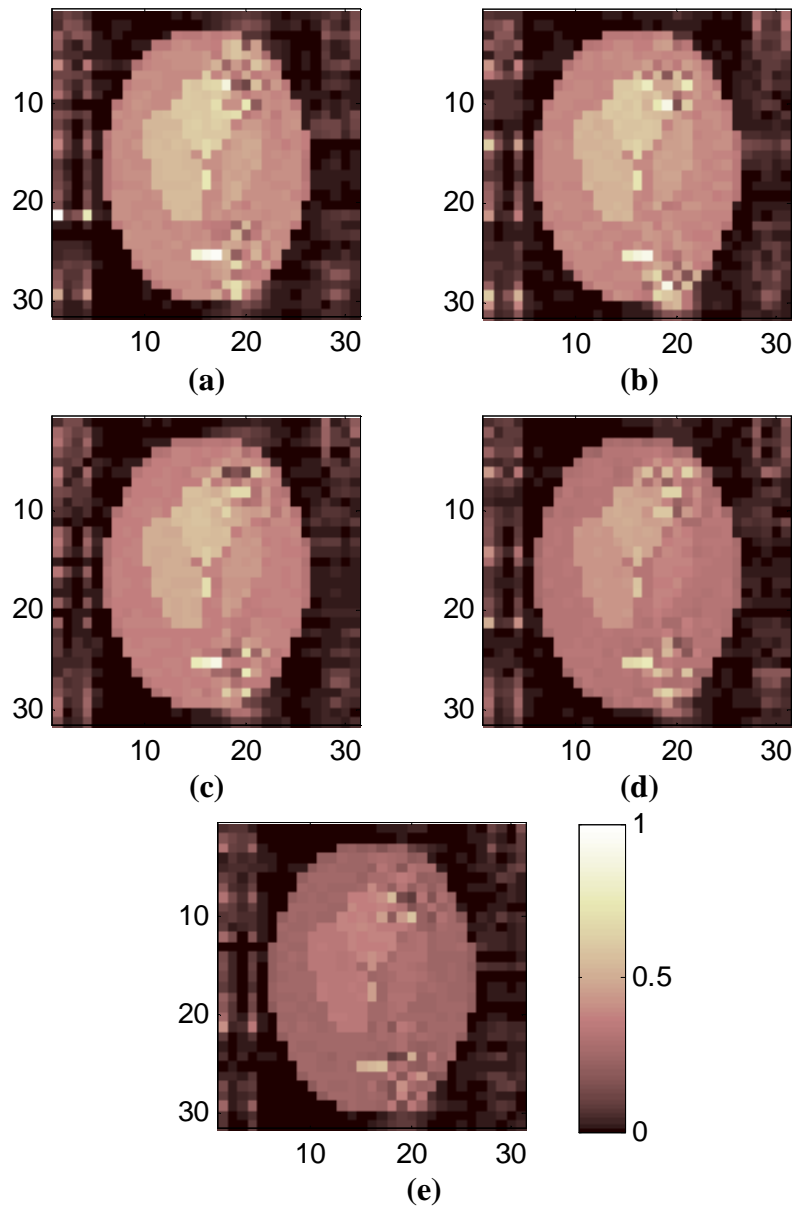
Figure 4.12. Reconstructed images with different T_2 values. (a) $T_2 = 300$ ms, (b) $T_2 = 100$ ms, (c) $T_2 = 50$ ms, (d) $T_2 = 20$ ms, (e) $T_2 = 10$ ms

The reconstructed image contrast decreases with T_2, since T_2 becomes comparable with TE and the resultant image is not a spin density weighted image anymore. Noise becomes more dominant in the reconstructed images with

decreasing T_2, causing larger reconstruction errors (Table 4.5). Images with tolerable error are obtained with T_2 values comparable to those of biological tissues when the proposed reconstruction algorithm is used.

Noise performance of the proposed reconstruction algorithm is also evaluated for $T_2 = 100$ *ms* (typical for head tissue). *N* and *Slice Thickness* changed to obtain different SNR levels (table 3). Increasing slice thickness as well as averaging improves SNR hence the reconstruction error decreases.

Table 4.5. SNR values and reconstruction errors for different T_2 values.

T_2	SNR	Reconstruction Error
300 *ms*	52.7	13.6 %
100 *ms*	51.1	14.5 %
50 *ms*	48.2	16.7 %
20 *ms*	42.0	25.2 %
10 *ms*	32.4	41.4 %

Table 4.6. SNR values and reconstruction error corresponding to different input parameters (*N* and *ST*).

N	ST	SNR	Reconstruction Error
-	-	∞	8.5 %
4	1 *cm*	72.4	11.4 %
2	1 *cm*	51.1	14.5 %
1	1 *cm*	35.8	15.9 %
1	0.5 *cm*	18.6	22.7 %

CHAPTER 5

EXPERIMENTAL RESULTS

To obtain experimental results for magnetic resonance imaging in inhomogenous main magnetic field, a phantom filled with a material containing MR active nuclei is needed.

5.1. Experimental Setup

The chosen phantom has a simple shape, which is given in Figure 5.1.
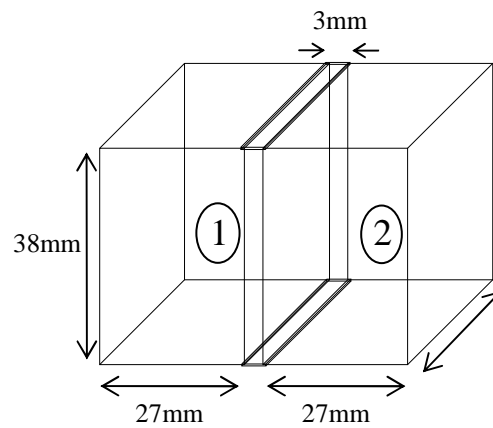
Figure 5.1. Experimental phantom with two separate compartments (1 & 2) is used for magnetic resonance imaging in inhomogenous main magnetic field.

In experiments phantom compartments filled 1g of $CuSO_4$ in 1lt pure water at 25°C.

In order to estimate T_1 and T_2 relaxation time constants compartment 1 of the phantom is completely filled with $CuSO_4$ solution. A spin echo pulse sequence without a slice selection and phase encoding gradient is applied. Adopted pulse sequence is shown in Figure 5.2. For this pulse sequence Echo time (T_E) is fixed to 17 ms and T_R values changed in the range of [70 ms, 5 s] and FID signal is collected 16 times and averaged to find less noisy data. Then maximum of averaged FID signal found for the corresponding T_R time.
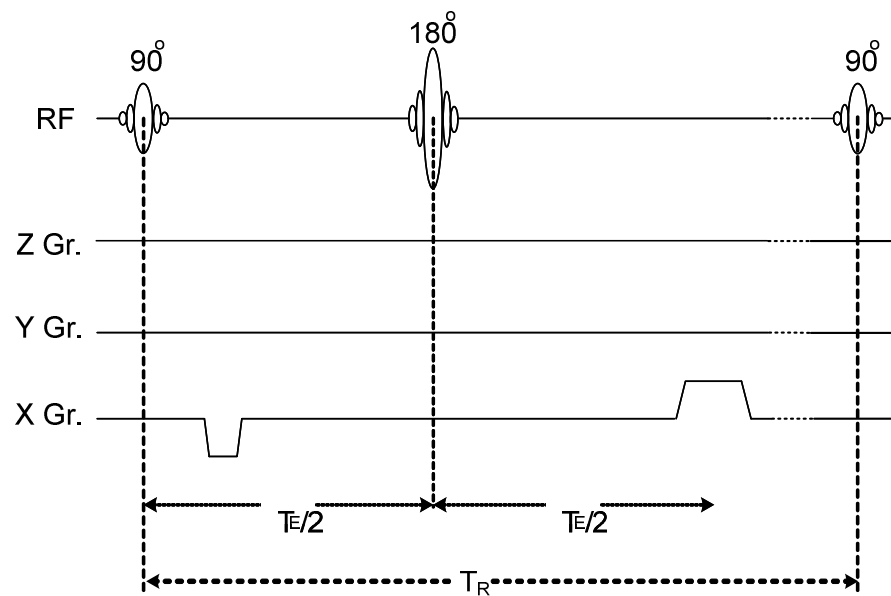

Figure 5.2. Pulse sequence used to find the T_1 and T_2 estimate of the $CuSO_4$ solution.

Using these points FID signal maximum versus TR plot is obtained and shown in figure 5.3. In addition, the Bloch equation that relates signal maximum of the FID signal the relation is given in (5.1) [4] as

$$\max\{\text{FID(t)}\} = A_1\left(1 - \exp(-T_R/T_1)\right) \tag{5.1}$$

Using relation (5.1) a curve can be fitted to the experimental data. For curve fitting Nonlinear Least Squares method and Trust-Region algorithm is used. A_1 estimate is equal to 5.33 with 95% percent confidence bound (5.27, 5.40) and T_1 estimate is equal to 0.160 with 95% percent confidence bound (0.156, 0.164). For these A_1 and T_1 values obtained curve is given in Figure 5.3.
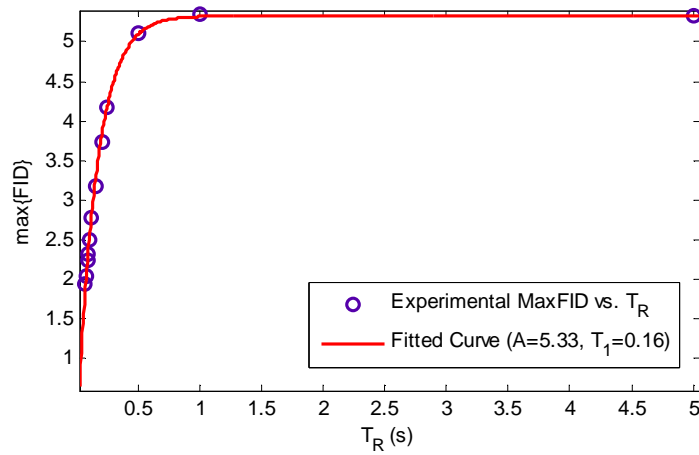

Figure 5.3. Experimental results of FID signal maximum versus different T_R values are shown as blue circles and fitted curve ($A_1 = 5.33$, $T_1 = 0.16$) for these experimental data are shown in red line.

For T_2 estimation, the same phantom and pulse sequence are used but T_R is fixed to 1 s and T_E is varied in the range of [17 ms, 307 ms]. FID signal is collected 16 times and averaged. The relation between FID signal maximum and TE is given in (5.2).

$$\max\{\text{FID(t)}\} = A_2 \left(\exp(-T_E / T_2) \right) \qquad (5.2)$$

Using the same technique for T_1 estimation a curve fitted for the experimental results. The fitted curve and experimental results are given in Figure 5.4. A_2 estimate is equal to 5.41 with 95% percent confidence bound (5.26, 5.56) and T_2 estimate is equal to 0.152 with 95% percent confidence bound (0.142, 0.161). Corresponding curve for these A_2 and T_2 values is given in Figure 5.4.
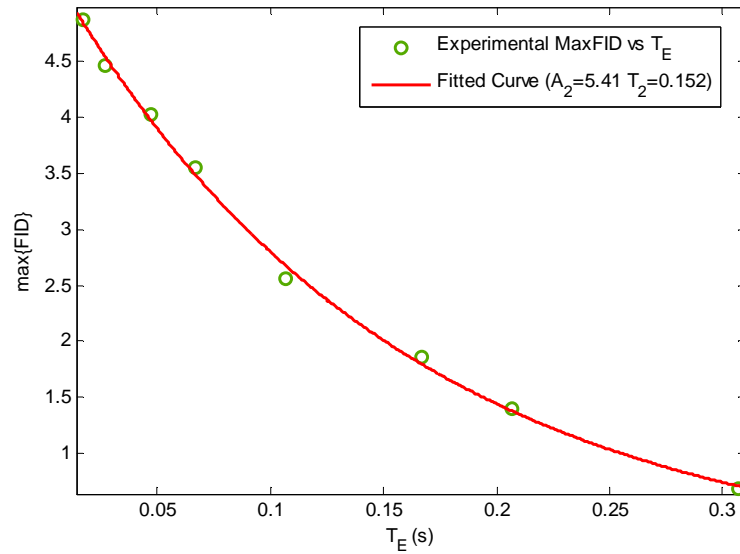
Figure 5.4. Experimental results of FID signal maximum versus different T_R values are shown as green circles and fitted curve ($A_2 = 5.41$, $T_2 = 0.152$) for these experimental data are shown in red line.

5.2. Experimental Results for FID Signal in Inhomogeneous Main Magnetic Field for One-Dimension

To make one-dimensional analysis of FID signal in inhomogeneous main magnetic field for one-dimension, conventional 0.15T METU-MRI system with a special pulse sequence is used. As a test object, the phantom described above with compartment 1 filled with $CuSO_4$ solution is used. Object's, T_2 and T_1 value are found to be 152 ms and 160 ms, respectively. Using pulse sequence shown in Figure 5.5, main magnetic field strength in z direction varies linearly in x direction. In addition, single RF coil is used for excitation and reception. The magnetic field of RF coil is in the direction of x and assumed to be uniform.
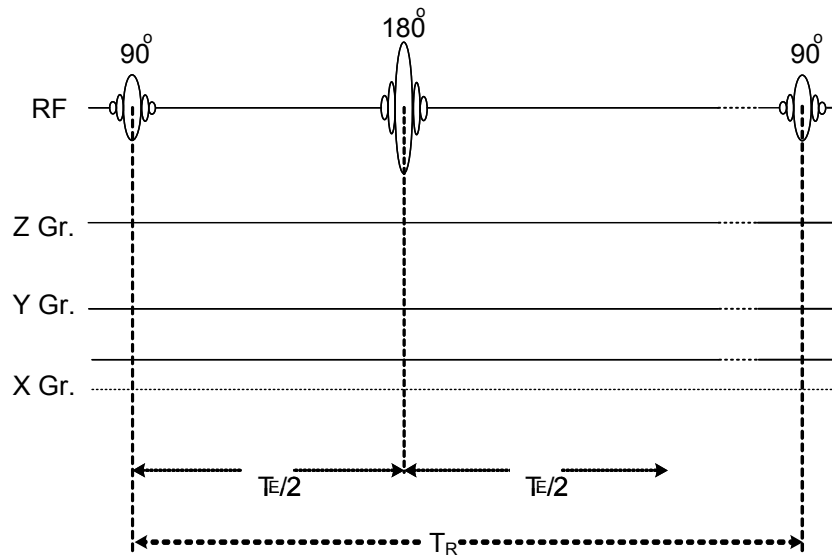
Figure 5.5. Pulse sequence used to find the Experimental Results for Free Induction Decay Signal in Inhomogeneous Main Magnetic Field for one-dimensional case.

To generate linear variation on the main magnetic field x-gradient is used, so the main magnetic field is varied linearly in the FOV. Varying the strength of x-gradient, different level of inhomogeneity in the FOV is obtained. Amplitude of FID results are shown in Figure 5.6.
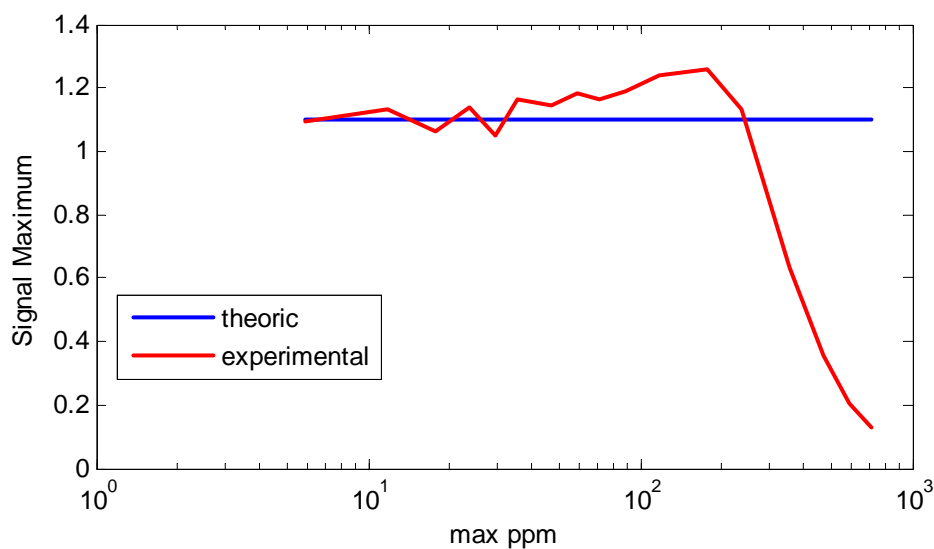
Figure 5.6. Inhomogeneity level versus demodulated FID signals' maximum values plot is given for one-dimensional case. Blue line is calculated from analytical FID signals. Red line shows experimental results.

In Figure 5.6. analytic results are obtained assuming ideal 90º RF pulse is used. Therefore, the signal maximum for analytical case does not change. However, for experimental results, RF pulse gain is set manually and this affects the signal peak. by changing the RF gain about 90º RF pulse can be obtained below the $1.5 \cdot 10^2$ ppm inhomogeneity level, As the inhomogeneity in the FOV increases, RF pulse bandwidth has to increase. In order to increase the bandwidth, the pulse duration decreases, due to RF gain limitation the pulse degree decreases. In addition, the results are affected due to frequency characteristics of the RF coil and electronics part.
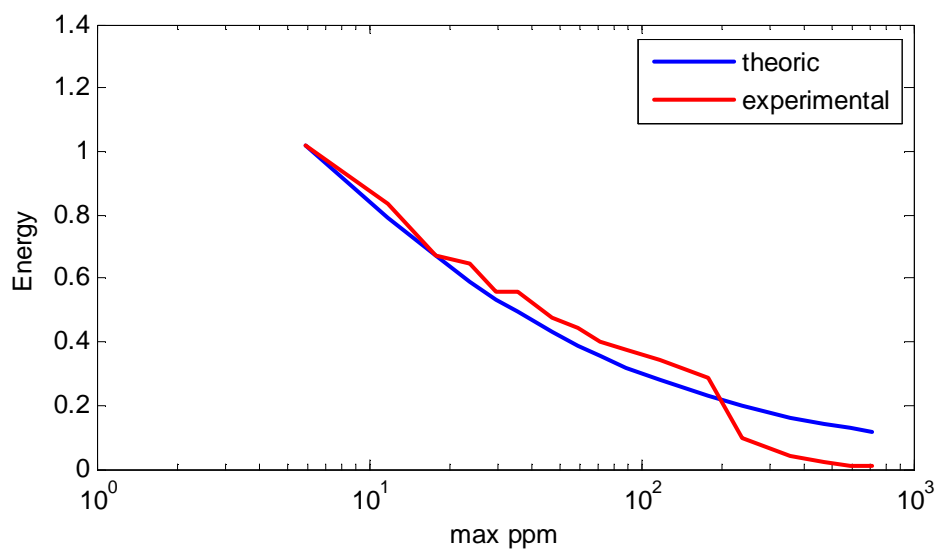
Figure 5.7. Inhomogeneity level versus demodulated FID signals' normalized energy plot is given for one-dimensional case. Blue line is calculated from analytical FID signal. Red line gives experimental results.

For the energy plot up to $1.5 \cdot 10^2$ ppm inhomogeneity level, experimental and analytical results are similar. Due to RF pulse gain limitation, amplitude of the signal so the energy decreases.
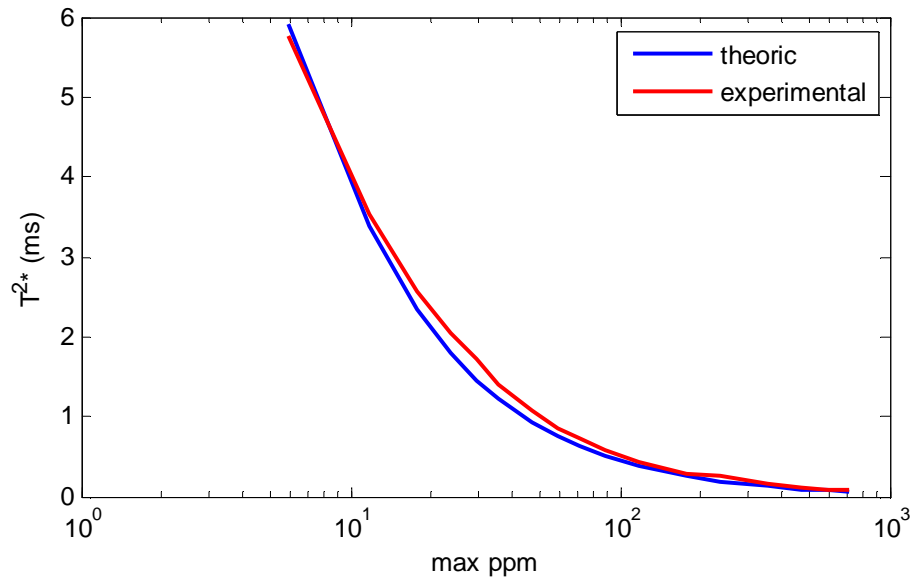
(a)
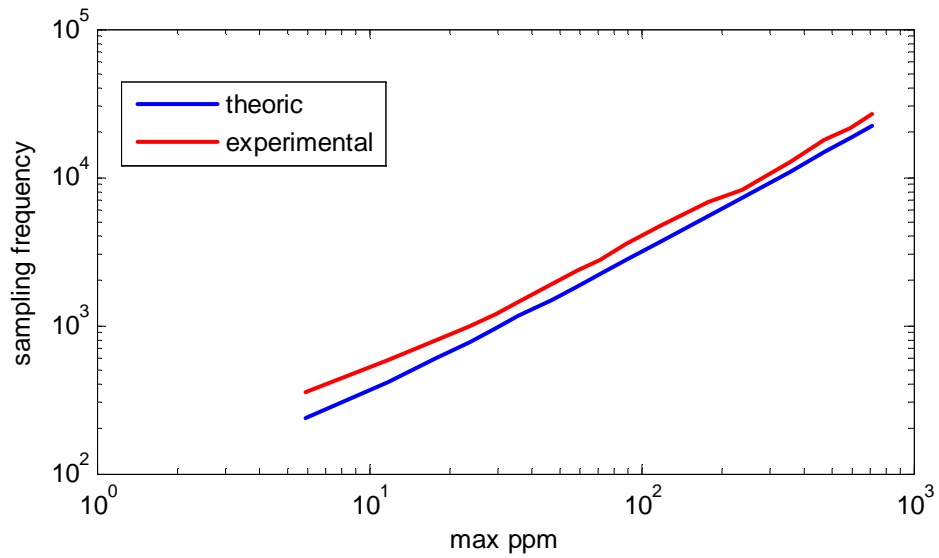
(b)

Figure 5.8. Inhomogeneity level versus (a) T_2^* estimate and (b) minimum sampling frequency needed is given for one-dimensional case. Assumptions are MRI receiver part has a 12 bit analog to digital converter and 31 pixel image is reconstructed. Blue lines are calculated using analytical FID signal. Red lines are obtained from experimental results.
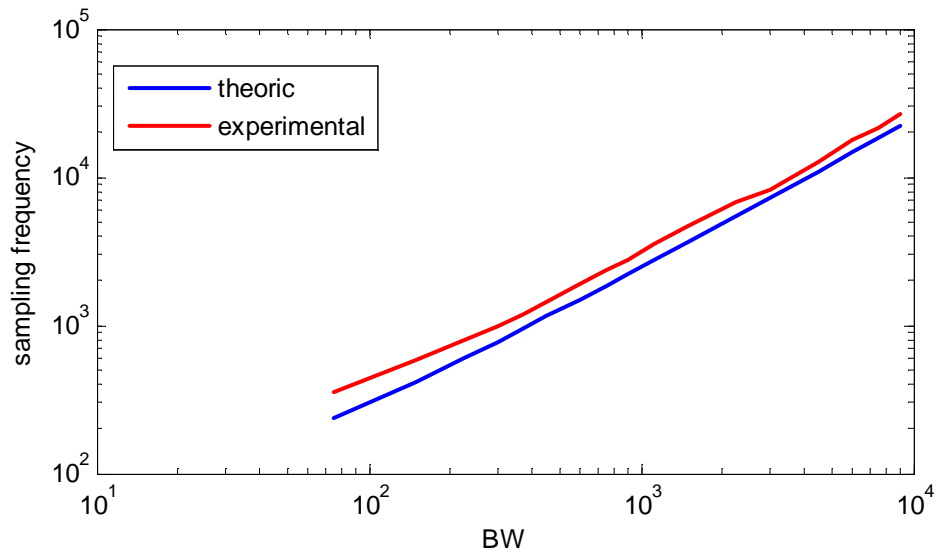
Figure 5.9. Bandwidth level versus minimum sampling frequency needed is given for one-dimensional case. Assumptions are MRI receiver part has a 12 bit analog to digital converter and 31 pixel image is reconstructed. Blue lines are calculated using analytical FID signal. Red lines are obtained from experimental results.

As seen from the results in Figure 5.8 the T_2^* values and the sampling frequency does not depend on amplitude variation. This is compensated while calculating T_2^* estimates which is given in subsection 3.1.1. The difference between analytical and experimental results may due to the gradient field strength variation and gradient amplifier gain.

5.3. Experimental Results for Imaging in Inhomogeneous Main Magnetic Field for One-Dimension

To make obtain one-dimensional image for inhomogeneous main magnetic field again conventional 0.15T METU-MRI system with previous pulse sequence given in Figure 5.5 is used. Same test object and RF coil is used. The inhomogeneity level is set to $1.5 \cdot 10^2$ ppm which is the maximum limit applicable to a 90º RF pulse. Since the variation in the main magnetic field is linear in x-direction the reconstruction matrix found to be identity and the obtained result is shown in Figure 5.10. The reconstruction error is 14.3%.
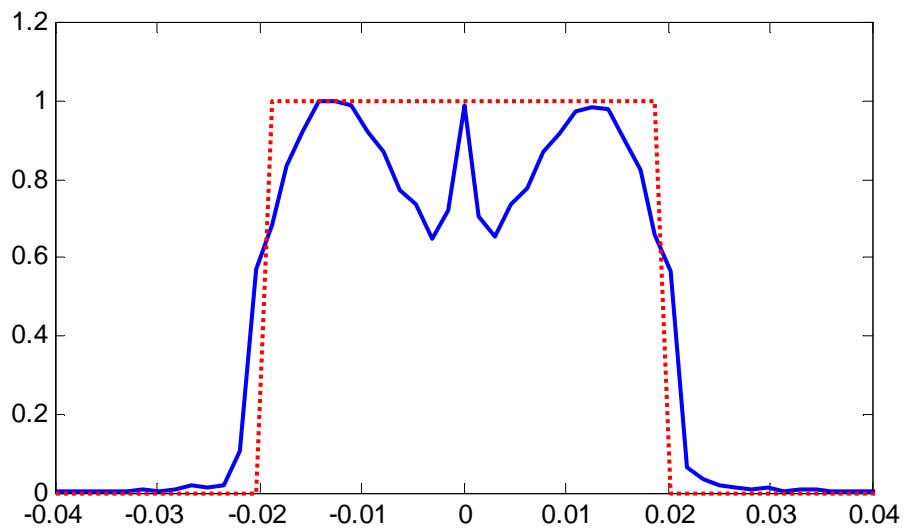

Figure 5.10. Experimental result of imaging in inhomogeneous main magnetic field for one-dimensional case. Blue line is reconstructed image. Red line shows the phantom.

CHAPTER 6

CONCLUSIONS

In this thesis, analysis of magnetic resonance imaging in inhomogeneous main magnetic filed is aimed. To do this analysis, MR systems that use inhomogeneous magnetic fields and FID signal models used for these systems are surveyed.

A new model is developed to calculate FID signal for inhomogeneous magnetic fields. The model consists of two main parts, which are magnetization vector calculation part and signal formation part. The first part is similar to Bloch equation, but it is position dependent to cover inhomogenous case. So that, using this part, magnetization vectors are found for every time instant and voxel. Then utilizing these magnetization vectors and developed model's signal reception part, FID signals are calculated.

Furthermore, a new noise model is implemented to achieve realistic FID signal. To calculate realistic noisy FID signal, noise model for MRI with homogeneous fields is extended for inhomogeneous fields. Then FID signal and noise models are used synchronously to calculate MR and additive noise signals.

Using these models' outputs and derived analytical results, FID is characterized in inhomogeneous main fields. The characterization is done for different levels of inhomogeneity for one and two-dimensional cases. The characterization includes the relation between inhomogeneity level and signal decay, signal peak,

signal energy, FOV, and MRI system parameters (RF bandwidth, receiver bandwidth, resolution, and maximum sampling rate). Using these relations and obtained results, required system parameters can be calculated from inhomogeneity level. Similarly, inhomogeneity level limit can be calculated from system parameters.

A new image reconstruction algorithm is proposed for inhomogeneous magnetic fields. Proposed algorithm is FFT based. The algorithm is tested using a test object in homogeneous magnetic field. The obtained results are almost same to original object proton density distribution (relative error $< 3.77 \cdot 10^{-3}$ %). After that, the algorithm is tested with inhomogeneous main magnetic field. The proposed reconstruction algorithm gives 8.5 % relative error. When only two-dimensional Fourier transform is employed, the reconstructed image has 95 % relative error. Image reconstruction algorithm is also tested for different levels of noise and relaxation times to understand the influence of both variables. In the worst case relative error of 42 % is achieved. This result is twice as better as compared to direct FFT reconstruction.

REFERENCES

[1]   F. Bloch, 1946, "Nuclear Induction," Physical Review, 70, pp. 460-474.

[2]   E. M. Purcell, H. C. Torrey, and R. V. Pound, 1946, "Resonance Absorption by Nuclear Magnetic Moments in a Solid," Physical Review, 69, pp. 37 – 38.

[3]   E. M. Haacke, R. W. Brown, M. R. Thomson, R. Venkatesan, 1999, "Magnetic Resonance Imaging Physical Principles and Sequence Design," Wilew-Liss.

[4]   Z. P. Liang, P. C. Laterbour, 2000, "Principles of magnetic Resonance Imaging," IEEE Press.

[5]   P. C. Lauterbur, 1973, "Image formation by induced local interactions: examples employing nuclear magnetic resonance," Nature, 242, pp. 190-191.

[6]   R. L. Kleinberg, A. Sezginer, D. D. Griffin, and M. Fukuhara, 1992, "Novel NMR apparatus for investigating an external sample," Journal of Magnetic Resonance, 97, pp. 466.

[7]   G. R. Coates, L. Xiao, M. G. Prammer, 1999, "NMR Logging Principles and Applications," Halliburton Energy Services, USA.

[8]   R. L. Kleinberg, 1996, "Well logging," Encyclopedia of NMR, Wiley-Liss, New York, pp. 4960-4969.

[9]   E. L. Hahn, 1950, "Spin Echoes," Phys. Rev., 80, pp. 580-594.

[10] H. Y. Carr, E. M. Purcell, 1954, "Effects of Diffusion on Free Precession in Nuclear Magnetic Resonance Experiments," Phys. Rev., 94, pp. 630-638.

[11] S. Meiboom, D. Gill, 1958, "Modified Spin-Echo Method for Measuring Nuclear Relaxation Times," Rev. Sci. Instrum., 29, pp. 688-691.

[12] E. L. Hahn, 2006, "Lille Conference Talk," J. Magn. Reson. 179, pp. 9-19.

[13] R. K. Cooper, J. A. Jackson, 1980 "Remote (Inside-Out) NMR. I., Remote Production of a Region of Homgeneous Magnetic Field," J. Magn. Reson. 41 (1980) pp. 400-405.

[14] L. J. Burnett, J. A. Jackson, 1980, "Remote (Inside-Out) NMR. II. Sensitivity of NMR Detection for External Samples," J. Magn. Reson., 41, pp. 406-410.

[15] J. A. Jackson, L. J. Burnett, F. Harmon, 1980, Remote (Inside-Out) NMR. III. Detection of nuclear magnetic resonance in a remotely produced region of homogeneous magnetic field, J. Magn. Reson., 41, pp. 411-421.

[16] C. I. Nicholls, A. Santos, 1991, "Hydrogen Transient Nuclear Magnetic Resonance for Industrial Moisture Sensing," Drying Technol., 9, pp. 849-873.

[17] C. I. Nicholls, A. Santos, 1991, "Hydrogen Transient Nuclear Magnetic Resonance for Industrial Moisture Sensing," Drying Technol., 9, pp. 849-873.

[18] G. A. Matzkanin, A. Santos, 1986, "One-Sided NMR Sensor System Measures Soil/Concrete Moisture," Design News.

[19] R. F. Paetzold, G. A. Matzkanin, A. Santos, 1985, "Surface Soil Water Content Measurement Using Pulse Nuclear Magnetic Resonance Techniques," Soil Sci. Soc. Am. J., 49, 537-540.

[20] G. A. Matzkanin, J. D. King, W. L. Rollwitz, 1981, "Nondestructive Measurement of Moisture in Concrete using Pulsed NMR," Proc. 13th Symp. Nondestructive Evaluation," San Antonio.

[21] A. Marko, B. Wolter, W. Arnold, 2007 "Application of portable nuclear magnetic resonance surface probe porous media," J. Magn. Reson., 185, pp. 19-25.

[22] R. M. Pearson, L. R. Ream, C. Job, J. Adams, 1987, Use of NMR Spectrometers for Process Control, Cereal Foods World, 32, pp. 822-826.

[23] R. M. Pearson, D. I. Wetzel, 1985, "Rapid On-Line Moisture Determination of Whole Kernel Wheat by Pulsed Nuclear Magnetic Resonance," Cereal Foods World, 30, pp. 563-564.

[24] W. L. Rollwitz, J. D. King, G. A. Matzkanin, R. F. Paetzhold, 1983, "Magnetic Resonance: A Versatile Sensor for Agricultural Applications, Proc. Nat. Conf. Agricultural Electronics Applications ASAE, Chicago

[25] J. D. King, W .L. Rollwitz, A. Santos, J. R. Gonano, 1978, "Applications of Nuclear Magnetic Resonance to the Detection and Identification of Explosives," Proc. New Concepts Symposium and Workshop on the Detection and Identification of Explosives, Reston.

[26] J. D. King, W. L. Rollwitz, A. Santos, 1982, "Nuclear Magnetic Resonance for Explosives Detection," Proceedings of the ASTM Symposium on Airport Security, Philadelphia.

[27] L. Burnett, 1994, "Single-Sided NMR," Quantum Design Newsletter, 4, pp. 9.

[28] G. A. Matzkanin, 2002, "A Review of Nuclear Magnetic Resonance for Nondestructively Characterizing Materials," 11th Int. Symp. Nondestr. Charact. Mat., pp. 24.-28, Berlin.

[29] G. A. Matzkanin, 1985, "Application of Spatially Localized NMR to Nondestructive Evaluation," Proc. 2nd World Conf. NDT, pp. 3-8, Las Vegas.

[30] J.A. Jackson, L.J. Burnett, F. Harmon, 1980, "Remote (Inside-Out) NMR. III. Detection of nuclear magnetic resonance in a remotely produced region of homogeneous magnetic field," J. Magn. Reson., 41, pp. 411-421.

[31] G. Eidmann, R. Savelsberg, P. Blümler, B. Blümich, 1996, "The NMR MOUSE: A Mobile Universal Surface Explorer," J. Magn. Reson., A122, pp. 104-109.

[32] B. Blümich, P. Blümler, G. Eidmann, A. Guthausen, R. Haken, U. Schmitz, K. Saito, G. Zimmer, 1998, "The NMR MOUSE: Construction, Excitation, and Applications," Magn. Reson. Imag., 16, pp. 479-484.

[33] A. Guthausen, G. Zimmer, P. Blümler, B. Blümich, 1998, "Analysis of Polymer Materials by Surface NMR via the NMR MOUSE," J. Magn. Reson., 130, pp. 1-7.

[34] A. Guthausen, G. Zimmer, R. Eymael, U. Schmitz, P. Blümler, B. Blümich, 1998, "Soft-Matter Relaxation by the NMR MOUSE," Spatially Resolved Magnetic Resonance, Wiley-VCH, Weinheim, pp. 195-209.

[35] M. D. Hürlimann, 2001, "Diffusion and Relaxation Effects in General Stray Field NMR Experiments," J. Magn. Reson., 148, 367-378.

[36] M. D. Hürlimann, L. Venkataramanan, C. Flaum, P. Speier, C. Karmonik, R. Freedman, N. Heaton, 2002, "Diffusion-Editing: New NMR Measurement of Saturation and Pore Geometry", 43rd Annual SPWLA Meeting, pp. 1-14, Japan.

[37] G. Leu, E. J. Fordham, M. D. Hürlimann, P. Frulla, 2005, "Fixed and Pulsed Gradient Diffusion Methods in Low-Field Core Analysis," Magn. Reson. Imag., 23, pp. 305-309.

[38] Y. Q. Song, M. D. Hürlimann, C. Flaum, 2003, "A Method for Rapid Characterization of Diffusion," J. Magn. Reson., 161, pp. 222-233.

[39] A. Wiesmath, C. Filip, D. E. Demco, B. Blümich, 2001, "Double-Quantum-Filtered NMR Signals in Inhomogeneous Magnetic Fields," J. Magn. Reson. 149, pp. 258-263.

[40] A. Wiesmath, C. Filip, D.E. Demco, B. Blümich, 2002, "NMR of Multipolar Spin States Excited in Strongly Inhomogeneous Magnetic Fields," J. Magn. Reson., 154, pp. 60-72.

[41] Y.Q. Song, U.M. Scheven, 2005, "An NMR Technique for Rapid Measurement of Flow," J. Magn. Reson., 172, pp. 31-35.

[42] S. Mailboom and D. Gill, 1958, "Modified spin-echo method for measuring nuclear times. Review of Scientific Instruments," Review of Scientific Instrumentation, 29, pp. 688.

[43] B. Blümich, J. Perlo, F. Casanova, 2008, "Mobile Single-Sided NMR, Progress in Nuclear Magnetic Resonance Spectroscopy", 52, pp. 197–269.

[44] H. Raich, P. Blümler, 2004, "Design and Construction of a Dipolar Halbach Array with a Homogeneous Field from Identical Bar Magnets: NMR Mandhalas," Concepts in Magn. Reson., B23, pp. 16-25.

[45] R. Haken and B. Blümich, 2000, "Anisotropy in Tendon Investigated in Vivo by a Portable NMR Scanner, the NMR-MOUSE," Journal of Magnetic Resonance, 144, 2, pp. 195-199.

[46] P. J. Prado, B. Blümich, and U. Schmitz, 2000, "One-Dimensional Imaging with a Palm-Size Probe," Journal of Magnetic Resonance, 144, pp. 200–206.

[47] S. Rahmatallah , Y. Li, H. S. Seton, I. S. Mackenzie, J. S. Gregory, and R. M. Aspden, 2005, "NMR detection and one-dimensional imaging using the inhomogeneous magnetic field of a portable single-sided magnet," Journal of Magnetic Resonance, 173, 1, pp. 23- 28.

105

[48] N. Baril, E. Thiaudiere, B. Quesson, C. Delalande, P. Canioni, J. P. Franconi, 2000, "Single-coil surface imaging using a radiofrequency field gradient," Journal of Magnetic Resonance, 146, 1, pp 223-227.

[49] F. Casanova and B. Blümich, 2003, "Two-dimensional imaging with a single-sided NMR probe," Journal of Magnetic Resonance, 163, 1, pp. 38-45.

[50] J. Perlo, F. Casanova and B. Blümich, 2004, "3D imaging with a single-sided sensor: an open tomography," Journal of Magnetic Resonance, 166, 2, pp. 228-235.

[51] J. Kolz, N. Goga, F. Casanova, T. Mang, B. Blümich, 2007, "Spatial Localization with Single-Sided NMR Sensor," Appl. Magn. Reson., 32, pp. 171-184.

[52] F. Casanova, J. Perlo, B. Blümich, 2006, "Depth profiling by Single-Sided NMR," NMR Imaging in Chemical Engineering, Wiley-VCH, Weinheim, pp. 107 – 123.

[53] A. Samoilenko, D. Y. Artemov, and L. A. Sibeldina, 1988, "Formation of sensitive layer in experiments on NMR subsurface imaging of solids," JEPT Letter, 47, pp. 348.

[54] T.B. Benson and P.J. McDonald, 1995, "Profile amplitude-modulation in stray field magnetic resonance imaging," Journal of Magnetic Resonance Series, A, 112, pp. 17-23.

[55] J. H. Baltisbergera, S. Hedigerb, and L. Emsley, 2005, "Multi-dimensional magnetic resonance imaging in a stray magnetic field," Journal of Magnetic Resonance, 172, pp. 79–84.

[56] J. B. Miller and A. N. Garroway, 1994, "Planar imaging by NMR," 35th Experimental NMR Conference, pp. 186.

[57] P. P. Hsu and J. H. Chen, 1994, "A Simulation of MR Imaging Sequences Using the Numerical Solutions of Bloch Equations," Proceedings of the 16th Annual International Conference of the IEEE Engineering in Medicine and Biology Society. Part. 1, Baltimore, pp. 574-575.

[58] R. M. Summers, L. Axel, and S. Israel, 1986, "A computer simulation of nuclear magnetic resonance imaging," Magnetic Resonance in Medicine, 3, pp. 363-376.

[59] D. A. Yoder, Y. Zhao, C. B. Paschal, and J. M. Fitzpatrick, 2004, "MRI simulator with object-specific field map calculations," Magnetic Resonance Imaging, 22, 3, pp. 315-328.

[60] M. B. E. Olsson, R. Wirestam, and B. R. R. Persson, 1995, "A computer simulation program for MR imaging: Application to RF and static magnetic field imperfections," Magnetic Resonance in Medicine, 34, pp. 612-617.

[61] J. Bittoun, J. Taquin, and M. Sauzade, 1984, "A computer algorithm for the simulation of any nuclear magnetic resonance (NMR) imaging method," Magnetic Resonance Imaging, 3, pp. 363-376.

[62] R. M. Summers, L. Axel, and S. Israel, 1986, "A computer simulation of nuclear magnetic resonance imaging," Magnetic Resonance in Medicine, 3, pp. 363-376.

[63] M. B. E. Olsson, R. Wirestam, and B. R. R. Persson, 1995, "A computer simulation program for MR imaging: Application to RF and static magnetic field imperfections," Magnetic Resonance in Medicine, 34, pp. 612-617.

[64] A. R. Brenner, J. Kürsch, and T. G. Noll, 1996, "Distributed Large-Scale simulation of MR imaging," MAGMA (Magnetic Resonance Materials in Physics, Biology, and Medicine), 4, 2, pp. 291-292.

[65] H. B. Cattin, F. Bellet, J. Montagnat, and C. Odet, 2003, "Magnetic resonance imaging (MRI) simulation on a grid computing architecture," Cluster Computing and the Grid, pp. 582–587.

[66] L.A. Stables, R.P. Kennan, A.W. Anderson, and J.C. Gore, 1999, "Density matrix simulations of the effects of J coupling in spin echo and fast spin echo imaging," Journal of Magnetic Resonance Imaging, 140, pp. 305–314.

[67] O.P. Yee, J.A. Nyenhuis, R.L. Stroshine, and W.K Wai, 1995, "Magnetic field inhomogeneity effects on spin echo NMR diffusion measurements," IEEE Transactions on Magnetics, 31 , 6 , pp. 3584 – 3586.

[68] C. Cai, Z. Chen, S. Cai, and J. Zhong, 2005, "A simulation algorithm based on Bloch equations and product operator matrix: application to dipolar and scalar couplings," Journal of Magnetic Resonance, 172, 2, pp. 242-253.

[69] K. S. Kwan, A. C. Evans, and G. B. Pike, 1999, "MRI Simulation-Based Evaluation of Image-Processing and Classification Methods," IEEE Transactions on medical imaging, 18, pp 11.

[70] O. Ocali, E. Atalar, 1998, "Ultimate intrinsic signal-to-noise ratio in MRI," Magnetic Resonance in Medicine, 39, pp.462-473.

[71] W. A. Edelstein, G. H. Glover, C. J. Hardy *et al.*, 1986, "The intrinsic signal-to-noise ratio in NMR imaging," Magnetic Resonance in Medicine, 3, pp. 604-618.

[72] P. A. Bottomley, T. H. Foster, R. E. Argersinger, and L. M. Pfeifer, 1984, "A review of normal tissue hydrogen NMR relaxation times and relaxation mechanisms from 1–100 MHz: Dependence on tissue type, NMR frequency, temperature, species, excision, and age," Med. Phys., 11, pp. 425-448.

[73] V. E. Arpınar, H. Yiğitler, B. M. Eyüboğlu, "Homojen Olmayan Manyetik Alanlarda Manyetik Rezonans Görüntüleme Sisteminin Üç Boyutlu Uzayda Nümerik Modellemesi," Proc. Of Ursı-Türkiye 2006 3rd National Congress, Ankara, pp.186-8, 2006.

APPENDIX A

THEORY OF MR-EIT IN INHOMOGENEOUS MAIN MAGNETIC FIELDS

As stated before Bloch equation can be used model the spin & magnetic field interaction in macroscopic level. That is

$$\frac{d\vec{M}\left(\overline{r},t\right)}{dt} = \gamma\vec{M}\left(\overline{r},t\right)\times\vec{B}\left(\overline{r},t\right) - \frac{\vec{M}_{\perp}\left(\overline{r},t\right)}{T_2\left(\overline{r}\right)} - \frac{\left(\vec{M}_{\parallel}\left(\overline{r},t\right) - \vec{M}^{\,0}\left(\overline{r}\right)\right)}{T_1\left(\overline{r}\right)} \tag{A.1}$$

where $\vec{B}_0(\overline{r})$ static main magnetic flux density, and

$$\vec{M}_{\parallel}\left(\overline{r},t\right) = \frac{\vec{B}_0\left(\overline{r}\right)\vec{B}_0^T\left(\overline{r}\right)}{\left\|\vec{B}_0\left(\overline{r}\right)\right\|^2}\vec{M}\left(\overline{r},t\right) \tag{A.2}$$

$$\vec{M}_{\perp}\left(\overline{r},t\right) = \left(I - \frac{\vec{B}_0\left(\overline{r}\right)\vec{B}_0^T\left(\overline{r}\right)}{\left\|\vec{B}_0\left(\overline{r}\right)\right\|^2}\right)\vec{M}\left(\overline{r},t\right) \tag{A.3}$$

In MR-EIT experiments the test object has to be conductive. And an external current is applied to the object via electrodes. This externally applied current generates current distribution in the test object. Due to that current distribution a magnetic flux density is generated. Name this magnetic flux density as $\vec{B}_C(\overline{r})$. This $\vec{B}_C(\overline{r})$ can be inserted as new term in Bloch equation as,

$$\frac{d\vec{M}(\bar{r},t)}{dt} = \gamma\vec{M}(\bar{r},t)\times\left(\vec{B}(\bar{r},t)+\vec{B}_C(\bar{r},t)\right)-\frac{\vec{M}_\perp(\bar{r},t)}{T_2(\bar{r})}-\frac{\left(\vec{M}_\parallel(\bar{r},t)-\vec{M}^0(\bar{r})\right)}{T_1(\bar{r})} \quad (A.4)$$

If the main magnetic flux density $\vec{B}_0(\bar{r})$ is very large compared to $\vec{B}_C(\bar{r},t)$ than total magnetic field can written as

$$\vec{B}_0(\bar{r})+\vec{B}_C(\bar{r},t)=\vec{B}_0(\bar{r})+\frac{\vec{B}_0(\bar{r})\cdot\vec{B}_C(\bar{r},t)}{\left\|\vec{B}_0(\bar{r})\right\|^2}\vec{B}_0(\bar{r})+\left(\vec{B}_C(\bar{r},t)-\frac{\vec{B}_0(\bar{r})\cdot\vec{B}_C(\bar{r},t)}{\left\|\vec{B}_0(\bar{r})\right\|^2}\vec{B}_0(\bar{r})\right) \quad (A.5)$$

$$\vec{B}_0(\bar{r})+\vec{B}_C(\bar{r},t)=\underbrace{\left(1+\frac{\vec{B}_0(\bar{r})\cdot\vec{B}_C(\bar{r},t)}{\left\|\vec{B}_0(\bar{r})\right\|^2}\right)\vec{B}_0(\bar{r})}_{A}+\underbrace{\left(\vec{B}_C(\bar{r},t)-\frac{\vec{B}_0(\bar{r})\cdot\vec{B}_C(\bar{r},t)}{\left\|\vec{B}_0(\bar{r})\right\|^2}\vec{B}_0(\bar{r})\right)}_{B} \quad (A.6)$$

Since $\vec{B}_C(\bar{r},t)$ assumed to be zero very small compared to $\vec{B}_0(\bar{r})$ then **B** can be ignored. Then

$$\vec{B}_0(\bar{r})+\vec{B}_C(\bar{r},t)\simeq\left(1+\frac{\vec{B}_0(\bar{r})\cdot\vec{B}_C(\bar{r},t)}{\left\|\vec{B}_0(\bar{r})\right\|^2}\right)\vec{B}_0(\bar{r}) \quad (A.7)$$

This is generally the case since the externally applied current has a limit in medical applications. As seen in the computer simulations the generated

111

magnetic flux density is in the range of μT and the main magnetic flux density is in the range of T due to that assumption is correct. So let us define a new parameter $\vec{B}_{Ceff}(\vec{r},t)$ which is the effective component of the $\vec{B}_C(\vec{r},t)$.

$$\vec{B}_{Ceff}(\vec{r},t) \simeq \left(\frac{\vec{B}_0(\vec{r}) \cdot \vec{B}_C(\vec{r},t)}{\left\| \vec{B}_0(\vec{r}) \right\|^2} \right) \vec{B}_0(\vec{r}) \tag{A.8}$$

By substituting $\vec{B}_{Ceff}(\vec{r},t)$ to (A.4) the Bloch equation becomes

$$\frac{d\vec{M}(\vec{r},t)}{dt} = \gamma\vec{M}(\vec{r},t) \times \left(\vec{B}(\vec{r},t) + \vec{B}_{Ceff}(\vec{r},t) \right) - \frac{\vec{M}_\perp(\vec{r},t)}{T_2(\vec{r})} - \frac{\left(\vec{M}_\parallel(\vec{r},t) - \vec{M}^0(\vec{r}) \right)}{T_1(\vec{r})} \tag{A.9}$$

The general form of Bloch equation when an externally current is applied is shown in (A.9). From there the effect on $\vec{M}(\vec{r},t)$ can be calculated. In MR systems, the magnetization vectors can not be directly measured. Only induced voltages in the receiver coil due to magnetization vector change with time can be measured. The induced voltage satisfies for a receiver coil defined by its magnetic flux density $\vec{B}_2(\vec{r})$ as in (A.10).

$$V(t) = -\int_{V_{obj}} \vec{B}_2(\vec{r}) \cdot \frac{d\vec{M}(\vec{r},t)}{dt} d\vec{r} \tag{A.10}$$

In (A.10) V_{obj} is the volume that will be imaged.

Now define $\vec{B}_2(\bar{r})$ sum of two vectors $\vec{B}_{2\parallel}(\bar{r})$ and $\vec{B}_{2\perp}(\bar{r})$ as

$$\vec{B}_{2\parallel}(\bar{r}) = \left(\frac{\vec{B}_0(\bar{r}) \cdot \vec{B}_2(\bar{r})}{\left\| \vec{B}_0(\bar{r}) \right\|^2} \right) \vec{B}_0(\bar{r}) \tag{A.11}$$

and

$$\vec{B}_{2\perp}(\bar{r}) = \vec{B}_2(\bar{r}) - \left(\frac{\vec{B}_0(\bar{r}) \cdot \vec{B}_2(\bar{r})}{\left\| \vec{B}_0(\bar{r}) \right\|^2} \right) \vec{B}_0(\bar{r}) \tag{A.12}$$

Substitute (A.11) & (A.12) into (A.10) and by using (A.2) & (A.3) equation becomes

$$V(t) = -\int_{V_{obj}} \left[\vec{B}_{2\parallel}(\bar{r}) + \vec{B}_{2\perp}(\bar{r}) \right] \cdot \frac{d}{dt} \left[\vec{M}_{\parallel}(\bar{r},t) + \vec{M}_{\perp}(\bar{r},t) \right] d\bar{r} \tag{A.13}$$

Take the derivative operator out of the integral and perform the dot product (A.13) becomes

$$V(t) = -\frac{d}{dt} \int_{V_{obj}} \vec{B}_{2\parallel}(\bar{r}) \cdot \vec{M}_{\parallel}(\bar{r},t) + \underbrace{\vec{B}_{2\parallel}(\bar{r}) \cdot \vec{M}_{\perp}(\bar{r},t)}_{A} + \underbrace{\vec{B}_{2\perp}(\bar{r}) \cdot \vec{M}_{\parallel}(\bar{r},t)}_{B} + \vec{B}_{2\perp}(\bar{r}) \cdot \vec{M}_{\perp}(\bar{r},t) d\bar{r} \tag{A.14}$$

A and *B* terms are equal to zero since the vectors are orthogonal to each other. Also for the other two dot product term vectors are parallel to each other. So that

$$V(t) = -\frac{d}{dt} \int_{V_{obj}} \left|\vec{B}_{2\parallel}(\vec{r})\right|\left|\vec{M}_{\parallel}(\vec{r},t)\right| + \left|\vec{B}_{2\perp}(\vec{r})\right|\left|\vec{M}_{\perp}(\vec{r},t)\right| d\vec{r} \qquad (A.15)$$

Divide the integral into two and take the derivative inside, then

$$V(t) = -\underbrace{\int_{V_{obj}} \left|\vec{B}_{2\parallel}(\vec{r})\right|\frac{d}{dt}\left|\vec{M}_{\parallel}(\vec{r},t)\right| d\vec{r}}_{A} - \underbrace{\int_{V_{obj}} \left|\vec{B}_{2\perp}(\vec{r})\right|\frac{d}{dt}\left|\vec{M}_{\perp}(\vec{r},t)\right| d\vec{r}}_{B} \qquad (A.16)$$

If assumed that only the gradients can be applied during the signal reception phase, then parallel component of magnetization vector can be found using the solution of (A.9) [4].

$$\left|\vec{M}_{\parallel}(\vec{r},t)\right| = \vec{M}_{\parallel}^{0}(\vec{r})\left(1 - e^{-t/T_1(\vec{r})}\right) + \vec{M}_{\parallel}(\vec{r},0_+)e^{-t/T_1(\vec{r})} \qquad (0.1)$$

In (A.17) $\vec{M}_{\parallel}^{0}(\vec{r})$ means magnetization vector at rest and $\vec{M}_{\parallel}(\vec{r},0_+)$ means parallel component of the magnetization vector after RF excitation pulse. As seen from the (A.17) derivative of the $\left|\vec{M}_{\parallel}(\vec{r},t)\right|$ inversely related to the relaxation parameter $T_1(\vec{r})$. For biological tissues in human body minimum of relaxation parameter T_1 found as 340 ms [72].

Now consider the part B in (A.16) to solve this part again assume that only the gradients can be applied during the signal reception interval then

$$\left|\vec{M}_\perp(\bar{r},t)\right| = \vec{M}_\perp(\bar{r},T_{SA}) \underbrace{e^{-t/T_2(\bar{r})}}_{A} \underbrace{e^{j\omega(\bar{r})t}}_{B} \underbrace{e^{-j(\gamma\int_{T_{SA}}^{t}\sum_i \vec{G}_i(\bar{r},\tau)d\tau)}}_{C} e^{-j(\gamma\int_{0_+}^{T_{SA}}\sum_i \vec{G}_i(\bar{r},\tau)+\vec{B}_{Ceff}(\bar{r},\tau)d\tau)} \quad (A.18)$$

In equation (A.18) Above function can be divided as multiple time dependent parts (A, B, C) then the derivative of above equation with respect to time is

$$\frac{d}{dt}\left|\vec{M}_\perp(\bar{r},t)\right| = \vec{M}_\perp(\bar{r},T_{SA}) e^{-j(\gamma\int_{0_+}^{T_{SA}}\sum_i \vec{G}_i(\bar{r},\tau)+\vec{B}_{Ceff}(\bar{r},\tau)d\tau)} \left(\underbrace{A'BCD}_{1}+\underbrace{AB'CD}_{2}+\underbrace{ABC'D}_{3}\right) \quad (A.19)$$

The dominant part is the second one since $\omega(\bar{r}) = \gamma \vec{B}_0(\bar{r})$ is very large compared to $1/T_2(\bar{r})$ and $\sum_i \gamma \vec{G}_i(\bar{r},\tau)$ for our case. In addition, $\omega(\bar{r})$ is also very large compared to $1/T_1(\bar{r})$ then A part of (A.16) can be also ignored. Then

$$V(t) \simeq -\int_{V_{obj}} \vec{B}_{2\perp}(\bar{r})\cdot\vec{M}_\perp(\bar{r},T_{SA}) e^{-j\gamma\left(\int_{0_+}^{T_{SA}}\sum_i \vec{G}_i(\bar{r},\tau)+\boxed{\vec{B}_{Ceff}(\bar{r},\tau)d\tau}\right)} e^{-t/T_2(\bar{r})} e^{-j\gamma\left(\int_{T_{SA}}^{t}\sum_i \vec{G}_i(\bar{r},\tau)d\tau\right)} j\omega(\bar{r}) e^{j\omega(\bar{r})t} d\bar{r} \quad (A.20)$$

The only difference in this equation due to current application is shown in the box above. By using previously designed reconstruction algorithm phase induced in the signal hence the $\vec{B}_{Ceff}(\bar{r},\tau)$ can be found directly.

For practical application in order to minimize the phase errors due to difference between actual and measured magnetic fields as an extra first image can be taken without a current application. And by taking the ratio of the signals a better result can be obtained. But since this is a simulation there has to be no need for taking the ratio since there is no deviation in magnetic fields.

VITA

Volkan Emre ARPINAR

Konutkent 1 Elmas Sok. No: D19/3

Çayyolu

06530 Ankara - TURKEY

Phone : +90 (312) 240 66 74

E-mail : earpinar@metu.edu.tr

P e r s o n a l   I n f o r m a t i o n

Date of Birth **:** April 12, 1977

E d u c a t i o n

Ph.D.: *2003 - 2009*

Dept. of Electrical & Electronics Engineering,
Middle East Technical University

Courses: Adaptive Signal Processing, Numerical Methods for Electromagnetics, Spectral Estimation, Physiological Control Systems Analysis, Digital Video Processing, Fundamentals of Radar Systems 1, Fourier Optics, Optimization.

M.Sc. Degree: (3.64/4)   *1999-2003*

Dept. of Electrical & Electronics Engineering,
Middle East Technical University

Courses: Advanced Medical Imaging, Bioelectricity and Biomagnetism,
Signal Analysis and Processing, Digital Image Processing, Linear System
Theory, Estimation Theory

Thesis: Reconfigurable Microcontroller Based Multifrequency Electrical
Impedance Tomography (Abstract is enclosed)

Specialization: Medical instrumentation, Medical imaging systems, MRI
hardware, running of a 0.15T Oxford magnet, MR data acquisition control
hardware and software.

B.Sc. Degree: (3.32/4)   *1995 - 1999*

Dept. of Electrical & Electronics Engineering,
Middle East Technical University
with course load specialization in computer and telecommunication systems,
biomedical engineering and medical imaging

Graduation Project: Implementation of Positron Emition Tomograph (PET)
simulation program using MATLAB.

High School: *1992 - 1995*

Ankara Gazi Anatolian High School

Secondary: *1989 – 1992*

Ankara Gazi Anatolian High School

Kastamonu Anatolian High School

P u b l i c a t i o n s

- V.E. Arpınar, B.M. Eyüboğlu, " Magnetic Resonance Signal Analysis in Inhomogenous Magnetic Fields," Proceedings of Medical Physics and Biomedical Engineering World Congress 2009, Munich – GERMANY, 2009.

- V.E. Arpınar, B.M. Eyüboğlu, "Magnetic resonance signal analysis in inhomogenous main magnetic field," Proceedings of European Society for Magnetic Resonance in Medicine and Biology 2009 Congress, Antalya – Turkey, 2009.

- V.E. Arpınar, B.M. Eyüboğlu, "Magnetic resonance imaging in inhomogeneous magnetic fields with noisy signal," Proceedings of 4th European Congress for Medical and Biomedical Engineering, Antwerp – BELGIUM, 2008.

- V.E. Arpınar, B.M. Eyüboğlu, "Microcontroller Controlled Multifrequency Electrical Impedance Tomograph," Proceedings of The IEEE/EMBS 23rd Annual Conference, Istanbul - TURKEY, 2001.

- V.E. Arpınar, B.M. Eyüboğlu, "Homojen Olmayan Manyetik Alanda MR sinyalinin analizi," 14. Biyomedikal Mühendisliği Ulusal Toplantısı, İzmir, 2009.

- V.E. Arpınar, B.M. Eyüboğlu, "Homojen Olmayan Manyetik Alanlar Kullanan Manyetik Rezonans Görüntüleme Sisteminde Gürültünün Hesaplanması," 13. Biyomedikal Mühendisliği Ulusal Toplantısı, Ankara, 2008.

- V.E. Arpınar, B.M. Eyüboğlu, "Homojen Olmayan Manyetik Alanlarda Manyetik Rezonans Görüntüleme," 13. Biyomedikal Mühendisliği Ulusal Toplantısı, Ankara, 2008.

- V.E. Arpınar, B.M. Eyüboğlu, "Homojen Olmayan Manyetik Alanlar İçin Gürültü Tanımlaması Ve Görüntü Oluşturma Algoritmasının Performansı," 3. Türk Manyetik Rezonans Derneği Kongresi Bildiri Kitabı, Ankara, Pp.32, 2008.

- V.E. Arpınar, H. Yiğitler, B.M. Eyüboğlu, "Homojen Olmayan Manyetik Alanlarda Manyetik Rezonans Görüntüleme Sisteminin Üç Boyutlu Uzayda Nümerik Modellemesi," Proc. Of Ursı-Türkiye 2006 3rd National Congress, Ankara, Pp.186-8, 2006.